Unravelling motor protein organization on lysosomal membranes with super-resolution microscopy

Guillaume Cordier

Under the supervision of

Professor Melike Lakadamyali

Thesis Supervisor:

Prof. Melike Lakadamyali

(ICFO-The Institute of Photonic Sciences, Spain)

Thesis Committee Members:

- Dr. Oriol Gallego
  (IRB- The Institute for Research in Biomedicine in Barcelona, Spain)

- Dr. Francesca Cella Zanacchi
  (IIT- Istituto Italiano di Tecnologia in Genova, Italia)

- Prof. Maria Garcia-Parajo
  (ICFO-The Institute of Photonic Sciences, Spain)

A mes parents qui m'ont transmit le goût de la lecture, ouvrant la porte à tant d'aventures.
Un chapitre se termine

Acknowledgment

Since I came at ICFO, back in January 2013, I met many people who helped me in their own different ways, for the development of my research and my life as a researcher. It seems impossible now to acknowledge everyone, but I will give it a try.

First of all, I would like to acknowledge my boss, Pr. Melike Lakadamyali, who, in spite of facing drastic life changes, has always be helpful and available, patient and optimistic about my work. Thank you for trusting me for these years. I would like to show gratitude also the past member of my research group, who were my first mentors, and inspiring example, like Johnny Tam, who me taught how do get thing done in the right way, have a balanced life, the concept of triple checking every details, and also for being there to cheer me when I was desperate. I would like to give credit to Joe Borberly also for his infinite patience and skills for teaching me the bases of matlab, and tricks to build a STORM setup from scratch. I would like to thanks Stefan Balint for his warm and joyful mood inside and outside of the office. I would like to bless Angel Sandoval for all the biological preparations, and for his patience for answering any kind of question about life at the macro, micro and nanoscale and biology in general. A huge thank to Ione Verdeny who was the major influence on myself in the last 4 years, a real hard worker doubled with incredibly skilled dancer, helpful friend and later lunch eater. Pablo Gomez who came lately in the lab to start a PhD was sharing my office and made the communication easier, I want give a shout for widening my mind, and for the discussion about my research, Spanish literature and songs. I should also praise Jason Otterstorm for showing so much joyfulness and scientific rigor everyday. He is one of my scientist mentor in the research field too. I would like to show appreciation to the whole Advanced and Fluorescent Imaging Biophysics group and collaborators for all these cakes, lunch, group meetings or moments together: Maria-Aurelia, Nela Durisc, Francesca Cella Zanacchi, Irina, Laurent Ladépêche, Anna Oddonne, Lara Laparra, Shreyasi Thakur, Nitin Mohan for his smile, Jesus Planaguna i Valls, my personal catalan teacher, Rafael Sibilo. I would like to thank the whole SMB group for the interesting joint group meeting, joint lunch meeting and card borrowing in order to enter into the Biolab. From the SNL facility, I would like to thanks Jordi Andilla, for helping with the confocal imaging. I would like to take my hat off to the whole ICFO administration and staff : ranging from facility services to mechanical workshop, electronics workshop, secretariat and human resources, for their efficiency in solving any kind of problem or necessity : especially Jonas, Carlos Dengra, Anne Göttsner, the KTT unit and Miriam Marti for pushing me to expand and vulgarize science to the limits with light painting or by dancing. Of course I would like to give thanks to all my ICFO buddies from different groups, who were sharing with me the PhD experience (up and downs) : Alejandro Mattar who tried to explained me quantum physics every Friday, Johann the best IFCO gluten free photograph, Giorgio, Stijn, Nicolas Maring, Eric Puma-my sailing mate, Gabriele for your Lithuanian classes and dances, Simon Cooper, and the Café de la

Llum staff for naming a sandwich after my name…last but not least Mathieu Massicote and Jane Joplin for the motivation support, their vision of life and research and the good moments in Garraf.

I spend most of my time at ICFO the last 5 years but I should also thank all the people, supporting me and inspiring me in a daily base, outside of the work.

I would like to give a huge thank to people from another major world in my life : all my dancing friends who stimulated me, who kept my mind fresh and my body in shape. There is a long list but I should mention my dancer gang : Julia, Ivo, Javiera, Noelia, Luigi, my wife Mashag. For the kicks. Dr. Patrick O'Brien and my Lithuanian family: Martynas, Kamile, Giedre, Arnas…my friends and teachers especially Alexandros Marinis, Max y Serena, Elle Bereckny, Edu and Silvia, and all of my students. Special thanks also to the "Fast Socks" : Sandy Lewis together with Adria & Barbara, Marti, Masha for upgrading my level of organization to the non-return point and making the Barcelona Shag Society possible. I would like to thanks Quico and the Boozan Dukes as well as Gadjo, Chino and the Big Bet for making the soundtrack of my life this past 4 year

Quiero agradecer tambien a todos mis amigos de Garraf que me animaron para seguir hacia adelante : Montse y Esteban para cuidarme, enseñarme su vida de escaladores verdadero y mucho mas, Irene y Oscar, Eric, Lorenzo, Xavi, Marina. Del puerto quiero rendir homenaje al difunto Carlos, agradecer Steve & Sara por todo su amor y amistad, y al pantalán 3. Quiero agradecer a Lottie por vivir conmigo 6 meses en el velero y suportarme. Quiero también agradecer a Cira Valls para compartir su piso conmigo cuando llegue en Barcelona, animarme a conocer Catalunya y el barrio de Sants. Un agradecido muy especial al Chulapio y Alvaro.

Je voudrai également remercier Nina qui a illuminé ma vie ces dernières années, de par sa joie de vivre et son hospitalité légendaire. J'en profite pour remercier au passage Chacha et Stéfan, Estelle et Marc, Guillaume, vieille branche, Justine et Arthur . Enfin je voudrai remercier mes amis francais qui ne m'ont pas oublié après tant d'années expatrié : j'ai nommé Guillaume Taburet, Monsieur Léo Briend, Adrien Vergne, Dr. Adrien Guérin, Dr. Simon Cabanes, Dr. Clement Thorey. Petit remerciement à tous ceux qui ont squatté mon bateau, à Matthieu Jungfer, à mes potos de l'école d'ingé, à Dr. Marie Mazoyer, à Dr. Anthony Bardon et sa femme Dr. Tifaine Bardon, pour leurs encouragements depuis le Japon. Enfin un énorme merci à Dr. Pr. Sergi Padilla Para pour m'avoir incité à faire mon doctorat à l'ICFO.

Je voudrai remercier profondément mes parents Jérôme Cordier et Gabrielle Le Vot ainsi que ma soeur Enora pour leur soutient inconditionel dans cette aventure, d'accepter ma

facon de vivre, et de m'encourager dans toutes les étapes importantes de ma vie. Je voudrai remercier toute ma grande famille pour leur support et compassion.

Al final quiero agradecer el amor de mi vida, Pilar por cuidarme, por ocuparse de todo cuando no podia y proporcionarme continuamente con amor y felicidad.

Table of Contents

Abstract

Intracellular transport is of paramount importance to maintain subcellular organization. Failures in intracellular transport can lead to several diseases, especially if the failure happens in the nervous system.

The key players involved in intracellular transport are the microtubule cytoskeleton and motor proteins. The microtubule cytoskeleton connects the perinuclear region to the cell periphery and acts as tracks for transport. Motor proteins translocate along the microtubule cytoskeleton in order to carry cargoes. There are two kinds of motor protein families that move cargo along polarized microtubules: the kinesin superfamily moves toward the (+) end of the microtubule track whereas dynein moves toward the (-) end of the microtubule track.

Since their first discovery in the 60's, motor proteins have been extensively studied using *in vitro* single molecule methods, allowing us to understand the bases of intracellular transport. However, motor proteins, their microtubule tracks and vesicular cargoes have sizes that range from tens to hundreds of nanometers, below the diffraction limit of light microscopy. Therefore, studying intracellular trafficking in the cellular context has been challenging. While the bottom-up *in vitro* studies are highly valuable for enhancing our understanding of how motor proteins function, they cannot capture the full complexity of the intracellular environment. Therefore, it is highly important to develop new methods to overcome the challenge of studying intracellular transport in intact cells. In the last decade, with the development and advent of super-resolution microscopy methods, a revolution occurred in the field of light microscopy. These methods have made it possible to visualize sub-cellular structures with nanometer spatial resolution, breaking the diffraction limit.

This thesis first describes the development of new methods for high-throughput and multi-color super-resolution microscopy (**Chapters 2 and 3**). Subsequently, I applied these methods to study the organization of motor proteins on the lysosome membrane inside cells with the purpose of determining how intracellular transport can be regulated via motor-protein organization (**Chapter 4**). **Chapter 1** is an Introduction to the state of the art for our knowledge in microtubule-based intracellular transport. Chapter 2 introduces the single molecule localization techniques that improve the spatial resolution of light microscopy. This chapter emphasizes the Stochastic Optical Reconstruction Microscopy (STORM) technique, which I used to study the organization of microtubule based motor proteins around lysosomes as well as the fusion and fission of mitochondria. Chapter 3 describes the development of two new techniques: (i) the use of microfluidic devices to improve the throughput of correlative live-cell and super-resolution microscopy, thus allowing to observe rare events and (ii) sequential multi-color imaging that increases the number of colors that can be imaged with STORM. **Chapter 4** focuses on the biological application of sequential multicolor imaging to study the 3D organization of dynein and

kinesin on lysosomal membranes. Conclusions and Future Perspectives are provided in **Chapter 5**.

Chapter 1
Introduction to intracellular transport

"Science describes nature as exposed to our method of questioning" (Heisenberg)

Cells need to regulate a myriad of processes from organelle positioning to protein transport and delivery via vesicles or protein degradation. To achieve these tasks with high spatial and temporal precision, cells rely on a network of microtubules and actin filaments connecting different parts of the cell interior. The microtubule and actin cytoskeleton, among other functions, are used as tracks for motor proteins to travel on and carry a multitude of different cargoes to different cellular locations. Kinesin and dynein motors transport cargoes toward the cell periphery or toward the cell nucleus, respectively, via the microtubules, whereas myosin motors use the actin network to more locally transport and position cargoes. Many regulatory mechanisms control intracellular transport efficiency. A failure in these mechanisms could lead to a drastic change in cellular organization and eventually lead to cell death, as in the case of several nervous system diseases. Here, I will describe the state of the art in our knowledge of the microtubule based transport of endolysosomal vesicles.

1.1 Microtubule dependent transport by microtubule motors

Looking at the phylogenetic tree, dynein, kinesin and myosin motors are essential proteins found in very early eukaryotic organism. They developed along evolution into big families with great diversity. I will focus on the description of the kinesin and dynein motors which are responsible for microtubule based transport, unlike myosin which is an actin motor. Microtubules are polarized filaments composed of alpha and beta tubulin. Their (-) end is generally pointed at the microtubule organizing center near the nucleus where microtubules are nucleated, and their (+) end is pointed at the cell periphery.

The cytoplasmic dynein motor moves towards the (-) end (retrograde transport) carrying material towards the nucleus (Paschal and Vallee, 1987) whereas the kinesin motors typically move towards the (+) end (anterograde transport) carrying material to the cell edge.

1.1.1 Kinesin superfamily

Kinesin superfamily proteins (also known as KInesin Family or KIF) can be subdivided into 15 kinesin groups depending on the genes which are responsible for their expression(Miki *et al.*, 2001; Lawrence *et al.*, 2004). In total, 45 different kinesins have been identified in mammalian genes (Hirokawa, Noda and Okada, 1998). This superfamily of proteins performs many functions including positioning and segregation of chromosomes along mitotic spindle and intracellular transport of several vesicles and organelles (Wordeman, 2010). I will focus in this thesis on the KIF5 (part of the kinesin-1 family) and KIF3 (part of the from the kinesin-2 family). KIF3 and KIF5 interact with a huge variety of cargoes, including synaptic vesicle precursors (transported by KIF5) (Setou *et al.*, 2002), plasma membrane precursors (transported by KIF5 motors and KIF3)(Lippincott-Schwartz *et al.*, 1995; Noda *et al.*, 2001), mitochondria (KIF5 motors)(Cai, Gerwin and Sheng, 2005), lysosomes (KIF5 and KIF3 motors)(Tanaka *et al.*, 1998), AMPARs (KIF5 motors)(Hoerndli *et al.*, 2013), N-cadherin containing vesicle (KIF3 motors), and mRNA (KIF5 motors)(Kanai, Dohmae and Hirokawa, 2004). A huge range of membrane adaptors (RAB, Milton, fodrin) interact with KIFs directly or indirectly and are thought to regulate the localization of different KIFs to the membrane of different vesicles (Glater *et al.*, 2006). Intracellular transport can be categorized in few specific pathways and KIF5 and KIF3 motors have been shown to play an important role in all these pathways: the Golgi-ER transport, where KIF3 and KIF5 motors might work in synergy to regulate Golgi-ER trafficking, the Golgi-plasma membrane transport (Lippincott-Schwartz *et al.*, 1995) and the endocytic pathway involving transport of materials from the plasma membrane via early and late endosomes towards lysosomes for degradation (**Fig 1.1**).

1.1.2 Intracellular dynein

The dynein family contains 15 forms of dynein found in vertebrates but only 2 are not involved in ciliary or flagellar movement. They are then referred as cytoplasmic dynein1 and cytoplasmic dynein2 (Gibbons and Rowe, 1965; Vallee *et al.*, 2004). The latter has a narrow

range of functions and distribution (Pazour, Dickert and Witman, 1999). The cytoplasmic dynein1 is responsible for the motion of lysosomes, early and late endosomes, Golgi-ER trafficking, carrying organelles towards the minus ends of microtubules (Vallee *et al.*, 2004) (**Fig 1.1**). In this thesis, cytoplasmic dynein 1 will be referred to as dynein.
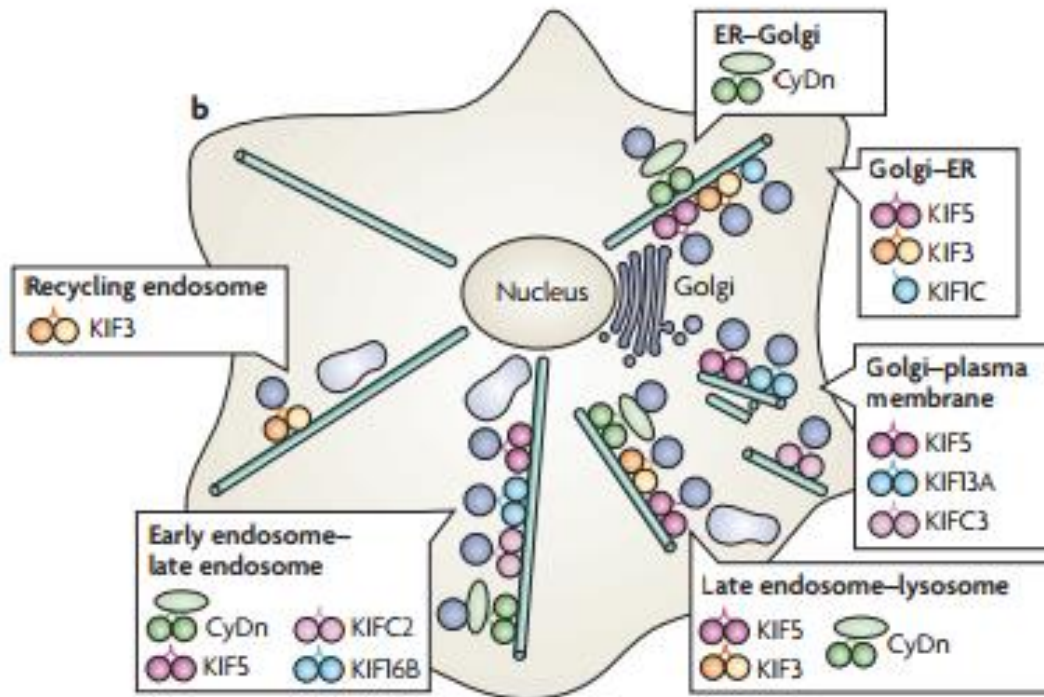
Fig 1.1 Sketch representing the distribution of motors protein on various cargoes. In each family of motor proteins, small structural differences lead to different tasks. Adapted from (Hirokawa *et al.*, 2009)

1.1.3 Motor properties

Kinesin Molecular structure

Even if kinesin and dynein perform similar tasks, their structure is completely different. The relatively simple kinesin (KIF5 and KIF3) structure is closer to the myosin structure in comparison to the more complex and larger structure of dynein (see **Fig 1.2**). Indeed, both motor proteins are dimeric, but the kinesin structure can be depicted with only 3 subunits, the kinesin heavy chains (KHCs), also known as the motor domain, the stalk or the tail domain and the kinesin light chains (KLCs) or cargo binding region. The kinesin head is composed of two motors, interacting with the microtubule via phosphorylation. The motors associate with two long (around 70 nm) and entangled polypeptide chains (the stalk) reaching to the KLCs, which serve as intermediate with the cargoes or membrane protein adaptors. Between the stalk and the motor domain, the neck linker is thought to play a crucial role in the communication between the two motor domains. Indeed, KIF5 with a

shorter neck-linker (14 amino acids and 17 respectively), is more processive than KIF3. KIF5 has a molecular weight close to 360 kDa and has been initially identified by means of biochemichal fractionation by Ron Vale (Vale, Reese and Sheetz, 1985). KIF3 motors are unique in that they form a heterotrimeric complex consisting of two different heavy chains (Wedaman *et al.*, 1996).

Dynein Molecular structure

Dynein is a massive molecular complex (~1.5 MDa, 4 times larger than kinesin) which was discovered by Ian Gibbons in the 60's (Gibbons and Rowe, 1965) but due to its size and complexity, it has been difficult to study. Dynein contains a variety of accessory subunits, dynein heavy chains (DLCs) and dynein light chains (DHCs) which encompass intermediate, light intermediate, and light chains (ICs, LICs, and LCs) (Vallee *et al.*, 1988). The DHCs (~520 kDa) consist of a microtubule-binding domain, linked to a motor domain (~320 kDa) by a stalk of 10 to 15 nm emerging from AAA subunits of the motor domain. The motor domain is formed by 6 ATPase units arranged in a ring (Burgess *et al.*, 2003) which denotes its origin to the AAA family of ATPases (Neuwald *et al.*, 1999). Each dynein complex contains two DHCs, two ICs (~74 kDa), two LICs (~53 kDa), and a small potentially variable number of LCs (Vallee *et al.*, 1988). Dynein processivity and cargo binding depend on its interaction with the accessory protein dynactin. For example, the ICs, the largest subunit, interacts with p150(Glued) (Vaughan and Vallee, 1995) which is part of the dynactin protein and is essential for microtubule recognition and binding. LICs and LCs have been implicated in direct cargo binding (Purohit *et al.*, 1999), whereas the ICs have a preponderant role in the dynein-dynactin interaction. The LCs have also been suggested to connect receptors such as neurotrophin receptors or rhodopsin to the dynein (Tai, Chuang and Sung, 2001; Yano *et al.*, 2001).
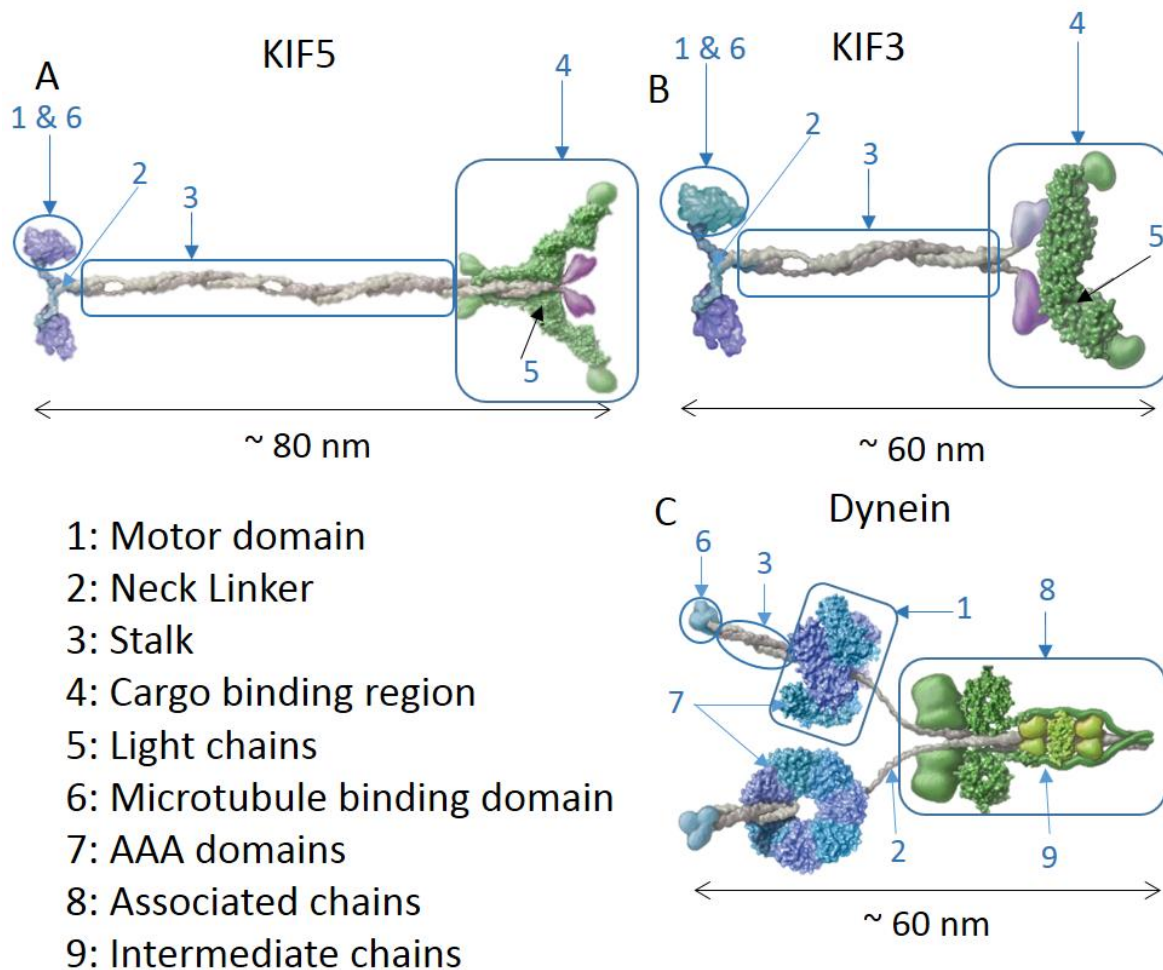
Fig 1.2 Scheme representing the structure of microtubule based-motor proteins. (A) the structure of KIF5, (B) the structure of KIF3 and (C) the structure of dynein. Both protein are dimers, they have a microtubule binding domain, a stalk, a motor domain, and associated chains that interact with the cargoes associated proteins. The motor domain is located at the microtubule-binding domain for the kinesin proteins whereas it is separated from the microtubule binding domain for dynein. Adapted from (Carter, 2013)

Kinesin and dynein mechanochemical cycle

Motors use the chemical energy of ATP to drive inner conformational changes that generate motile force and move along microtubule tracks (Vale, 2003).

KIF5 and KIF3 translocate on the microtubule track by stepping in a coordinated "hand over hand" manner in which each KHC takes 8 nm steps on the same protofilament (Ahmet Yildiz *et al.*, 2004). The front head is immobilized on the MT after ATP binding while the rear head detaches after ATP hydrolysis. The ATP binding induces a conformational change of the neck-linker, the mechanical element that will move the rear head towards the (+) end of the microtubule (Rice *et al.*, 1999). After a rapid diffusional search, the rear head rebinds to the MT in front of the immobilized head which causes the release of ADP. In that way, kinesin is

always holding the microtubule track with at least one head. Kinesin predominantly takes forward steps along MTs, but under a load superior to 7 pN, kinesin can take backward steps *in vitro* (Carter and Cross, 2005; Yildiz *et al.*, 2008). Remarkably, KIF3 and KIF5 have different behavior upon application of forces opposed to their directional motion (forces generated by dynein motors): KIF3s are rapidly unbinding and binding in contrast to KIF5 (Andreasson *et al.*, 2015). Indeed the microtubule affinity of kinesin fluctuates depending on its nucleotide states. KIF3 motors have been suggested to spend more time in a nucleotide state where its microtubule affinity is low, in comparison with KIF5 motors nucleotide states cycle. Contrarily to the kinesins, the force produced by dynein to attach and detach from the microtubule is not located in the motor head domain but in the AAA ring domain, and its mechanism is more complex. Briefly, ATP binding in one of the AAA domain will lead to structural changes leading to the closing of the ring formed by the AAA domains. By closing, a linker within the AAA domains will be in a bended state and finally in a stretched state leading to the release of the force accumulated while bending. Once stretched, it will push one of the filament forming the coiled-coiled stalk. The sliding of one of the coiled-coiled filament regarding the other, will in consequence propagate force to the microtubule binding domain. X-Ray crystallography allowed to deeply understand each different step of the biochemical cycle and how dynein changes its conformation in order to execute motion (Carter *et al.*, 2011; Kon, Sutoh and Kurisu, 2011; Bhabha *et al.*, 2014). The AAA ring is a very asymmetric structure, and several gaps exist where the AAA domains are farther apart and where ATP can bind. ATP binding induces a serie of conformational changes which result in force generation and a range of different microtubule-affinity states, an essential feature for alternating microtubule binding and unbinding of the individual motor domains (Roberts *et al.*, 2009)

Kinesin motility parameters: step size, processivity, speed and stall force

Intrinsic properties of single motor proteins such as step size, processivity, speed or stall force have been measured with *in vitro* and single molecule assays. *In vitro* motility assays were achieved using fluorescence microscopy under total internal reflection fluorescence conditions, allowing to measure step size, speed, and processive properties of single motors (DeWitt *et al.*, 2012) whereas optical trap assays were generally performed to estimate the force produced by single motors *in vitro* (Steve Block pioneered this method in biology). KIF3 and KIF5 have a regular step size of 8 nm (Svoboda *et al.*, 1993; Andreasson *et al.*, 2015). This is because kinesin motor head has a high affinity for the β-tubulin heterodimer subunit and moves along a single microtubule filament, where each heterodimer subunits are spaced by 8 nm. The two heads of kinesin take turns in moving along the microtubule tracks in a coordinated fashion.

Motor proteins have the particularity of being extremely processive, that is to say they undergo repeated enzymatic cycles, "steps", without releasing from the microtubule track. Processivity is also known as run length. *In vitro* optical trap experiments have shown that single kinesins could walk over 0.74 µm before detaching from the microtubule filament.

The average speed is estimated to be around to 700 nm.s^{-1} (Mallik *et al.*, 2005). The stall force is defined by the maximum amount of load that can be exerted on the motor proteins before they detach from the microtubule or stop their motion. The stall forces of the individual isolated motors hauling plastic beads *in vitro* range from 4 to 7 pN for kinesin (Svoboda 't and Block, 1994; Schnitzer, 1999). Interestingly, it has been found that the application of increasing forces on the motors decrease motor proteins´ processivity and speed (Visscher, Schnitzer and Block, 2000). Also, kinesin motors respond differently to external loads. KIF3 can walk against sustained load, whereas KIF3 motors tend to detach under loads (Visscher, Schnitzer and Block, 2000; Hendricks *et al.*, 2010; Schroeder *et al.*, 2012) and reattach rapidly. These results come from the structural difference of the motor domains (Andreasson *et al.*, 2015). *In vivo* studies have confirmed *in vitro* studies to a certain extent: for instance the reported step size for kinesin motors is similar (Kural, 2005; Nan, Sims and Xie, 2008). Nevertheless the cargo motility in the cell is notably higher than *in vitro* since speeds of 1 µm.s^{-1} were reported by different groups (Gross *et al.*, 2000; Kural, 2005; Nan, Sims and Xie, 2008). *In vivo*, motor driven cargos (both minus- and plus-end directed) are characterized by stop and go type saltatory motion over distances of multiple microns (Hoffman *et al.*, 2006; Jonas *et al.*, 2008; Bálint *et al.*, 2013). Kinesin stall force *in vivo* for a single motor has been measured to be ~3 pN (Sims and Xie, 2009; Leidel *et al.*, 2012), although higher forces have been reported, suggesting that multiple motors cooperate in transporting the cargo. Other studies measured forces in agreement with *in vitro* experiments (Hendricks, Holzbaur, and Goldman). The difference of results could be explained by the diversity of *in vivo* environments (Microtubule Associated Proteins affecting dynein transport, post translational modifications of microtubules changing motor protein affinity toward the microtubule, thus the attachment-detachment rate of the microtubule domain, correlated with the processivity and speed, etc.) which strongly affect motors behavior.

Dynein motility parameters: step size, processivity, speed and stall force

Dynein has been studied for more than 70 years, but unfortunately in different species and in different systems, which makes it difficult to reconcile results. Mammalian dynein step size varies from 4 nm to 32 nm (Mallik *et al.*, 2004) as measured using *in vitro* motility assays, and its microtubule binding domain seems to attach to the intradimer interface of α and β-tubulin (Redwine *et al.*, 2012). The *in vivo* reported step size for Dictyostelium dynein motors is a bit larger than the mammalian ones, from 16 to 24 nm (Nan *et al.*, 2005; Nan, Sims and Xie, 2008) and the budding yeast dynein shows 8nm steps (Reck-Peterson *et al.*, 2006).

Dynein has a hand-over-hand stepping behavior, but dynein can also exhibit an inchworm pattern, including side-stepping to adjacent microtubule filaments, also known as "drunk sailor" pattern (Vale and Toyoshima, 1988; Mallik *et al.*, 2005; Qiu *et al.*, 2012; Can *et al.*, 2014). Dynein's heads seem to behave independently in contrast with kinesin, which requires motor head coordination. In consequence, the processivity of dynein depends on

the microtubule-bound time compared with the unbound time of the individual motor domains. Lastly, the backward steps are quite frequent for dynein heads (Ross *et al.*, 2006; DeWitt *et al.*, 2012). The reason for this difference as compared to kinesin relies in dynein structure, which is more flexible than kinesin's, resulting in a looser coupling and variable stepping.

In vitro optical trap experiments have shown that single bovine and chicken dyneins could walk over 1 µm, before detaching from the microtubule filament and the average speed is estimated to be around 300 to 700 nm.s^{-1} (Mallik *et al.*, 2005; Berezuk and Schroer, 2007) according to bead assays. Interestingly fluorescence microscopy assay show the same processivity for mice dynein but no motility for human and rat dynein(Ori-McKenney *et al.*, 2010; McKenney *et al.*, 2014). Optical trap experiments showed also differences in force production depending on the species. The stall forces of the individual isolated motors hauling plastic beads *in vitro,* range from 1-2 pN for mammalian dynein to 7 pN for budding yeast dynein (Mallik *et al.*, 2004, 2005; Gennerich *et al.*, 2007; Vershinin *et al.*, 2008; Schroeder *et al.*, 2010). The essential presence of dynein's interactors such as dynactin, bicaudal homolog D 2 (BicD2) protein or Lissencephaly homolog 1 (Lis1) protein, demonstrated the complexity of intracellular transport. The processivity of human dynein in presence of specific cofactors reaches 5 to 9 µm (McKenney *et al.*, 2014; Schlager *et al.*, 2014), whereas bovine and chicken processivity decreases to 2 µm in presence of dynactin (King and Schroer, 2000; Culver–Hanlon *et al.*, 2006; Berezuk and Schroer, 2007). The velocities remain unchanged. An excellent review of difference in dynein's properties depending on their species has been written recently (Jha and Surrey, 2015).

1.1.4 Regulation of processivity

Regulation of motor proteins could be directly related to their task. Indeed the highly regulated processivity and low force production of mammalian dynein could be explained by the numerous tasks it needs to complete in the cell. Indeed, the diversity of tasks lead mammalian dynein to organize in groups (also referred later as "teams") or cooperate with kinesin during bidirectional transport (Arpan K Rai *et al.*, 2013). On the other hand, highly processive and highly force producing budding yeast dynein could be explained by its unique aim: pulling on to the microtubule in order to move the nucleus at the right place during mitosis (Starr, 2009). There are multiple modes of motor protein regulation involving allosteric mechanisms as well as extramolecular interactions affecting the motor activity. The regulation could occur at the microtubule interface: posttranslational modifications (PTM) of mictotubules and microtubule associated proteins (MAP) could influence the microtubule binding frequency and dynamics. The rigidity of microtubules induced by Tau binding increases dynein processivity (Vershinin *et al.*, 2007; Dixit *et al.*, 2008), although MAP/Tau binding inhibit kinesin transport along MTs *in vitro* (Trinczek *et al.*, 1999). Indeed, it remains unclear if either MAPs compete on the binding domain of MTs with motor proteins, or due to steric hindrance they prevent the motor protein from binding. On the other hand, GSK3β directly phosphorylates Tau, increasing its affinity for KIF5 (Lovestone *et*

al., 1994). Also, the regulation could occur at the motor protein interface. Dynein and dynactin together with the cargo specific adapter BicD2 protein could force dynein out of an autoinhibited conformation, strongly stimulating processive dynein motility (Urnavicius *et al.*, 2015; Carter, Diamant and Urnavicius, 2016). It could be also that wild-type dynactin turns dynein off when kinesin is active (Steven P Gross *et al.*, 2002). Lis1 and NudE have also been identified as dynein regulatory molecules (Efimov and Morris, 2000; Feng *et al.*, 2000; Vallee *et al.*, 2000). In a recent *in vitro* study, McKenney et al showed that Lis1 inhibits dynein detachment from microtubule by sterically forcing dynein to keep a conformation favorable to microtubule binding. The slower detachment results in a better summation of forces generated by multiple dyneins. Moreover the phosphorylation of the dynein motor subunit could also regulate its behavior: the phosphorylation of AAA3 is responsible for dynein-MT binding (Nicholas *et al.*, 2015) while the phosphorylation on DIC inhibits dynein-dynactin interaction *in vitro* (Vaughan *et al.*, 2002). GSK3β-mediated phosphorylation of dynein intermediate chain reduces dynein interaction with Ndel1-Lis1 complex, which enhances, as a consequence, dynein force production (McKenney *et al.*, 2010). Moreover, GSK3β increases release of kinesin from the cargo by phosphorylating KLC2 in rat brain (Morfini *et al.*, 2002). Also, -c-Jun N terminal kinase (JNKs) directly phosphorylates KIF5B and triggers its dissociation from microtubules (Stagi *et al.*, 2006). The regulation could indirectly occur: by enhancing interaction between the motor and a factor, or its association. For example, cyclin-dependent kinase5 (Cdk5) has also been described to regulate fast axonal transport through phosphorylation of the dynein adapter protein Ndel1. It increases Ndel1 association with Lis1, leading to enhanced retrograde transport of lysosomes (Pandey and Smith, 2011). In the same fashion, phosphorylation of JIP1 by JNKs enhances KIF5-JIP1 interactions, thus promotes ante retrograde axonal transport (Fu and Holzbaur, 2013). Cdk5 regulates axonal transport indirectly via inhibition of GSK3β (Morfini *et al.*, 2004). Pathogenic Htt activates JNK3 which in turn phosphorylates KIF5 motor domain and decreases its ability to bind microtubules (Morfini *et al.*, 2009). Finally, organization of motors in clusters could also improve their properties in order to perform better their task. It has been recently shown that dynein re-organize in time during phagosome maturation (Rai *et al.*, 2016) to regulate a switch from bi- to uni-directional motility.

1.2 Motor stoichiometry and organization

1.2.1 Dynein recruitment

The manner in which motors are recruited to the membrane of different vesicles is dependent on the vesicle and the motor involved, but typically the diversity of motor-vesicle interactions is achieved via the help of accessory proteins present on the vesicle membranes. (Granger, 2014). For example, in late endosomes, the Oxysterol-binding protein homologue (ORP1L) binds cholesterol and stabilizes a GTP-bound state of Rab7 and Rab9 proteins, which are prone to recruit a Rab-interacting lysosomal protein (RILP), which in turns recruits dynactin-dynein complex (Johansson *et al.*, 2007; Rocha *et al.*, 2009). More

precisely, the RILP directly interacts with the C-terminal region of p150[Glued] (Johansson *et al.*, 2007). Also, dynein can directly bind to Rab4A via its light chain (Bielli *et al.*, 2001) and to membrane protein Snapin, which participate in late endosome maturation to lysosomes (Cai *et al.*, 2010) On autophagosomes, the association between membrane protein LC3, scaffold protein JNK-interacting protein-1 (JIP1) and p150[Glued] dynactin subunit, is crucial for dynein activation and fusion of the autophagosome with lysosome (Fu, Nirschl and Holzbaur, 2014). The dynein-dynactin complex has been demonstrated to tether via adaptor proteins (Snapin, RIPL, ORP1L, RabGTPase, αIβIII spectrin) in cholesterol enriched domains on the late phagosome. Finally, the dynein light chain LC1, has been shown to directly interact with late endosome and lysosome membrane via LAMP1 (Tan, Scherer and Vallee, 2011)

1.2.2 Kinesin recruitment

The kinesin-1 family, KIF5 motors, and kinesin-2, KIF3 motors, can attach to their cargoes through the KLC, through interactions with adaptor or scaffold and receptor proteins present on the cargo membrane. Different adaptor proteins recruit various members of the kinesin family to different cargoes. For example, KIF3 proteins interact with small Rab GTPase Rab4 on early and late endosomes (Imamura *et al.*, 2003; Bananis *et al.*, 2004; Brown *et al.*, 2005), whereas it interacts with Rab11 on recycling endosomes (Chen *et al.*, 2008; Schafer *et al.*, 2016). For KIF5 motor proteins, lysosomal membrane protein 2 (LAMP2) bridges the motor and the lysosome in neurons (Nakata and Hirokawa, 2003), and Rab6A via BiCD-2 adaptor protein, bridges secretory vesicles to KIF5 motors (Grigoriev *et al.*, 2007). Another core link between KIF5 motors and the lysosomal membrane is the complex made of the small GTPase Arl8 with SifA and kinesin-interacting protein (SKIP) (Rosa-Ferreira and Munro, 2011).

1.2.3 Effect of multiple motors on transport

Due to the complex and crowded cellular environment previously mentioned, a single motor of one polarity (dynein or kinesin), of one family (KIF5 or KIF3) and of one isoform (KIF5b or KIF5c or KIF5a) is hardly enough to haul a cargo for the distance and timing required. Instead, it has been assumed that *in vivo*, cargoes are decorated with a myriad of different kinds of motor proteins simultaneously and each motor protein is present in more than one copy. Having motors of opposing polarity like dynein and kinesin simultaneously present on the vesicle is important for regulating bidirectional transport. Intracellular transport is generally achieved through back-and-forth movement with an overall net directionality towards the proper destination. *In vivo* observations reported that several vesicles undergo bidirectional motility with intermittent pausing (Welte, 2004). Each active transport (retrograde or anterograde) is achieved by one type of motor (dynein or kinesin) and the switch between the activity of these motors remains controversial. Three models can theoretically explain bidirectional transport: the selective recruitment model, the tug-of-war model and the coordination model. In the selective recruitment model, only one type of motor is newly recruited and bound to the cargo at a time. The coordination model suggests

that both kinesin and dynein motors are attached to the cargo but only kinesin or dynein motors are active at any instant of time, with the activity reversed by some cofactor. The tug-of-war model, suggests that both kinesin and dynein motors are active and attach at the same time to the microtubule resulting in a fight followed by one polarity motors (dynein motors, or kinesin motors) stochastically detaching under the opposing force of the other.

The first model has been rejected in several systems: *in vivo* experiments have shown that both motors are present on cargos (Rogers *et al.*, 1997; Murray, Bananis and Wolkoff, 2000). In addition, minus–end motor mutations can alter the plus-end motion of *Drosophila* lipid droplets, which stresses the fact that both motors are attached to the cargo during transport (Steven P. Gross *et al.*, 2002).

The tug-of-war scenario has been confirmed *in vivo* by precise motion analysis correlated with force measurement simulations (Soppina *et al.*, 2009). The switching of motor is accompanied by a reduction of velocity and an elongation of the vesicle, which is consistent with the vesicle being pulled by opposite motors. Furthermore, stepping of 8 nm in both directions, during high force events, has been observed *in vivo* (Hendricks *et al.*, 2012). As the force production of kinesin is greater than dynein's, it has been suggested that bidirectional cargoes are driven by small teams of strong kinesin motors and large teams of dynein motors operating at near force balance. This scenario has been modeled mathematically based on experimental data (Muller, Klumpp and Lipowsky, 2008). This model requires the cooperative detachment of a team of motors under opposing loads. However *in vivo* studies using optical traps and lipid droplets of 300 to 800 nm size in *Drosophila* embryos demonstrated that the dynein detachment rate decreases with increasing opposing load, which does not fit with a cooperative detachment of a team of motors under opposing load. Hence, this study suggests that only motors of one polarity are active on the cargo at any instant of time, which is in contradiction with the tug-of-war model (Leidel *et al.*, 2012). Other studies have shown that the knock down of one motor influences motility in both directions, which is in direct conflict with the 'tug of war' model.

The coordination between motors would involve inactivation of one kind of motor by biochemical means (phosphorylation that would prevent binding of the microtubule domain on the track, phosphorylation of AAA3 for dynein) or physical means (steric hindrance, pushing the motor away from the track). The information transfer between the motors is more likely to happen if the motors are in direct or indirect (via co-factors) physical contact. The most studied mediators for coordination is dynactin: this co-factor of the minus end motor dynein not only enhances dynein motility by stabilizing its interaction with the microtubules, but also initiates motility and recruits dynein at the microtubule interface as discussed in the regulation section (Moughamian *et al.*, 2013; McKenney *et al.*, 2014, 2016; Nirschl *et al.*, 2016). In mammalian neurons, JIP1 directly removes the autoinhibition of KHC and also binds to dynactin which makes a perfect candidate for a master control switch between the two motors (Fu and Holzbaur, 2013). Following the same model, Rho GTPase

Mitochondrial Rho (Miro) and the adaptor protein Milton link KIF5 motors and dynein to mitochondria in a Ca^{2+} manner in neurons (Wang and Schwarz, 2009).

The number of motors of same polarity actively engaged into intracellular transport has been investigated for decades using *in vitro*, and recently *in vivro* techniques. It has been roughly estimated to be 1 to 4 kinesins and 1 to 9 dyneins, using purified vesicles of ~90 nm in diameter (Hendricks *et al.*, 2010) and various methods like single step photobleaching of labeled motors or optical force measurements. Having multiple motors of the same type can increase processivity through cooperation of multiple motors. Indeed, *in vitro* studies showed that the run length of cargoes increase with motor number (Block, Goldstein and Schnapp, 1990; Mallik *et al.*, 2004; Vershinin *et al.*, 2007) while the speed remains unaffected (Derr *et al.*, 2012). For peroxisomes it has been reported that also the speed depends on the number of motors (Kural, 2005; Levi *et al.*, 2006). In line with these results, the force exerted by multiple dynein motors (Mallik *et al.*, 2005) and kinesin motors (Vershinin *et al.*, 2007) is additive *in vitro*, and *in vivo* (Hendricks *et al.*, 2012) providing evidence that motors can cooperate to generate force together. Recent *in vitro* studies have shown that multiple dynein motors could trigger helical motion around the microtubule track, with a net preference for right handed rotation (Can *et al.*, 2014), which has been suggested to be a mechanism used by motor proteins to overcome road blocks during transport (Verdeny-Vilanova *et al.*, 2017a).

1.3 Lysosome as a model system

Different cargos (lysosomes, secretory vesicles, mitochondria, lipid droplets and melanosomes) have different transport requirements and are in many cases transported by a different set of motors. The work presented in this thesis focuses on lysosomes. These organelles were discovered for the first time in 1955 (De Duve *et al.*, 1955) and later imaged by electron microscopy (Baudhuin *et al.*, 1965). Lysosomes are known for a plethora of physiological processes ranging from cholesterol homeostasis, plasma membrane repair, bone and tissue remodeling, pathogen defense, cell death and cell signaling. At the cellular level, lysosome function consists of digesting proteins from the external membrane or from the cytoplasm. In order to receive the materials to be digested from the other endocytic compartments like late endosomes or from autophagosomes, these vesicles need to be motile on the microtubule. Their motility is likely important for encountering and fusing with other vesicles. Indeed, lysosomes are highly mobile vesicles, carrying out bi-directional transport along microtubules. Their high mobility, combined with the fact that they are easy to label using tools like lysotracker, makes them a good model system for studying intracellular transport.

Membrane composition of lysosome

The plasma membrane of eukaryotic cells, and also of cargoes such as lysosomes, is mostly made of lipids (phospholipids, cholesterol, sphingolipids) For lysosomes, its membrane also

encompasses transmembrane proteins such as RabGTPase and carbohydrates. RabGTPase mediates lysosomal trafficking and fusion processes. For example Rab5 and Rab7 are implicated in endolysosomal vesicle trafficking (Rojas *et al.*, 2008; Wang *et al.*, 2011). But more than half of the transmembrane proteins of lysosomes belong to the family of lysosomal membrane proteins (LAMPs) and lysosomal integral membrane proteins (LIMPs). Among the 25 LMPs found up to now, the most abundant LMPs are LAMP1, LAMP2 and LIMP2. LMPs are transmembrane proteins which are dedicated to diverse tasks: LAMP1 and LAMP2 are thought to intervene in the fusion of lysosomes with autophagosomes (Eskelinen *et al.*, 2004), whereas LIMP2 recruits particular hydrolases to the lysosome (Reczek *et al.*, 2007). In addition, LAMP-depleted cells showed a redistribution of lysosomes to the cell periphery, pointing to a role for LAMPs in lysosomal dynamics (Huynh *et al.*, 2007). A recent study has also shown that LAMP1 participates in the regulation of lysosomal exocytosis (Yogalingam *et al.*, 2008). From these observations, LAMPs are suggested to form functional microdomains at the lysosomal membrane that are crucial for lysosome dynamics. Nevertheless, the role of lysosomal membrane proteins is not fully understood yet and only some of their functions have been elucidated.

Certain lipids, such as cholesterol, are thought to form microdomains also called lipid rafts, which are ~10 nm to 300 nm in diameter and enriched in both cholesterol and sphingolipids (Simons, Ikonen and et al, 1997; Pike, 2006; Lingwood, Simons and et al, 2009) Cholesterol can insert between phospholipids and interact with the hydrocarbon chains of the polar head of group of the phospholipids (**Fig 1.3A**). As a result, the polar head groups are more stabilized and decrease in mobility, the local lipid bilayer is therefore less deformable. Another consequence is that the fatty acid chains of phospholipids are less spread apart, leading to a thicker bilayer (**Fig 1.3B**). The sphingolipids have a longer and saturated hydrocarbon tails that insert between phospholipids saturated hydrocarbon chains, and transmit better force between tails (Anishkin and et al, 2013).
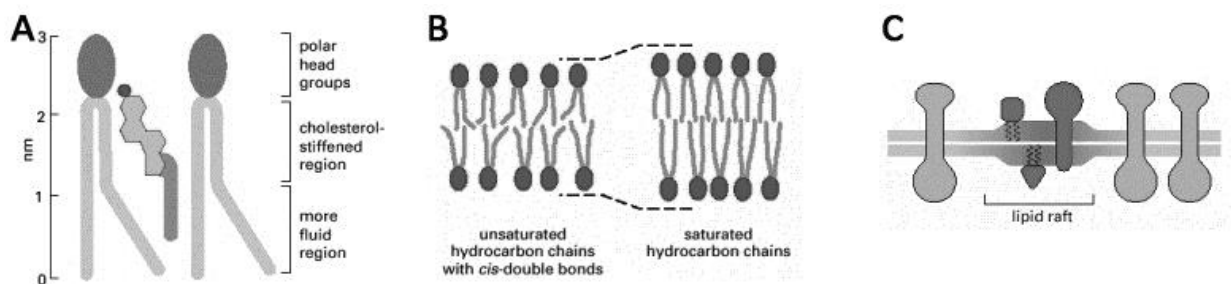
Fig 1.3 Drawing representing the membrane organization at different scale. (A) drawing of cholesterol group, in between two phospholipid groups, stabilizes the phospholipids. (B) Fatty acid chains of phospholipids are less spread apart in saturated lipids, as a result, the layer is thicker. (C) the lipids raft domain has a thicker layer and membrane proteins are stabilized in it.

Lipid microdomains as well as domains formed by transmembrane proteins are important as they can act as platforms to concentrate and cluster motor proteins. Indeed, recent work has shown that cholesterol microdomains are important for clustering of dynein motors on

the membrane of purified large vesicles (late phagosomes) (Arpan K. Rai *et al.*, 2013). In this thesis, we investigate the clustering of motors on smaller vesicles such as lysosomes and in the cell context.

Chapter 2
Single molecule methods for studying intracellular trafficking

"You can observe a lot, just by watching" (Yogi Berra)

Super-resolution fluorescence microscopy techniques are starting to tackle problems that have previously been intractable such as visualizing the architecture of the nucleus (Szczurek *et al.*, 2016) or the neuronal cytoskeleton (Leterrier *et al.*, 2017). The power of the super-resolution fluorescent microscopy techniques resides in their ability to deliver structural information at the nanometer level with molecular specificity and less harsh sample preparation, unlike electron microscopy. In this chapter, I will describe the theory, applications and technological requisites of a single-molecule localization based super-resolution microscopy technique known as Stochastic Optical Reconstruction Microscopy (STORM) [1] which is a technique extensively used in this thesis to study intracellular traffic and mitochondria behavior.

---

[1] The information provided in this chapter can mostly be found in a review publication written by previous members of my laboratory (Oddone *et al.*, 2014) and a book chapter (Oddone,Verdeny et al, 2014)

2.1 From microscopy to nanoscopy

Optical microscopy has been used since about 400 years to visualize cells and sub-cellular organelles. Development of labeling strategies and specific markers opened the door to visualizing specific proteins and cellular compartments with high molecular specificity and high contrast. The non-invasive aspect of fluorescence labeling and imaging makes it possible to image living cells or even living organisms. Key technological developments have improved fluorescence microscopy since its first development. For example, total internal reflection fluorescence (TIRF), confocal and two-photon microscopy methods surmounted obstacles such as background fluorescence and deep tissue imaging. Despite these advances, one major obstacle remained insurmountable until recently: the resolution limit set by the diffraction of light. Since light is a wave, it undergoes diffraction and interference like any other wave. When light passes through an aperture of a given size, such as the objective lens of a microscope, it undergoes diffraction. Hence when light coming from a point sources forms an image, this image is not a point but rather an intensity distribution known as the Airy disk (**Fig 2.1**), and mathematically described as the Point Spread Function (PSF)
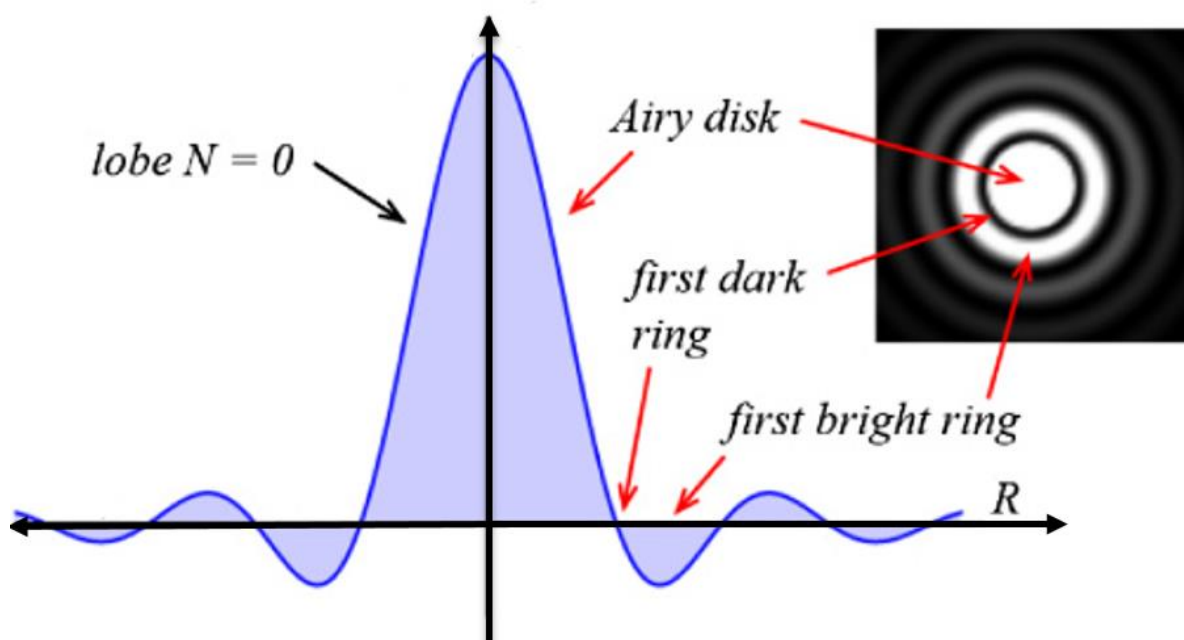
Fig 2.1 Function representing the ideal Airy pattern, with the 2D intensity pattern (center saturated) in the inset. The Airy disk is lobe N=0 (order 0), the first bright ring is lobe N=1 (order1), etc. The normalized intensity distribution of the point source image is also called Point Spread Function.

The width of the first lobe of the Airy disk is related to the wavelength of light and the size of the aperture. Ernst Abbe realized that due to diffraction, two point sources of light could not be resolved if they are closer in distance than $\lambda/(2NA)$ in the lateral (x-y) and $2\lambda/(NA^2)$ in the axial (z) direction, where NA stands for the Numerical Aperture of the microscope objective, λ is the wavelength of light, and n is the refractive index of the medium. At this

distance, the Airy disk coming from the two point sources overlap such that their intensity pattern becomes indistinguishable. For visible light and high NA objectives (ex NA~1.4), the resolution of conventional optical microscopes is ~200-300 nm and ~500 nm in the lateral and axial directions, respectively. The spatial resolution of light microscopy is a limitation for visualizing biological structures, which are often smaller than the diffraction limit (proteins complexes, DNA, mRNA, microtubules, viruses, etc.).

The diffraction limit was finally broken with the development of stimulated emission depletion microscopy (STED) followed by Structured Illumination Microscopy (SIM), Stochastic Optical Reconstruction Microscopy (STORM) and Photoactivated Localization Microscopy (PALM). The principle of STED was first described in 1994 and experimentally demonstrated in 1999 by Stefan Hell (Hell and Wichmann, 1994; Klar and Hell, 1999), SIM was described in 2005 (Gustafsson, 2005), and STROM and PALM methods reported in 2006 (Betzig *et al.*, 2006; Hess *et al.*, 2006; Rust *et al.*, 2006). STED, STORM and PALM can achieve a spatial resolution of ~ 20 nm and ~ 50 nm in lateral and axial directions, respectively. These tremendous technological developments have moved microscopy into the era of "nanoscopy" and are enabling a myriad of new biological applications. The huge scientific impact of super-resolution was recognized by the Nobel committee, which awarded the pioneers of this new field with the Nobel Prize in Chemistry 2014.

In this thesis, I extensively used STORM, which belongs to a group of super-resolution microscopy methods that are collectively referred to as single molecule localization microscopy (SMLM). Below, I will describe in detail the main concepts behind SMLM paying particular attention to STORM.
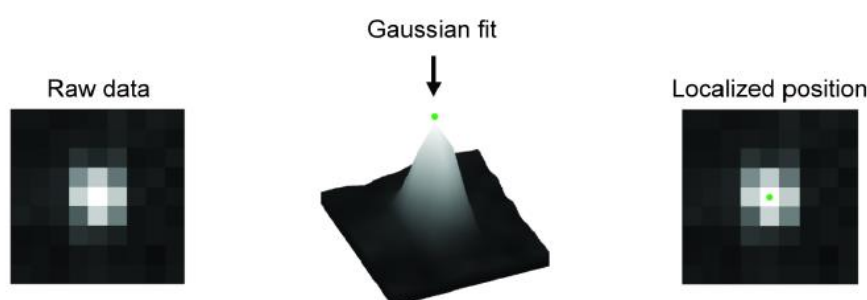

Fig 2.2 Single molecule detection and localization. The image of a single fluorophore in a light microscope is a diffraction-limited spot. By fitting a Gaussian to its intensity profile, it is possible to retrieve the original position of the fluorophore with nanometer precision (green spot). Figure adapted from (Oddone *et al.*, 2014)

2.2 SMLM main concepts

2.2.1 Single molecule localization

A common feature of the SMLM techniques is the ability to precisely localize the position of individual molecules. As previously mentioned, the size of the image of a point light source captured by a camera is determined by diffraction and is in the form of an Airy function. This image is termed the point spread function (PSF) of the microscope. By calculating the centroid of the image, the exact position of the light source can be determined with much more precision than the image itself (Thompson *et al.*, 2002)(**Fig2.2**). Nevertheless the light emitted by two individual, or more, nearby point-like emitters will overlap due to diffraction making it impossible to discern their positions. Therefore, one of the key discoveries making super-resolution possible has been the discovery of photoswitchable fluorophores (Patterson *et al*, 2002; Bates *et al.*, 2005; Heilemann *et al.*, 2005). These fluorophore can be tuned such that they do not fluoresce continuously: they switch between a bright (fluorescent state, also entitled "on" state) and a dark state (non-fluorescent state, also entitled "off" state).

Under adequate condition (for example, high laser power pulses, appropriate buffer conditions), there is a very high probability for a photoswitchable fluorophore to be in the dark state, and a small probability of the fluorophore to be in the bright state. Under good experimental conditions, among a large population of fluorophores, only a spare subset of fluorophores will fluoresce at the same time. The probability that two neighboring fluorophores are in the bright state at the same time is then very small, hence, the fluorophores will be isolated in space. Therefore, the position of each fluorophore can be localized with high-accuracy. Over time, all the fluorophores can be switched on and localized, hence a super-resolution image can be reconstructed from the positions of fluorophores (**Fig 2.3**).
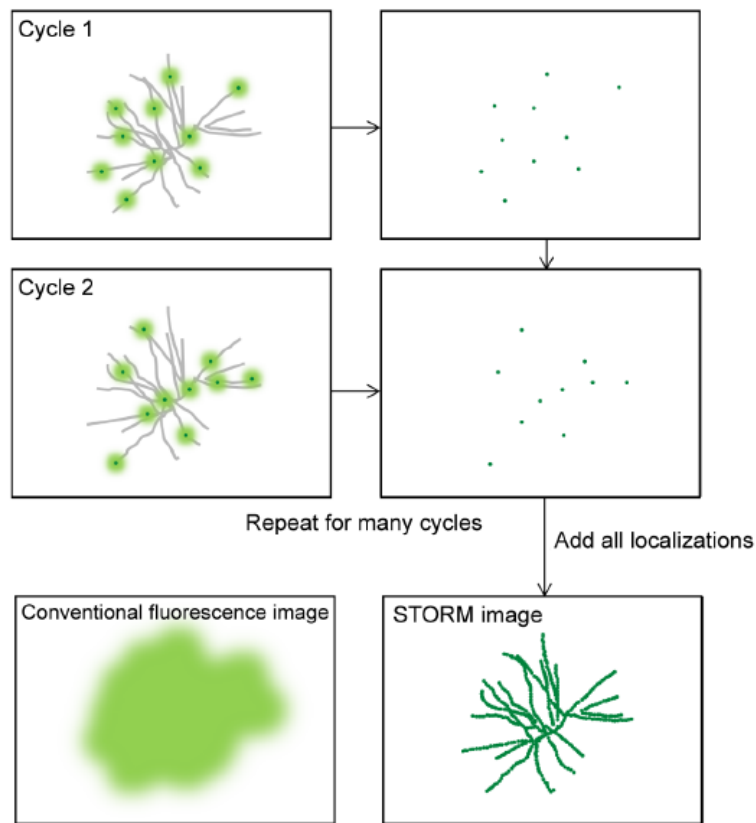
Fig 2.3 Single-molecule localization principle. Schematic showing the general strategy for single-molecule localization microscopy. By using photoswitchable fluorophores, it is possible to turn « on » and image only a few molecules at a time (light green spots). These sparse, single fluorescent molecules are localized with very high precision (dark green spots), tuned « off » (by photobleaching or by switching to a dark state), and a new subset is turned « on ». This process is repeated for several cycles until all fluorophores are localized. Finally, a super-resolution image of the underlying structure can be reconstructed by adding all the localization positions (last panel). Figure adapted from (Oddone *et al.*, 2014)

2.2.2 Spatial Resolution

The resolution, or effective resolution of a super resolution image does not depend on one factor but on many factors that should be optimized: a high localization accuracy, a small probe size, and a high labeling density (Nyquist resolution), a drift corrected image. The contribution of each one of these parameters will be discussed.

Localization accuracy

The location of a single fluorescent molecule can be precisely determined by finding the centroid position of its PSF as long as the molecule is isolated and spatial overlap is avoided. In this case, localization precision depends largely on the number of photons collected from the single emitter. Considering only the error generated from photon counting and assuming the PSF to be of Gaussian shape, localization precision (σ) would be given by

$\sigma = s / \sqrt{N}$, where s is the standard deviation of the Gaussian fit of the PSF and N the number of photons detected. However, additional sources of error such as pixelation noise and background noise generated by CCD (charged coupled device) readout, dark current, or cellular autofluorescence must also be taken into account. Several papers have discussed the fundamental limits to localization uncertainty and proposed different expressions for it (Mortensen et al., 2010; Stallinga and Rieger, 2012; Thompson et al., 2002). Additionally, different computational methods for determining the centroid position, such as nonlinear least squares fitting to a Gaussian PSF or the maximum likelihood estimation (MLE) using a Gaussian PSF model, have been investigated and compared (Abraham et al., 2009; Mortensen et al., 2010; Ober et al., 2004; Smith et al., 2010). It has been shown that, in general, the MLE method is able to determine position with higher accuracy. The latest analytical approximation for localization precision was proposed in 2012 by Stallinga and Rieger (Stallinga and Rieger, 2012):

$$\sigma^2_{LocPrecision} = \frac{s^2 + \frac{a^2}{12}}{N} \left[1 + 4\tau + \sqrt{\frac{2\tau}{1 + 4\tau}} \right]$$

Where s is the width of the Gaussian that is used to fit the PSF, a is the pixel size of the camera dectector, N is the number of photons collected, and τ is a normalized dimensionless background parameter defined as:

$$\tau = 2 * \pi * b * \frac{s^2 + \frac{a^2}{12}}{N * a^2}$$

where b is the number of counts in the background per pixel.

The localization accuracy is an event-dependent. Every time a light emitter blinks (event), its localization accuracy can be calculated based on the number of photon output. Unfortunately, it is almost impossible that the position of the same individual fluorophore, after two consecutive event, is the same. There are indeed additional errors induced by experimental set up (dipole moment, antibody), that can affect the intensity spatial distribution, and by consequence, the center of the Gaussian fit that determines the fluorophore's position. The localization precision of an image cannot be then calculated based on one precise position of an individual fluorophore (localization accuracy), but by taking into account all the positions calculated, of the same individual fluorophore.

An additional property from single fluorescent molecules affecting localization precision is the molecules' orientation as these do not emit light in an isotropic fashion but rather

behave as electric dipoles. This effect is especially important when there is limited or no rotation of the fluorescent emitters during camera exposure, making the shape of the emitter image to deviate from an isotropic distribution. The effect of dipole orientation on localization precision has been previously addressed by simulation experiments accounting for several parameters such as the effective pixel size, the numerical aperture of the microscope objective or the number of photon counts emitted by the molecule (Enderlein et al., 2006). For an effective pixel size around ~100 nm, numerical apertures of 1.2-1.4, and photon counts ranging from 500 to 16000 photons lead to a position determination error of ~10 nm, significantly independent on the orientation of the fluorescent molecule. Moreover, sample labeling for STORM imaging is typically performed with dye labeled antibodies which are not completely fixed on the antibodies, rather they have a certain flexibility in their orientation, thus, they can be approximated as isotropic emitters.

In practice, localization precision can be experimentally determined by measuring the standard deviation or the full width at half maximum of a cluster of multiple localizations originating from a single fluorophore (Huang et al., 2008b; Rust et al.,2006) (**Fig 2.4**). For bright organic dyes such as A647, which is the fluorophore we typically use in our experiments, a localization precision of 8-9 nm is common. Fluorescent proteins, which have lower photon output, give rise to lower localization precision (~20 nm).
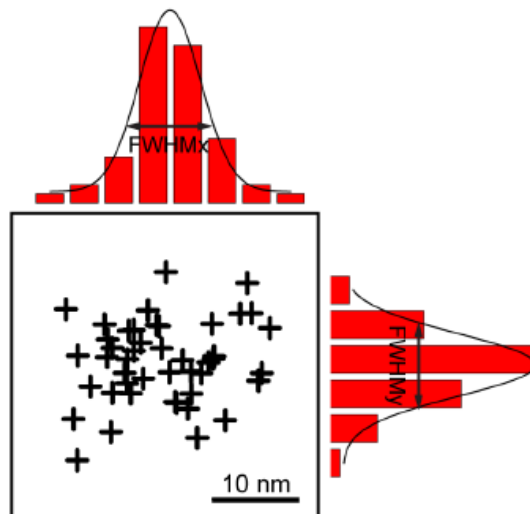
Figure 2.4 Localization precision. Localization precision in (x-y) directions determined from the full width at half maximum (FWHM) of the distribution of multiple localizations originating from an individual fluorophore. Figure adapted from (Oddone *et al.*, 2014)

Labeling density and Nyquist criterion

The labeling density also affects the final spatial resolution. Low labeling densities (not all target molecules labeled) typically cause continuous structures to appear discontinuous, resulting in a loss of detail (**Fig. 2.5**).

The effects of the labeling density on the effective spatial resolution can be quantified by the Nyquist criterion (see Shroff et al., 2008 for further details), which states that structural features smaller than twice the fluorophore-to-fluorophore distance cannot be reliably discerned:

$$\sigma_{Nyquist} = {2}\big/{\rho^{1/D}} \qquad (2.2)$$

Here, ρ is the labeling density calculated as the number of localizations per unit area or volume and D is the dimension of the structure to be imaged (2 for two-dimensional and 3 for three-dimensional STORM imaging). To determine the effective resolution, a common approach is to convolute the contribution due to localization precision and to the labeling density:

$$\sigma_{Effective} = \sqrt{\sigma_{Localization\ precision}^2 + \sigma_{Nyquist}^2} \qquad (2.3)$$

For high spatial resolution, it is essential to obtain an optimal labeling density. Antibody labeling may lead to low labeling efficiency owing to steric hindrance, low affinity of antibodies, or low accessibility of epitopes. Fluorescent proteins are typically introduced via transfection, and several factors can affect the final labeling density, including the presence of unlabeled endogenous proteins and the incomplete maturation or photoactivation of fluorescent proteins (Durisic et al., 2014a). The specific probe that should be used to achieve optimal labeling depends on the target and the availability of high-quality antibodies or fluorescent protein fusion constructs.
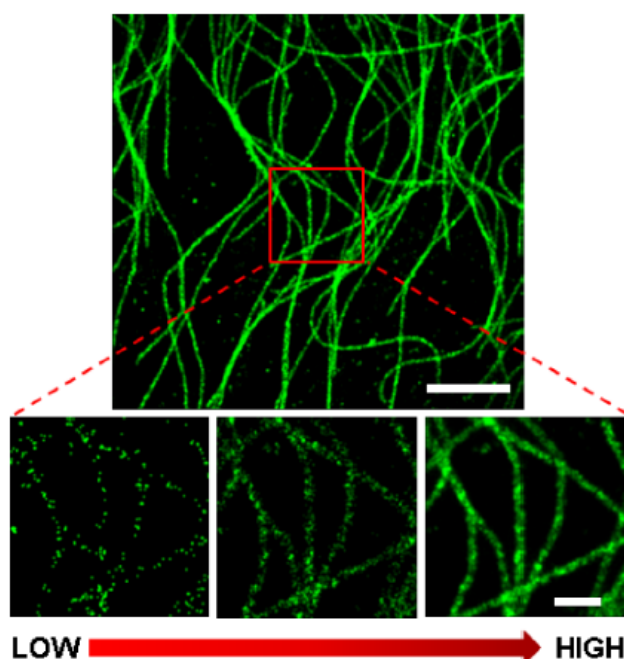
Figure 2.5 Effects of labeling density on effective spatial resolution. Example of a 2D super resolution image of microtubules (large field of view). The scale bar is 2 μm. The red box in the large field of view is shown as a zoom-up below with increasing labeling density (from left to right) as indicated by the arrow. As the labeling density increases, a significant improvement in resolution can be appreciated. The scale bar is 500 nm. Figure adapted from (Oddone *et al.*, 2014)

Probe size

The physical size of the probe (**Fig. 2.6**) has also an effect on how accurately the final super-resolution image resembles the actual structure. This is particularly important for super-resolution methods as the probe dimensions have the same order of magnitude as the achievable spatial resolution. Fluorescent proteins (~3-4 nm) are among the smallest probes although the low photon budget lowers the localization precision and effective resolution. While organic dyes are very small (~1 nm), they are often linked to the target by indirect immunostaining with primary and secondary antibodies (~10-15 nm) creating a rather large probe. The probe size can be substantially decreased via the use of Fab fragments (~5-6 nm) or camelid antibodies (nanobodies, ~4 nm) (Ries et al., 2012). Alternatively, organic dyes can be introduced into the cell via SNAP, CLIP or HALO tag technology, resulting in a probe size similar to that of fluorescent proteins. Direct labeling (e.g., with membrane- or organelle-specific markers, DNA-binding dyes, or via click chemistry) will further reduce the probe size.

The work presented in this thesis have been realized using the antibody strategy because of the robustness, well-established protocols and the availability on the market of good dyes.
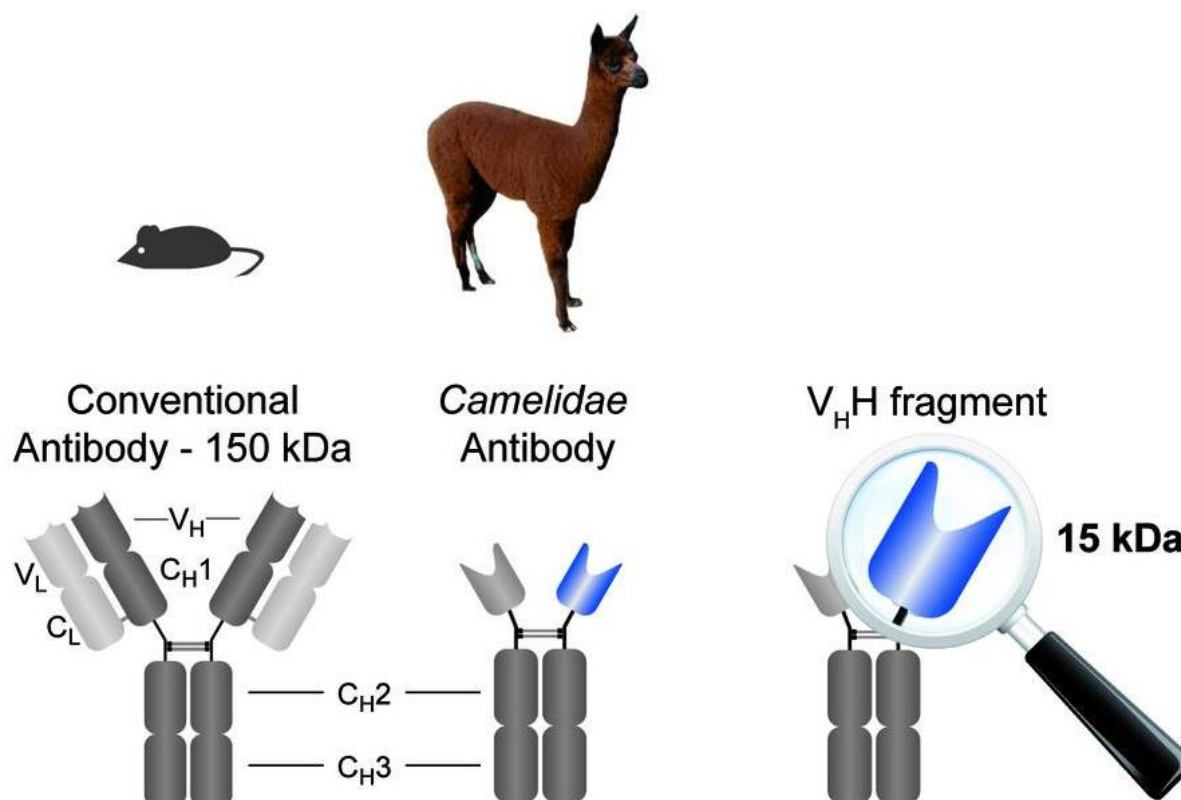
Fig 2.6 Probe size affects spatial resolution. Schematic comparison of the size of different types of probes. Left : conventional antobodies (~10-15 nm, 150 kDa) are made of a heavy chain domain(C_H1, C_H2, C_H3 and V_H), a variable light chain domain (V_L) and a constant light chain domain (C_L) and an antigen binding site. Right : nanobodies (blue), also termed V_HH fragments (~4 nm, 15 kDa). Adapted from chromotek website.

Drift Correction

Lateral and axial drift occur during the acquisition due to thermal motion in the mechanical parts of the microscope, especially the stage. Since STORM provides nanoscale resolution, even small amounts of drift in the few tens to hundreds of nanometer range will compromise image resolution. There are several ways of correcting drift. For example, fiduciary markers such as fluorescent beads can be added to the sample and their position can be tracked over the course of the experiment. The drift can then be corrected by shifting the localizations based on the initial position of the beads. Alternatively, the super-resolution experiment can be split into frames of a given window size (e.g. 1000 frames assuming that the drift is negligible in this small subset of frames). A super-resolution image can then be reconstructed from these subsets of frames. The reconstructed super-resolution images are then correlated with the one reconstructed from the initial frame window to correct for drift.

. Insight3 drift correction algorithm, previously described, is based on direct cross correlation calculation between images reconstructed periodically. The minimum roots mean square error for this drift technique was evaluated to 3.39 nm. In a recent article this algorithm was refined using a redundant cross correlation approach, which output a root mean square error of 1.56 nm (Wang *et al.*, 2014). The drift correction depends on the signal to noise ratio of the blinks, and the density of blinking in each frame. For a low number of blinks per frame the drift is harder to calculate. The drift correction based on redundant cross correlation was found to work more efficiently in these conditions so we implemented this algorithm in MatLab. in our group based on the open source code (the original code can be found here: http://huanglab.ucsf.edu/Resources.html)

2.3 STORM technological evolution

Different technological developments have allowed SMLM techniques such as STORM to be expanded to a wide range of applications such as multi-color imaging, 3D imaging, live-cell imaging or correlative imaging among others. Some of these applications will be extensively used in the experiments reported in this thesis.

2.3.1 3D imaging

Most biological structures are three-dimensional, thus, it is important to be able to visualize these structures in 3D and with high spatial resolution. Although there are several methods for extending SMLM to three dimensions, one of the simplest methods is to use a cylindrical lens placed in the detection path to introduce astigmatism. The astigmatism approach is also the one we use in our lab for 3D STORM imaging. This method can yield an axial resolution of 50-60 nm over a range of ~800 nm (~400 nm above and below the focal plane) (Huang et al., 2008b). Due to astigmatism, molecules that are exactly in the focal plane appear circular, whereas molecules above or below the focal plane appear elongated either horizontally or vertically, depending on the orientation of the astigmatic lens (**Fig.2.7**). With proper calibration, the ellipticity of each localization can be converted into an amount of displacement above or below the focal plane. The calibration can be performed using a piezoelectric stage and a glass coverslip with diffraction-limited, fluorescent microspheres sparsely adsorbed onto the glass surface. By acquiring a series of images at fixed z-steps, a calibration curve relating z to the width (in either x or y) of the PSFs can be generated. This calibration curve can then be used to calculate the z-position of subsequent single-molecule localizations acquired using the same system (**Fig.2.7**). See reference (Huang et al., 2008b) for additional details. Additionally, it is also possible to combine astigmatism with a dual-objective geometry in order to capture more photons and improve the z-resolution to about ~20 nm at the expense of imaging depth (Xu et al., 2012).
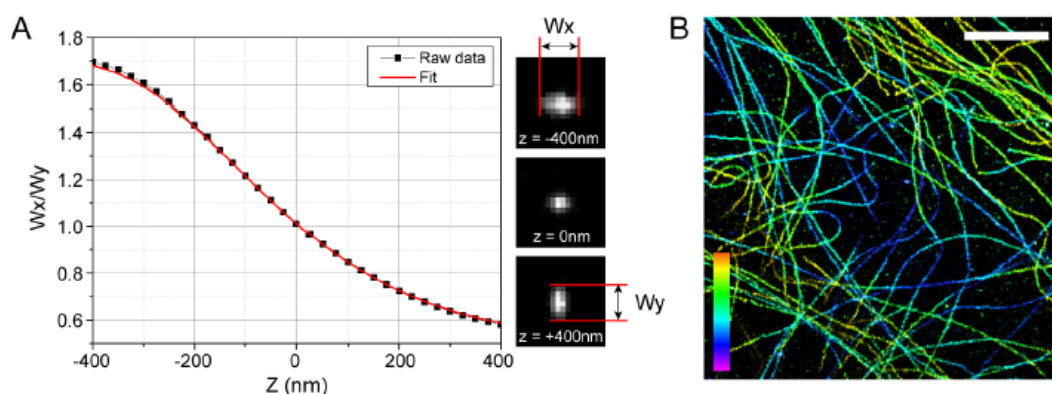
Figure 2.7 3D STORM imaging (A) 3D STORM imaging using the astigmatic lens approach. The z position of each raw data point is calculated by measuring the width in the x and y directions (Wx and Wy) and then by comparing the measured values to the calibration data. Representative molecules for various z positions are shown, which appear elongated because of the presence of an astigmatic lens placed before the camera. (B) 3D STORM image of microtubules acquired with the astigmatism approach. The color scale bar represents the z-position (between -400 nm in magenta and 400 nm in orange). The scale bar is 5 µm. Figure adapted from Ione Verdeny Vilanova doctoral thesis.

2.3.2 Multi-color imaging

Recent years have seen a tremendous amount of technological development in single molecule based super-resolution microscopy methods such as STORM (Jans *et al.*, 2013; Lakadamyali, 2014). Multi-color imaging is an important capability of fluorescence microscopy since it allows for a determination of colocalization and interaction between different sub-cellular structures. STORM imaging was extended to multiple colors soon after its initial discovery (Bates *et al.*, 2007; Cattoni *et al.*, 2013). However, the various approaches used for multi-color STORM imaging have important caveats. These caveats lead to decreased resolution and increased complexity as the number of colors is increased. One approach for multi-color STORM uses fluorophore pairs in which the same reporter is coupled to different activators (Cattoni *et al.*, 2013). In this case, the color is determined based on the wavelength of the activating laser light. By using pulses of activation laser light with different wavelengths, it is possible to color-code the resulting localizations based on when they turn on during the imaging cycle (Cattoni *et al.*, 2013). This approach is free from chromatic aberrations and the need for image registration since all colors are acquired in the same image channel. However, it is prone to color cross-talk (10-20%) (Bates *et al.*, 2007) since fluorophores can also undergo spontaneous activation, independent of the activation pulse, or alternately, fluorophores can be activated by the ''wrong'' activation pulse. A second approach uses spectrally-distinct reporter dyes coupled to the same (or different) activator dyes (Bates *et al.*, 2007). A variation of this second approach also exists that uses spectrally-distinct photoswitchable reporter fluorophores alone without an activator dye (dSTORM) (Mitra and Lippincott-Schwartz, 2010). The advantage of these

approaches is that color cross-talk can be reduced or eliminated (**Fig 2.8**). However, chromatic aberrations can be difficult to correct at the nanoscale level (Jeon *et al.*, 2000). More importantly, there is a limited availability of spectrally distinct photoswitchable fluorophores with favorable photophysical properties. Differences in the duty cycle and brightness of different fluorophores can impact the relative resolution of the images in the different color channels. In particular, the best fluorophore can only be used once. A detailed analysis of a large number of photoswitchable fluorophores showed that AlexaFluor647 outperforms fluorophores leading to images with the highest resolution (Berthier *et al.*, 2012). The necessity of spectrally distinct fluorophores has been circumvented by a new approach combining spectral and position acquisition (Zhang *et al.*, 2015). The spectral mean of the emission wavelength of individual bright fluorophores such as Alexa647 showed a very small standard deviation (less than 5 nm). The spectral mean has been used to distinguish different fluorophores whose emission spectra was heavily overlapping on one side, and the position of the fluorophore has been determined on the other side. This technique named spectrally resolved STORM (SR-STORM) has been extended to 3D, 4 colors STORM, in order to study peroxisomes, mitochondria, microtubule and vimentin filament in fixed cells. This technique was initially developed with two opposite objectives but has been adapted to an inverted objective, even though, the spectral mean difference is greater (20nm) due to the loss of photons by splitting the beam in two (Yan *et al.*, 2018). An important issue in all multicolor techniques based on different dyes is related to the imaging buffer environment. Indeed the dye blinking could be optimized when it is in a certain chemical environment (later explained). The optimal chemical environment is dye dependent, which makes often difficult to find conditions compatible with all fluorophores at the same time.
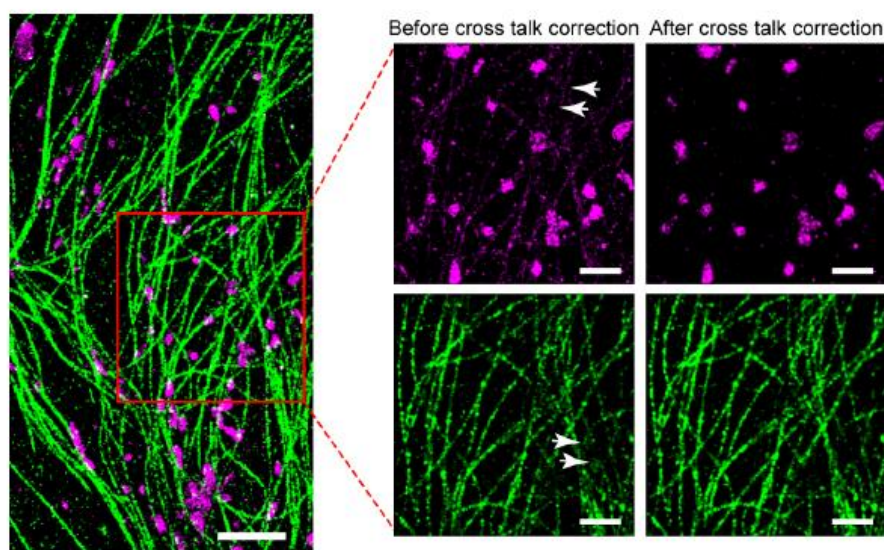

Figure 2.8 Multi-color STORM imaging. STORM image of microtubules (green) and lysosomes (magenta). Zoom-up of the red boxed region show microtubules and lysosomes before and after

cross talk removal. White arrows show examples of false color assignments that are corrected by the cross talk removal procedure. The scale bars are 2 μm (large field of view) and 1 μm (zoom-ups). Figured adapted from Ione Verdeny Villanova thesis

2.4 Experimental considerations

2.4.1 Suitable probes

One of the main requisites for super resolution microscopy is a light source tunable in time. The light emitter should be tuned such that they do not fluoresce continuously: they switch between a bright (fluorescent state, also entitled "on" state) and a dark state (non-fluorescent state, also entitled "off" state).

Photoswitchable probes

The probes used for SMLM can be classified into three categories: fluorescent proteins, small synthetic dyes, and quantum dots. Interestingly, different SMLM techniques have been associated to different kind of probes; therefore PALM and fPALM are generally associated with photoswitchable fluorescent proteins, whereas STORM, dSTORM are generally associated with photoswitchable fluorescent dyes.

While in the "on" state, one can excite an atom or atomic arrangement (typically, the chromophore region of proteins is made of aromatic rings, where pi bond are frequents) with a photon at a specific wavelength (**Fig 2.9**). The resulting excited state will last ~10^{-9}s, after which the electron (the one delocalized in the pi-bonds in the case of aromatic ring) returns to a ground state, and the energy released by de-excitation is radiative, so that it will result in the emission of a fluorescent photon. The corresponding wavelength of the emitted photon is longer than the one used to bring the electrons to the high energy level (i.e. to the excited state). This shift towards longer wavelength is referred to as Stokes Shift. The electronic energy transition does not change in electron spin, which results in short-live excited state. The atomic arrangement of the chromophore, responsible of the fluorescence, can be found in nature: all the fluorescent proteins are derived from corals, algae, jellyfish proteins and synthetized. The electronic environment as well as the spatial arrangement has a large influence on the fluorescent capacities of the chromophore.

The "off" or dark state, in which the fluorophore is not able to fluoresce, could be reached in many different ways. For example if the fluorescent dyes oxidize, and thus by creating a new bond, it would change its electronic configuration and as a consequence disabling any fluorescence. The introduction of a reducing agent (a compound that will get oxidized instead of the fluorophore) such as primary thiol (β-mercaptoethanol [BME]) or cysteine [MEA], ascorbic acid (Benke and Manley, 2012), or a phosphine (Vaughan *et al.*, 2013) is an essential step in the buffer preparation. Indeed thiol could also be used to bring reversibly the fluorescent dye to a dark state. For example, primary thiol binds to cyanines like A647 or Cy5 (Graham T Dempsey *et al.*, 2009), bringing them to a non-fluorescent dark state that can be reversed under excitation of its activator A405. A spatial change in the atomic

arrangement could also lead to dark state : cyanines aromatic rings could be found in cis or trans configuration. Another reversible mechanism involving dark non-fluorescent state is the addition of a proton to a fluorophore, such as in the case of fluorescin. (Fürstenberg and Heilemann, 2013). Dark states often appear as precursor states for photobleaching: the radicals (anions or cations) formed, in the dark state, are very reactive, and tend to create chemical bounds with species present in the environment. By creating a new bound, it changes the electronic configuration of the molecule, and avoids the molecule to reach an excited state.
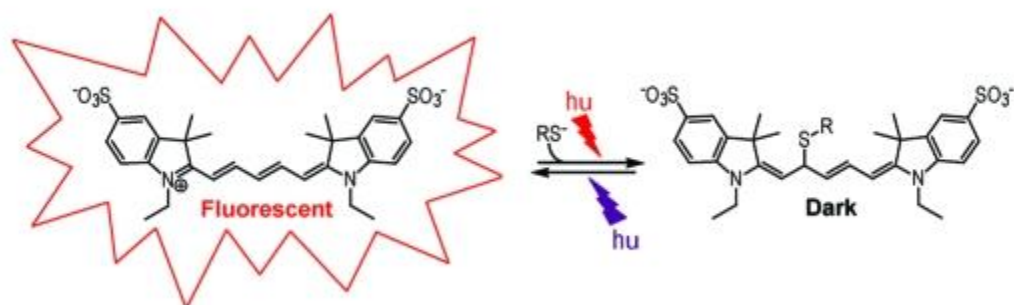

Fig 2.9 Photoswitching mechanism for cyanine dye (AlexaFluor647). Upon high power illumination (~1 kW/cm^2) with a laser matching the excitation wavelength of the dye and with the help of a reducing agent such as a primary thiol (RS$^-$), the dye is force to a non-fluorescent, dark state. Illumination with a low power of ultraviolet (UV) will bring the dye back to its fluorescent state. The A647 is generally coupled with A405 in a activator-reporter fashion. Then the UV excite the A405 dye which in turns reactivate A647. Figure adapted from (Graham T Dempsey *et al.*, 2009)

Fluorescent proteins

Inside the photoswitchable fluorescent protein family we can distinguish the fluorescent proteins used in SMLM that are photo-activated (from a resting dark state to an active fluorescent state) and the ones that are photo-converted (they undergo a change in their emission spectrum) by light. Under UV illumination, photoactivatable fluorescent proteins such as PA-GFP and PA-mCherry (Patterson and et al, 2002; Subach *et al.*, 2009) irreversibly go from a dark state to a bright state transitions whereas photoactivable fluorescent protein such as EYFP, rsEGFP, Dronpa (named after the Japanese word meaning disappearance of a ninja), and Dreiklang (Moerner *et al.*, 1997; Habuchi *et al.*, 2005; Biteen *et al.*, 2008; Brakemann *et al.*, 2011), can switch reversibly to the fluorescent form. The second kind of photoswitchable fluorescent proteins includes photoconvertible proteins, which already emit fluorescence, but upon illumination with UV light, their emission spectrum shifts, usually from green to red emission (Dendra2, mEos2, mKikGR) (Wiedenmann *et al.*, 2004; Gurskaya *et al.*, 2006; Habuchi *et al.*, 2008; McKinney *et al.*, 2009; Zhang *et al.*, 2012)

Organic dyes

Many dyes are organic compounds, which means their structure is made of carbon atoms, these may be natural or synthetic, and they are smaller (3 nm) than fluorescent proteins.

The most popular organic dyes for SMLM are derived from 3 compounds: cyanines (Cy5, Cy5.5, Cy7, Alexa Fluor® 647,etc.), rhodamines (Alexa Fluor® 488, Alexa Fluor® 532, Alexa Fluor® 568, ATTO488, ATTO565) and oxazines (ATTO655, ATTO680,etc.) (van de Linde, Heilemann and Sauer, 2012; Fürstenberg and Heilemann, 2013) (**Fig 2.10**). In STORM experiments, fluorescent dyes such as A647, Cy5.5 and Cy7 (reporter dye) are often paired with a second fluorophore (Alexa Fluor®405, A488 or Cy3) in order to increase the switching efficiency between dark and fluorescence state. The reporter-activator pair is also extensively used for multicolor imaging (Bates *et al.*, 2007, 2012). It is now known how the activator dye, when excited with appropriate wavelength, will transfer its energy in a non-radiative way to the dark-state reporter, which in turn, will recover the fluorescent state (**Fig 2.9**).
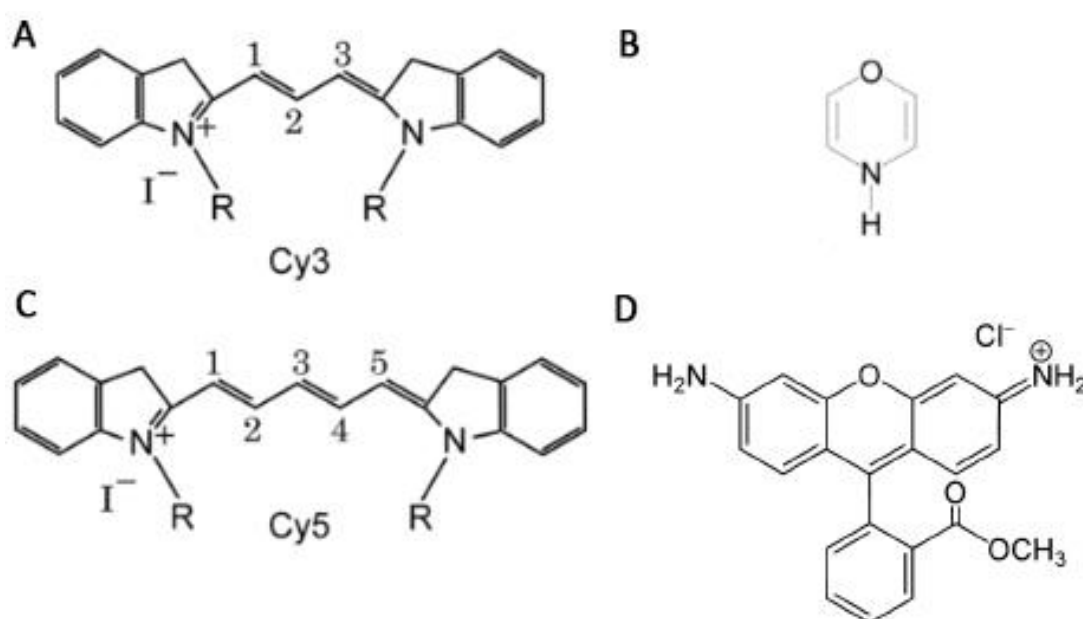
Fig 2.10 Chromophore structural motif of photoactivable cyanine3 & photoactivable cyanine5 respectively (A&C), oxazine (B) and rhodamine(D)

2.4.2 Probe properties

The probe is a decisive factor to take into account during the experiment design. Even if the range of available fluorophores available on the market expands each year, only a few of them are frequently used in SMLM experiments. Depending on the aim of the experiment, one have to pay attention to a few parameters. For multicolor imaging, the probes excitation and emission wavelength should not overlap for example. Also, in live cell experiments, the photostability and cytotoxicity of the probe should also be taken into account. The quantum dots are the more stable fluorophore but also the most toxic. The labeling strategy is a crucial information into the choice of the probe: labeling in live cell is much more difficult than labeling in "intact cells", or "fixed cells". For live cell imaging, a strategy consists in transfecting the cell with a DNA sequence of the protein of interest

merged with the DNA code for a fluorescent protein, creating a mutant protein. Nonetheless, the cellular expression of the protein may not be regulated and could lead to artefact (overexpression, the folding of the protein could be altered due to the size of the fluorescent protein, etc.). Recently another strategy using Crisp-cas9 technology could replace precisely a DNA segment, allowing screening endogenously expressed fluorescent proteins. Another way to label endogenous intracellular proteins is to use organic dyes and an immunostaining approach. Unfortunately the antibodies are very difficult to internalize, thus in this case, an hybrid approach involves genetically encoded tags such as SNAP, CLIP and HALO tags, and a small fluorophore-labeled synthetic component binding the tag (Jones *et al.*, 2011; Staff, Benarroch and Klein, 2011; van de Linde, Heilemann and Sauer, 2012). The cell squeezing technique forces the cell membrane to disrupt allowing large molecules to enter the cell through a hole in the disrupted membrane (Kollmannsperger *et al.*, 2016). The cell recovers its membrane after squeezing. Click-chemistry allows small modified fluorophores containing an azide-group to bind to DNA/RNA with no toxic by-products (Zessin, Finan and Heilemann, 2012). Among the long list of considerations, three main factors could change drastically the output of SMLM experiments.

Brightness

The number of photons emitted by a fluorophore is of utmost importance since it is inversely proportional to the precision with which a single fluorescent molecule could be localized (Thompson, Larson and Webb, 2002). A high photon emission directly correlates with the shape of the intensity profile, which is in turn, fitted to precisely position the fluorophore. The localization accuracy was described in section 2.2.2. The brightest fluorophores available on the market now are Atto565, Cy5.5, Cy3 and A647 (Dempsey *et al.*, 2011). On the other hand, the number of switching cycles and photostability could compensate for a low photon yield. Indeed each time a fluorophore blinks (with a certain photon yield), its position can be determined. The more blinking resulting from a fluorophore (that is to say the more switching cycle), the more localization positions will be output from the individual fluorophore. Then the distribution of the localizations originating from the same fluorophore will be fitted with a Gaussian function, which will be used to determine precisely the fluorophore's position. So the more localizations, the better the distribution is, and by consequence, the best the Gaussian fit is. As a result a high number of switching events (blinks) leads to a better knowledge on the position of the fluorophore (i.e., localization accuracy). Atto565 for example emits a high number of photons but it photobleaches very fast, which results in a low quality STORM image. This is because Atto 565 renders very precise localizations positions (due to its high photon yield) but a low number of localizations positions (due to photobleaching), so the total distribution of the localization positions are fitted by a Gaussian with less accuracy.

On/Off Duty Cycle

The duty cycle is defined as the time a fluorophore spends in the bright state (or "on" state) over the time the fluorophore spends in the dark state (or "off" state). The best candidates

have a low duty cycle meaning that the fluorophore spends most of its time in the dark state. Indeed, at any given time, the probability that the PSF of two close fluorophore overlaps, increases if the fluorophore spends a long time in the bright state (Dempsey *et al.*, 2011). In the three-dimensional STORM experiments, the fitting of the blinks is less robust and more blinking events are rejected of the analysis due to poor fitting. A way to avoid the blinking to be rejected is to make sure that the directs neighbors will not blink at the same time. In the case of high duty cycle, the probability of two neighboring fluorophores to blink at the same time is higher, so a strategy is to slightly reduce the labeling density of the sample. If two fluorophores are present on a structure of interest and their blinking overlap (they blink at the same time), their intensities profile won't be fitted, and they would not be part of the analysis. As a result, the structure of interest will not appear in the final STORM image. Whereas if there is only one fluorophore on the structure of interest (lower labeling density), the fluorophore blink won't be altered by any neighbor, but the structure, due to under-labeling, may appear incomplete. Thus, there is a balance to find between labeling density and duty cycle. Another strategy to deal with the duty cycle is to use appropriate imaging buffer conditions. Chemical reagent can force the fluorophores to stay for a long time in the non-fluorescent dark state, reducing thus, the duty cycle.

Switching kinetics

The excited state last ~ 10^{-9} s for each fluorophore, which means that in 1 second, if the fluorophore stays in the bright "on" state, it could in theory emit hundred millions of transitions between excited and ground state (i.e. emit a hundred millions of photons). Experimentally, this is not the case, the fluorophore goes to dark state before, and the time it stays in a fluorescent state is called a switching event, emitting between 500 to 20 000 photons, depending on the excitation power and the quantum yield of the fluorophore. For SMLM the faster a fluorophore goes to the dark state, the better. Indeed, the ideal is to capture a switching event per frame, so probes with faster switching rates allow faster data acquisition rates and shorten the time needed to acquire a super-resolution image (Dempsey *et al.*, 2011). This is an essential property for live cell imaging, in order to avoid blur. The advantage of organic dyes is that the excitation laser intensity directly correlates with the switching kinetics. For example, a classic laser density for STORM imaging using A647 is 1 kW.cm^{-2}, and for live STORM imaging, the density required is twenty times higher (Jones *et al.*, 2011) with the same fluorophore. On the other side, fluorescent protein switching kinetics is lower and they behavior is not correlated with the excitation laser intensity (Jones *et al.*, 2011).

To conclude, a high photon yield, low duty cycle, high photo stability are the main characteristics for the ideal fluorophore probe for SMLM in order to achieve high quality images. A fast switching rate is needed for live experiments and a low toxicity is always better.

2.5 Technical considerations for STORM

The STORM technique needs practical requirements from the experimental setup component to sample preparation, image acquisition or data analysis. This considerations have been well described in the literature (Rust *et al.*, 2006) and PhD theses from Ione Verdeny Vilanova, and Mark Bates.

2.5.1 Microscope Components

In order to have the best quality STORM images, here are a list of technical considerations to follow

- TIRF or inclined illumination geometries are often used to minimize unwanted background and maximize signal to noise ratio. The illumination profile should be homogenous in lateral and axial directions if possible

- An active autofocusing system is also important to keep the sample in focus and prevent z stage drift during data acquisition.

- A high quality TIRF oil-immersion objective, with high magnification (100x or higher) high numerical aperture (1.4 or higher)

- Laser intensities of at least 1 kW.cm^{-2} are used to activate, and bring to the dark state the fluorescent protein and organic dyes. For live-cell STORM imaging, laser intensities should be at least 20 kW.cm^{-2}

- An acousto-optic tuneable filter(AOTF) to perform rapid switching between different illumination wavelengths for pulsed activation/excitation. By turning on and off, the AOTF will act as a shutter. An acousto-optic modulator (AOM) for a specific frequency could also be used.

- An EMCCD camera, or a sCMOS camera to detect the signal. sCMOS have larger field of view but require a tedious calibration. EMCCDs are cheaper and faster.

The complete description on the experimental set up used in this thesis can be found in the **Appendix**. Notably companies such a Nikon are developing their own system, NSTORM©. Some of the experiments were done using the NSTORM© system.

2.5.2 Sample preparation

The sample preparation requires a high degree of attention since the structure observed could degrade easily. In case of fixed cells, the fixation protocol needs to be carefully chosen depending on the structure imaged. Usually paraformaldehyde (PFA) is used to crosslink the intracellular components and create a matrix maintaining the cell intact. The caveat of this fixation protocol is that some amino acids from the epitopes may react with the aldehyde group of PFA in order to create covalent bonds, and thus impeach the antibody to recognize the epitope. Alternatively, a rapid incubation of cold (-20ºC) mixture of methanol and ethanol also maintain cell structures intact, even though, it could damage membrane

structure. This last method is based on the azeotropy property of the mixture. To ensure the fixation method is efficient, control experiment should be done. It consist in fixing and staining the cell and then acquire a short STORM image. Then add and remove PBS in order to mimic a second immunostaining procedure and perform another STORM on the same region of interest. Compare both images, they should match. Also the immunostaining procedure should yield a high efficiency in order to respect the Nyquist criterion, and on the other hand, avoid nonspecific binding. The use of a blocking buffer prevent nonspecific binding from the antibodies, and the secondary antibodies are decorated with a high activator-to-reporter dye ratio. Usually there are 2 to 3 activators per reporter to achieve optimal photoswitching. The concentration of antibody depends on the affinity of the antibody and should be optimized in order to prevent background or unspecific binding. To sum up, the sample preparation is a trade-off between a good preservation of the structure of interest, a high labeling density and low background due to unspecific binding.

The sample preparation protocol used in this thesis are described in detail in the **_Appendix_**.

2.5.3 Imaging buffers for photoswitchable fluorophores

The sample to be imaged needs to be incubated into a buffer mixture in order to facilitate photoswitching of the fluorophores. Each fluorophore has its own optimized imaging buffer. The components may be the same, but the ratios are different. One of the main components is a primary thiol, a compound that contains a carbon-bonded sulfhydryl, which reacts with the dye to quench the triplet state or put the dye into a non-fluorescent state (dark state, See 2.4.1 section) (Graham T. Dempsey _et al._, 2009; Ha and Tinnefeld, 2012). β-mercaptoethylamine (MEA) is suitable for cyanine dyes in a single color STORM, whereas β methyl ester (BME) better suits for multicolor imaging. In order to prevent the dye to get oxidized (turning it to a permanent non fluorescent state), an oxygen scavenger system such as glucose oxidase could be used. The pH should also be controlled since photoswitching show better results under slightly basic pH conditions (between pH=6.5 and pH=7.5 for cyanine dyes). The by-products of the oxygen scavenger system lowers considerably the pH, thus a strong buffer such as PBS is needed to maintain the pH stable during the image acquisition. The recipe of the imaging buffer used in this thesis is detailed in the **_Appendix_**

2.5.4 Post processing

A crucial step into SMLM is the post processing of the data, especially in STORM. Hundred thousands of images need to be analyzed and the information collected in each of these images should be gathered into a single super resolution image. The data analysis is generally performed after the acquisition, and follow by three main steps:

Step 1: Single molecule identification

In order to separate the signal from the background, a threshold is set so that each pixel should have a minimum intensity to be taken into account (**Fig 2.11**). On the other hand, the signal coming from a single emitter should be separated enough from any signal from other emitter; otherwise the intensity profile wouldn't be correctly fitted. For dense blinking images, typically for live STORM, algorithm have been developed in order to accept these signals and handle them (Huang *et al.*, 2011; Min *et al.*, 2014).
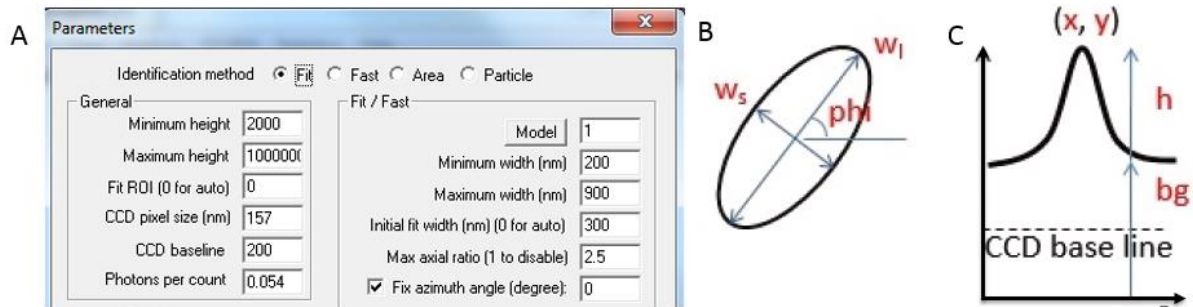

Fig 2.11 General parameters used for single molecule indentification. The photons reaching the camera sensor are converted into "counts". (A) The Minimum height and maximum height, the background (bg) as well as (B) the maximum width (W_l) and minimum Width (W_s), the angle, and the maximal axial ratio (W_l)/ (W_s), the Region of Interest (ROI) needs to been defined by the user. Inside the ROI, for each pixel its counts are sustracted to the average counts of the 4 pixels on its corner. (C) The counts number is fitted in (x,y) by a Gaussian and the center of the Guassian is used to determine the position of the fluorophore

Step *2: Localization, filtering and data processing*

Once the signal has been identified, it should be fitted in order to determine its precise position. The signal could be fitted by a Gaussian model of the PSF using either the nonlinear least square method or a MLE method, both have similar results. The MLE method takes better into account the Poison noise (i.e. noise from the background autofluorescence), whereas the least square method takes better into account the Gaussian noise (i.e. noise from the camera) (Brede and Lakadamyali, 2012). In order to achieve the best resolution, filters are applied to the selected signal. The brightness, the width, the orientation of the signal (horizontal or vertical) have threshold that filters out the signal coming from artefacts or background (**Fig 2.11**). Due to the temporal stochasticity of the blinking, the signal may fluoresce in various consecutive frames. Thus, the same pixel could be linked in consecutive frames in order to be considered as part of the same switching event of the emitter. Last but not least, the lateral and axial drift is also corrected. It could be corrected using fiducial markers such as microspheres as reference, or by splitting the data into subsets of frames (Betzig *et al.*, 2006; Bates *et al.*, 2007).

Step3: Image rendering

The last steps consist in render in 2D or 3D each localization into a single superresolution image. For a 41μm by 41μm field of view, a STORM image can gather up to 15 million of

localizations. In order to be able to see them correctly, the localizations could be displayed as crosses or as Gaussians dots, which intensity is correlated to the localization precision (Rust *et al.*, 2006).

Programs for STORM data analysis

Unfortunately, there is not yet a unified, open source, generalized program to analyze STORM data. The software (Insight3) used by our laboratory is the one historically developed while STORM was developed in Harvard laboratory, written by Dr. Bo Huang. Nevertheless, GraspJ was developed in our laboratory to analyse STORM data based on MLE method, RapidSTORM is an open source software freely available as well. For very dense labelled sample, DAOSTORM has been successfully developed for 2D and 3D data (Babcock, Sigal and Zhuang, 2012; Min *et al.*, 2014). A recent review compare various single-molecule localisation algorithms (Small and Stahlheber, 2014). The detailed parameters used for STORM analysis in this thesis, are listed in the ***Appendix***

Chapter 3

Correlative live cell and super-resolution microscopy

« Progress in Science depends on new techniques, new discoveries and new ideas, probably in that order » Sydney Brennet

Recently, super-resolution microscopy methods such as multicolor STORM have enabled visualization of subcellular structures simultaneously below the optical resolution limit. However, due to the poor temporal resolution, these methods have mostly been used to image fixed cells or dynamic processes that evolve on slow time-scales. To overcome this limitation, we have recently developed a correlative and sequential imaging method that combines live-cell and super-resolution microscopy[2]. However, this correlative imaging approach remained low throughput with low success rate when performed manually. In the first part of this chapter, I will describe a microfluidic based approach that improves the throughput of correlative microscopy. I will further demonstrate an application of the microfluidic platform by correlating mitochondrial dynamics, morphology, and nanoscale mitochondrial protein distribution in live and super-resolution images[3].

 Further, various approaches for achieving multicolor STORM have important caveats. Color cross-talk, limited availability of spectrally distinct fluorophores with optimal brightness and duty cycle, incompatibility of imaging buffers for different fluorophores, and chromatic aberrations impact the spatial resolution and ultimately the number of colors that can be achieved. In the second part of the chapter I will describe a simple approach for multi-color STORM imaging using a single fluorophore and sequential labeling that overcomes several limitations. At last, I will present a simple method to locate the same region of interest on different days and even on different microscopes. In combination, these approaches enable cross-talk-free multi-color imaging of sub-cellular structures.

---

[2]This work has been published as an article named '*Cross-Talk-Free Multi-Color STORM Imaging Using a Single Fluorophore*', Johnny Tam, Guillaume Alan Cordier, Joseph Steven Borbely, Ángel Sandoval Álvarez, Melike Lakadamyali . Published: July 7, 2014. https://doi.org/10.1371/journal.pone.0101772

[3] This work has been published as an article entitled '*A Microfluidic Platform for Correlative Live-Cell and Super-Resolution Microscopy*', Johnny Tam, Guillaume Alan Cordier, Štefan Bálint, Ángel Sandoval Álvarez, Joseph Steven Borbely, Melike Lakadamyali Published: December 29, 2014 https://doi.org/10.1371/journal.pone.0115512

3.1 Correlative live-cell and super-resolution imaging.

3.1.1 Live-cell and super-resolution imaging

For live-cell imaging, the temporal resolution of the imaging set-up must be faster than the dynamics of the biological process being imaged. In the case of STORM, temporal resolution is limited by the number of frames needed to build a super-resolution image with a given spatial resolution. The camera frame rate, the photoswitching rate of fluorophores and ultimately phototoxicity limit the temporal resolution.

Fluorescent proteins are typically used for live-cell imaging since they are genetically encoded, but because of their low photon output and slow switching kinetics, the spatio-temporal resolution is limited to 60-70 nm and tens of seconds (Shroff *et al.*, 2008). The organic dyes are brighter and photoswitch faster. 25 nm spatial and 0.5 s temporal resolution was demonstrated using A647 combined with SNAP tags, (Jones *et al.*, 2011). However, high laser intensities are required to photoswitch fluorophores fast enough to achieve this spatio-temporal resolution and hence phototoxicity becomes problematic.

In summary, the temporal resolution can be improved often at the expense of spatial resolution and increased phototoxicity. For more details the reader is referred to a recent review (Lakadamyali, 2014)

3.1.2 Correlative imaging

As defined by K.A Jahn and D.A Barton, "correlative microscopy is the use of two or more microscopy techniques preferably with different spatial and/or temporal resolutions – to characterize the same region of interest in a sample" (Jahn *et al.*, 2012). The information could be structural, morphological, chemical or dynamic, depending on the tool used. Some examples of correlative microscopy include correlative light and electron microscopy (CLEM) and correlative light and atomic force microscopy (AFM) (Janel *et al.*, 2017). Our laboratory developed an approach combining wide field fluorescence microscopy for live cell imaging with STORM. The dynamic information could be captured with the live cell imaging and correlated with the structural information at the nanometre level given by STORM (Bálint *et al.*, 2013; Verdeny-Vilanova *et al.*, 2017b)(**Fig 3.1**). The correlative live-cell and super-resolution imaging approach has been extensively used in this thesis and will be described in detail.

3.1.3 An all optical correlative live-cell and super-resolution microscopy approach

Most cellular dynamics occur at fast timescales (millisecond) and achieving both nanoscale spatial and millisecond temporal resolution is still very challenging using super-resolution microscopy methods (Lakadamyali, 2014). To circumvent this problem, recently, our group developed an all-optical correlative imaging approach that combines time-lapse live-cell microscopy with STORM to achieve both high temporal resolution and high spatial resolution, respectively (Bálint *et al.*, 2013). This approach has enabled us to study cargo transport dynamics at the level of single microtubules, revealing how microtubule

intersections impact motor protein mediated transport. In principle, this approach can be extended to study other subcellular processes in which it is necessary to interpret dynamic information in the context of ultrastructural information. However, the technique requires precise delivery and removal of fluid from a sample that remains on the microscope stage for the duration of the experiment, a procedure that, when performed manually, is imprecise, labor-intensive, and time consuming.
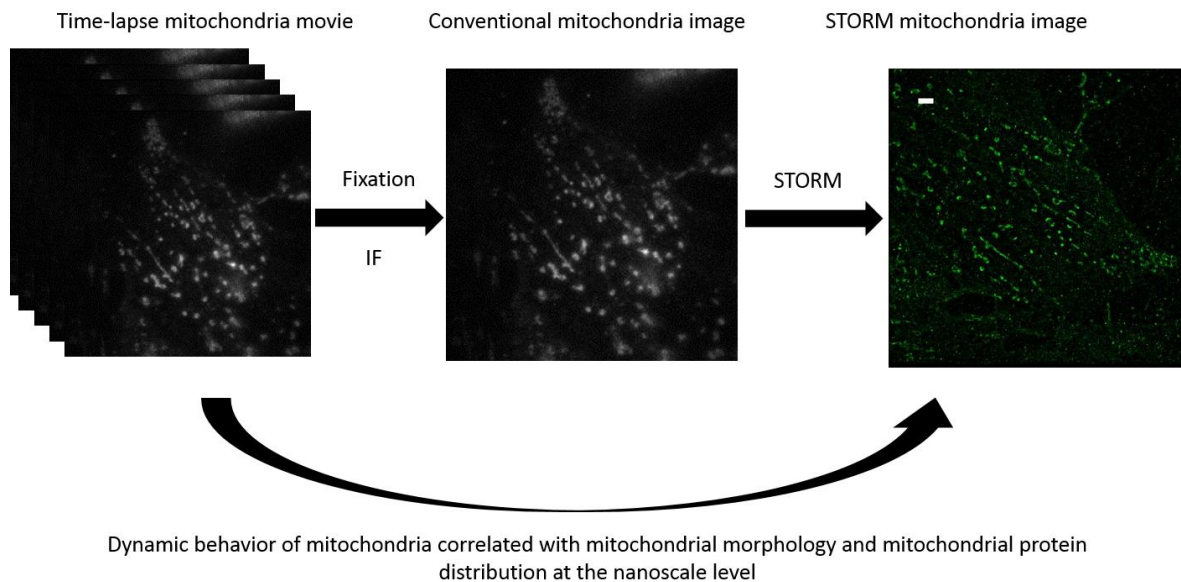

Dynamic behavior of mitochondria correlated with mitochondrial morphology and mitochondrial protein distribution at the nanoscale level

Fig 3.1 Workflow of the all optical correlative live-cell and super-resolution imaging approach. A live-cell time-lapse movie of mitochondria is recorded at high temporal resolution. The sample is then fixed *in situ* and stained with antibodies conjugated with photoswitchable fluorophores for immunofluorescence (IF) and super resolution imaging (STORM). A STORM image of the mitochondria is then recorded. Live-cell movie are precisely aligned with the STOM image of the mitochondria using fiducial markers. The scale bar is 2um.

3.2 A microfluidic platform to increase STORM throughput and permits rare cellular event observations

To streamline and automate the sample preparation between live-cell imaging and super-resolution microscopy, we took advantage of PDMS-based microfluidic devices. While sophisticated options exist for automated immunostaining of mammalian cells (Whitesides, 2006; Cheong, Paliwal and Levchenko, 2010), we decided to use an approach with external valves and a very simple modular design that is cost-effective and easy to adopt. Our microfluidic chip for adherent mammalian cell culture yields miniaturized imaging chambers that are still large enough to contain a high number of cells that can form a confluent monolayer under healthy growth conditions. It is also compatible with live-cell time-lapse imaging, STORM, and other inverted microscopy techniques. We have carried out extensive optimization of sample preparation protocols that are specific to super-resolution imaging

(fixation, immunostaining, and imaging buffers) to achieve optimal labeling densities, optimal photoswitching of fluorophores, and ultimately, optimal resolution in the reconstructed STORM images. To demonstrate the capabilities of the system, we systematically evaluated and categorized the dynamic behavior of mitochondria and correlated these dynamics with mitochondrial morphology and mitochondrial protein distribution at the nanoscale level. Mitochondria are essential for the health of neuronal cells, and changes in mitochondrial dynamics as well as morphology have been shown to occur in neurodegenerative diseases such as Multiple Sclerosis, Parkinson's, Alzheimer's, Huntington's, Lou Gehrig's, and Schizophrenia (Chen and Chan, 2009; Nikić *et al.*, 2011; Lovas and Wang, 2013). However, identification of mitochondrial changes can be potentially confounded by the natural variability in morphology, dynamics, presence of mutations in mitochondrial DNA, maintenance of membrane potential, and even nanoscale distribution of membrane proteins (Collins *et al.*, 2002; Chan, 2006; Detmer and Chan, 2007; Nikić *et al.*, 2011; Wurm *et al.*, 2011; Plucińska *et al.*, 2012; Jans *et al.*, 2013). The ability to characterize and correlate the dynamics and ultrastructure of a large number of organelles has the potential to allow detailed screening of disease pathologies.

3.2.1 Microfluidic design and workflow

There are a wide variety of microfluidic chip designs that have already been demonstrated for optical microscopy and/or immunostaining of bacteria and mammalian cells (Whitesides, 2006; Cheong, Paliwal and Levchenko, 2010; Cattoni *et al.*, 2013), many of which utilize a multi-layered design with on-chip valves (Unger *et al.*, 2000; Cheong, Paliwal and Levchenko, 2010). For simplicity and ease of use, we utilized a single-layered microfluidic chip manufactured using polydimethylsiloxane (PDMS) bonded to a glass coverslip (**Fig. 3.2** and see *Appendix*). Direct implementation of established protocols in these devices for cell seeding, immunostaining, and STORM imaging buffers resulted in very low cell concentrations, poor labeling densities, and complete absence of the photoswitching of fluorophores that is necessary for STORM. These poor results could be attributed to two key factors. First, during cell seeding, the density of cells in suspension dramatically decreases when the diameter of the tube through which the cells flow is small, an effect that is commonly observed in blood cells flowing through capillaries, and referred to as the Fahraeus-Lindqvist effect (Fåhræus and Lindqvist, 1931). This problem was overcome simply by increasing the cell seeding density by a factor of about 30. Second, most sample preparation protocols are optimized for the materials polystyrene and glass, which have significantly different material properties than PDMS (Berthier *et al.*, 2012). The biggest challenge is that PDMS tends to absorb small molecules (Toepke and Beebe, 2006), thereby changing the local concentration of some (but not all) reagents in an unpredictable manner. We overcame these problems by systematically testing and determining the optimal concentration for the reagents used in immunostaining and STORM imaging buffers (see *Appendix*).
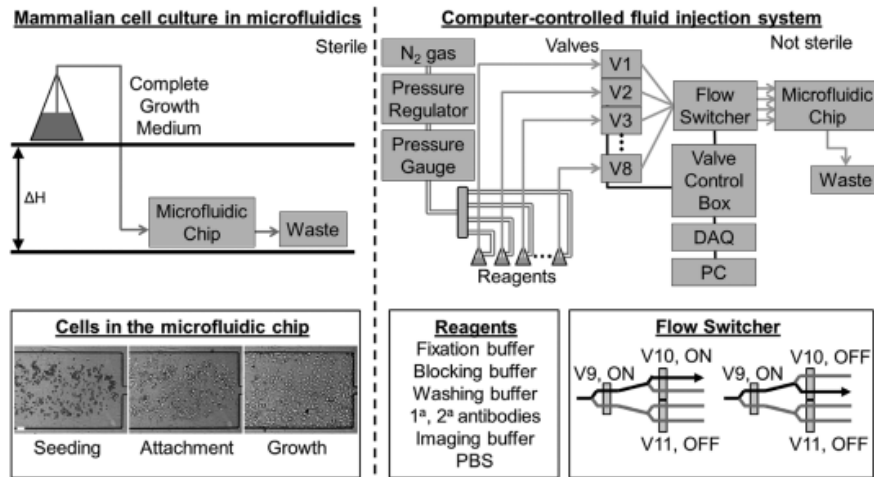
Fig 3.2 Design of microfluidic platform. Left, top : The cell culture is performed under steril conditions. The flow is established using gravity-driven flow and the flow rate is adjusted by changing the value of ΔH. Left, bottom : Cells are introduced into the microfluidic chip (seeding), allowed to attach (attachment), and then maintained under steady, continuous perfusion (growth). Right, top : during the data acquisition phase, the chip is removed from the sterile environment, placed on the microscope stage, and connected to a computer-controlled fluid delivery system. The number of reagents can be adjusted by adding or removing valves. Pressurized air is coupled to reagents which are routed through the system using solenoid pinch valves. Right, bottom : each reagent can be delivered to each channel in the microfluidic chip through a binary multiplexer tree. By adjusting the configuration of the valves, fluid can be routed to different channels (shown are two examples). A total of *n-1* three-way solenoid valves are needed to split the incoming fluid from one channel to *n* channels.

After optimizing mammalian cell culture, sample preparation, and imaging conditions, we were able to obtain labeling densities and imaging buffer conditions that allowed both single and multi-color super-resolution imaging with an image resolution of up to 23.8 nm (average image resolution of 37.5 nm) in the lateral directions (as determined from localization precision and Nyquist criterion for label density) (**Fig. 3.3**). The combined system enabled fully-automated immunostaining. Samples prepared using the automated system showed no differences when compared to samples prepared manually (**Fig. 3.3**, prepared using the automated system).
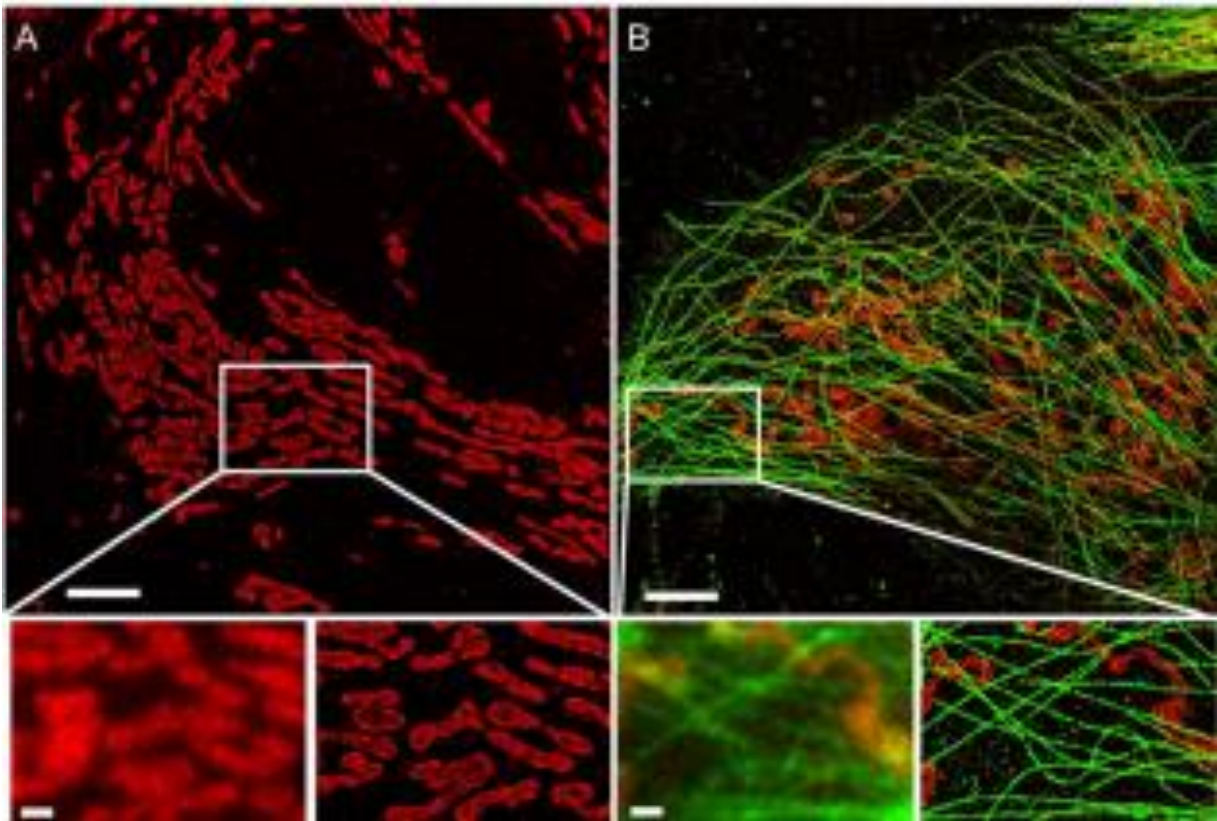
Fig 3.3 STORM microscopy in microfluidic chambers. Samples were prepared using a setup for automated immunostaining. (A) One color STORM image of mitochondira (Tom20). (B) Two-color STORM image of mitochondria (Tom20) and microtubules (alpha-tubulin). In both panels, the zoomed region shows the same region imaged using conventional epifluorescence microscopy (left= and STORM (right). Scale bars, 5 µm in top images, and 1 µm in bottom images (zoomed regions)

By adding an additional fluid channel containing a fixative solution, to allow for computer-controlled on-stage fixation, we extended the system to perform correlated live-cell and STORM experiments in multiple colors based on a crosstalk-free sequential imaging approach (Tam *et al.*, 2014) (**Fig.3.4**).

Fig 3.4. Correlative microscopy using microfluidics. Microtubules and mitochondria were imaged sequentially using epifluorescene microscopy and STORM. The live imaging examples from various time points selected from a sequence of live cell images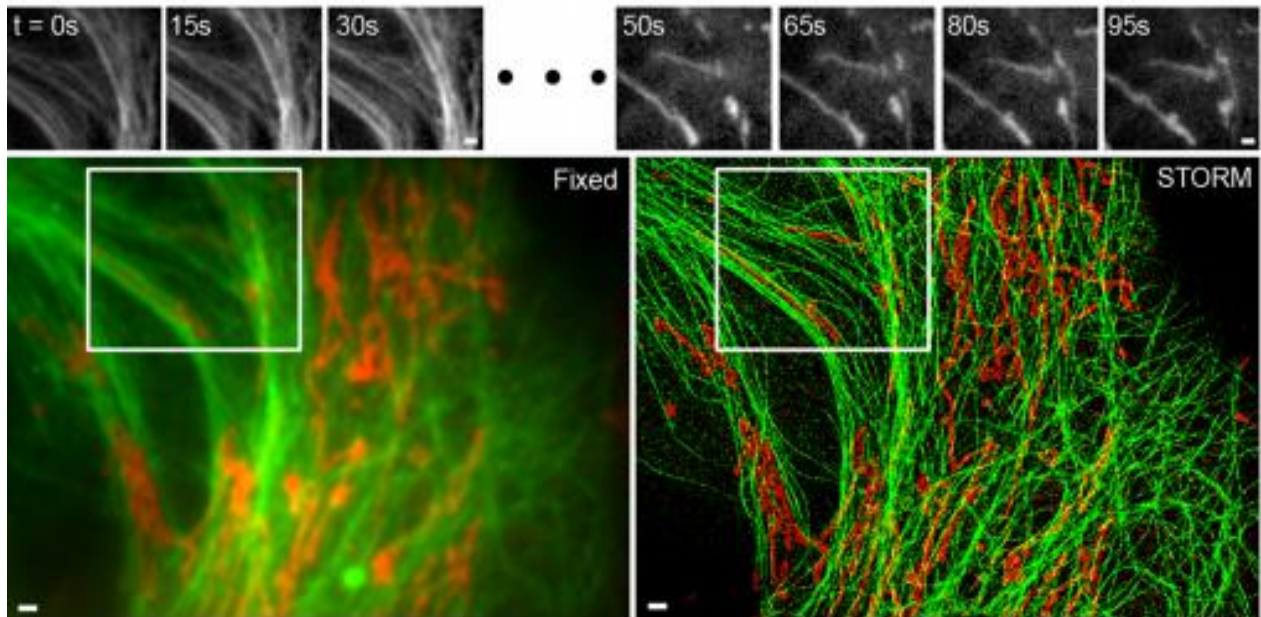 acquired at 100 ms per frame (top) are from the region inside the white boxes (bottom). The experimental sequence was as follows : live-cell imaging of microtubules (top left), followed by live-cell imaging of mitochondria (top right), on stage automated fixation, automated immunostaining of mitochondria, epifluorescence imaging of mitochondria (bottom left, red), STORM of mitochondria (bottom right, red), automated immunostaining of microtubules, epifluorescence, epifluorescence imaging of microtubules (bottom left, green), and STORM imaging of microtubules (bottom right, green). Since the STORM images were acquired sequentially, fiduciary beads were used to align and merge the two images. Scale bars, 1 μm.

The automated system eliminated the most time-consuming, labor-intensive, and technically-challenging steps required for correlative live-cell and super-resolution microscopy and significantly reduced the amount of time needed for human supervision and manual input.

3.2.2 A rare observation of mitochondrion membrane fusion and fission

To validate the robustness and utility of the system, we applied this platform to investigate mitochondrial dynamics by correlating live mitochondrial dynamics with mitochondrial morphology and protein organization in STORM. We carried out a total of 28 correlative live-cell super-resolution experiments in a time period of about 65 hours with high quality data in 21 out of 28 experiments (75% success rate). In correlative microscopy, the cell imaged for time-lapse microscopy has to be the same cell imaged in STORM. Therefore, it is not possible to select the best labeled cell for STORM imaging, which is the common procedure when fixed cells alone are imaged. Since there is always a level of variability in immunostaining (regardless of the use of microfluidic devices), there are instances in which the cell selected for time-lapse imaging will have less than optimal labeling density for

STORM. The experimental time we could achieve using the microfluidic devices was a significant improvement compared to manual throughput of one experiment per day. Most importantly, the immunostaining was carried out unsupervised. The correlative imaging enabled us to investigate the relationships between dynamics, size, and protein distribution at the level of individual organelles for a large population of mitochondria. Even though mitochondrial dynamics (in particular mitochondrial fusion and fission) have previously been imaged using live-cell STORM at a temporal resolution of few seconds, one important advantage of the correlative approach is the much lower laser power densities used for live imaging (0.2 to 0.5 W.cm^{-2} of 561-nm light was used as opposed to 10 kW.cm^{-2} of 561-nm light used in live-cell STORM (Shim *et al.*, 2012)). Given that mitochondria are especially fragile organelles which fragment easily due to photodamage (Mitra and Lippincott-Schwartz, 2010), laser intensity is an important consideration. A second advantage of the correlative imaging approach is the fact that even with the extremely low laser power densities used; we could still probe rapid and transient dynamic processes that take place in millisecond time scales, which is not possible with live-cell STORM. Finally, no imaging buffer or oxygen scavenger system was required for the live cell imaging. Cells were maintained in complete growth medium during live cell imaging (see **Appendix**). These considerations help to minimize any undesired perturbations to the cell or to the mitochondria. We identified a total of 577 mitochondria (357 in wild type cells and 220 in cells stably expressing GFP-tubulin) (**Fig. 3.6** and **Appendix**) that could be clearly discerned both in a live video showing mitochondrial dynamics up to the point of fixation, as well as in a high resolution STORM image. Here, it was important to utilize the STORM image to distinguish between closely-spaced mitochondria, to discern their size, and to examine the distribution of proteins along their membrane, details that were obscured due to the diffraction-limit in epifluorescence microscopy utilized for live-cell imaging.

We first investigated the characteristics of mitochondrial dynamics. Each mitochondrion was assigned to one of three categories: stationary (S), undergoing a slow, but dynamic motion (dynamic-slow, D-S), or undergoing a fast translation across the cell (dynamic-fast, D-F). The dynamic of a single mitochondrion belonging to one of these categories is very distinct (**Fig 3.5**). Dynamic slow and static mitochondria had similar average speeds (~310 nm.s^{-1}), but could be distinguished based upon whether or not they were confined to a region within the cell. Static mitochondria were confined within a smaller region (total displacement =192±91 nm determined from the first 500 frames of the time lapse movie) compared to the dynamic slow mitochondria (total displacement =414±261 nm determined from the first 500 frames of the time lapse movie, p=0.00038). Dynamic fast mitochondria underwent processive, directed motion and reached an average speed of 700 nm.s^{-1} during these periods.
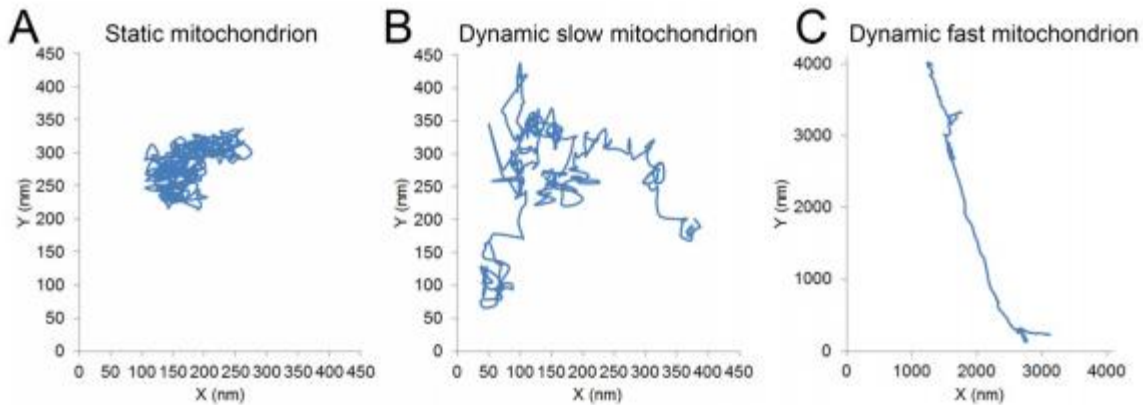
Fig 3.5 Representative trajectories for the static (A), dynamic slow, (B) and dynamic fast (C) categories of mitochondria. The trajectories of the static and dynamic slow mitochondria correspond to the first 500 frames (25 seconds) of the time-lapse movie. The trajectory of the dynamic fast mitochondrion corresponds to the period of directed, processive motion (293 frames, 14.65 seconds).

Once defined, the categories were used to distinguish the different mitochondria behavior (**Fig.3.6**).
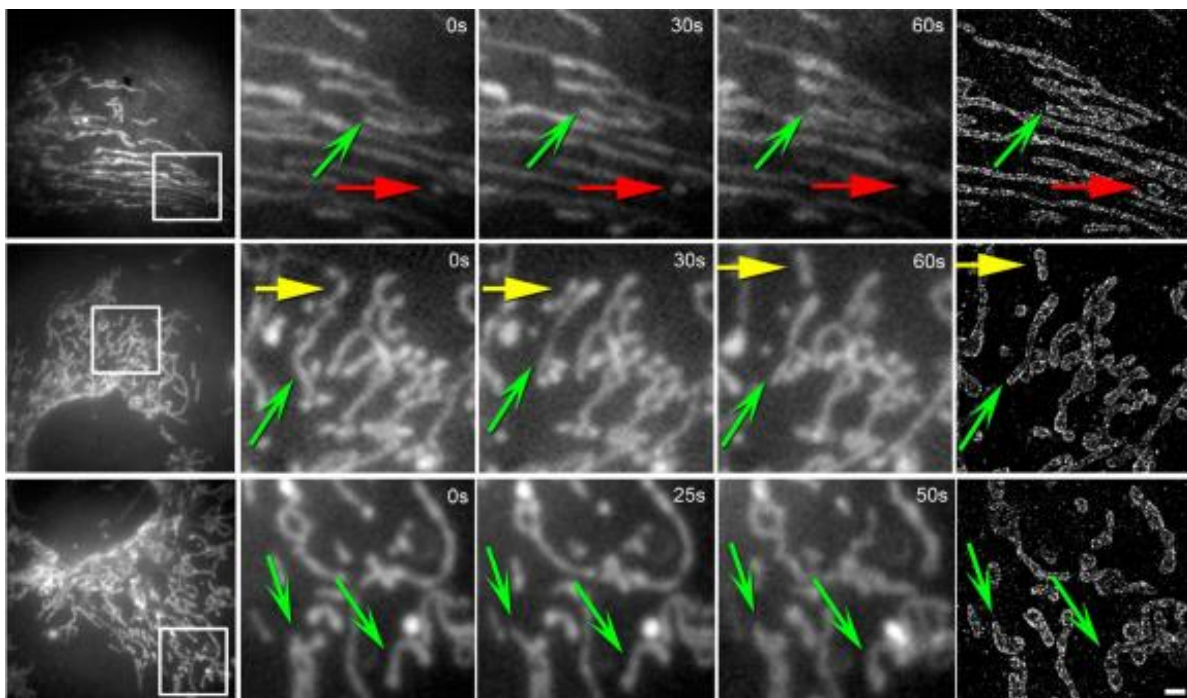
Fig 3.6. Examples of mitochondria events observed using correlative live-cell and super-resolution microscopy in a microfluidic device with a fluid delivery system for computer-controlled fixation and immunostaining. Each row represents one dataset, showing a region of interest within the cell at three different time points selected from a sequence of live cell images acquired at 50 ms per frame during live-cell imaging followed by the STORM image (from left to right). In each dataset, mitochondria were systematically identified and categorized based on their dynamic category using both the STORM image and the live-cell video. Examples of dynamic categories are labeled using

color-coded arrows (red=static, green=dynamic-slow, yellow = dynamic-fast; sharp arrowhead = interacting, flat arrowhead = isolated). Scale bar, 1 μm.

Stationary mitochondria appeared to be docked and single particle tracking showed that their motion was confined to a region around 192±91 nm (total displacement in the first 500 frames of the time lapse movie). Dynamic-slow mitochondria appeared to shift back and forth and moved within a larger range of 414±261 nm in the same time period. While they did not show processive, directed translocation in the cell, often the mitochondrial morphology underwent dynamic changes. Finally, dynamic-fast mitochondria were those organelles that underwent a net processive translocation (1570 nm on average) from one part of the cell to another part, reaching an average speed of ~700 nm.s^{-1} during periods of processive motion, consistent with motor-protein mediated active transport along microtubules. The majority of mitochondria underwent the dynamic-slow motion (83.5%), followed by a small fraction of stationary (10.5%) and dynamic-fast (5.9%) mitochondria. To further characterize the types of interactions that occurred between mitochondria, we also determined whether each mitochondrion contacted other neighboring mitochondria (interacting), as opposed to remaining completely isolated from all other mitochondria (isolated). The majority of mitochondria were interacting (71.6%) as opposed to isolated (28.4%). It is possible that the low spatial resolution of conventional microscopy leads to an overestimation of the interacting category, since a fraction of the mitochondria that appear to overlap in conventional microscopy may actually not touch each other at the superresolution level. Interestingly, the majority of interacting mitochondria were those that belonged to the dynamic-slow (**Table 1**) category. In contrast, both stationary and dynamic-fast mitochondria tended to be isolated.

	Stationary	Dynamic-slow	Dynamic-fast
Interacting	10 (2.8%)	241 (67.5%)	6 (1.7%)
Isolated	27 (7.6%)	61 (17.1%)	12 (3.4%)

Table 1 Distribution of mitochondrial dynamics

Next, mitochondrial size determined from STORM images was correlated to mitochondrial dynamics obtained from the live-cell videos. Mitochondria that were dynamic-slow or interacting were larger in size when compared to all other categories (p<0.001) (**Fig. 3.7**). Furthermore, dynamic-fast mitochondria were on average smaller than stationary mitochondria (p<0.001). Together, this data suggests that mitochondrial size, dynamics, and interactions are not independent parameters, but rather, related to each other.

We also examined whether the membrane distribution of mitochondrial protein Tom20 was related to mitochondrial dynamics. Protein distribution is not necessarily constant across all mitochondria and can depend on different factors. For example, a previous study found variations in Tom20 levels across mitochondria based on the position of these mitochondria relative to the nucleus (Wurm *et al.*, 2011). Since Tom20 is an outer membrane protein, we wondered if its distribution is also sensitive to the shape changes experienced by the

dynamic-slow or dynamic-fast mitochondria. Tom20 density (number of Tom20 localizations per unit area) showed a broad distribution within each dynamic category. There was not a statistically significant difference in the mean Tom20 density across the different dynamic categories (**Fig. 3.7**). This result indicates that the distribution of Tom20 is not sensitive to mitochondrial dynamics. Finally, to demonstrate that this kind of streamlined and automated correlative imaging and analysis can be applied to screen changes in mitochondrial dynamics, morphology, and protein distribution we compared these parameters to cells stably expressing a GFP-tubulin marker. Since dynamic mitochondria are likely associated with microtubules, we wondered if over-expression of GFP-tagged tubulin could alter the correlations in the dynamic and static categories that we observed in the wild type cells. Overall, the distribution of mitochondrial dynamics was similar between wild-type and transfected cells (**Table 2**).

	Stationary	Dynamic-slow	Dynamic-fast
Interacting	8 (3.6%)	134 (60.9%)	6 (2.7%)
Isolated	11 (5.0%)	52 (23.6%)	9 (4.1%)

Table-2 Distribution of mitochondrial dynamics in cells with GFP-tagged tubulin. The distribution of mitochondria across the dynamic categories is listed in stably-transfected cells expressing GFP-tagged tubulin (number of mitochondria, followed by percentage of the total number of mitochondria). The distribution of mitochondria across dynamic categories were similar between wild-type and transfected cells

Likewise, there were no statistically-significant differences when comparing mitochondrial morphology and protein distribution between dynamic categories (**Table 3**).

Parameter	Dynamic Category	Wild type	Transfected	p-value
Area [μm^2]	S	0.84 +/- 0.54	0.56 +/- 0.32	0.014
	D-S	1.23 +/- 1.40	1.07 +/- 1.53	0.244
	D-F	0.48 +/- 0.25	0.34 +/- 0.22	0.148
Tom20 Density [AU]	S	1.10 +/- 0.58	1.04 +/- 0.31	0.564
	D-S	1.09 +/- 0.44	1.06 +/- 0.39	0.473
	D-F	1.37 +/- 0.44	1.09 +/- 0.28	0.062

Table 3 Comparison of mitochondrial morphology and protein distribution in stably transfected cells vs. wild type cells.

This result confirmed that protein over-expression did not alter this particular organelle in these stably-transfected cells at the level of its intracellular dynamics, nanoscale morphology, and nanoscale Tom20 membrane organization.
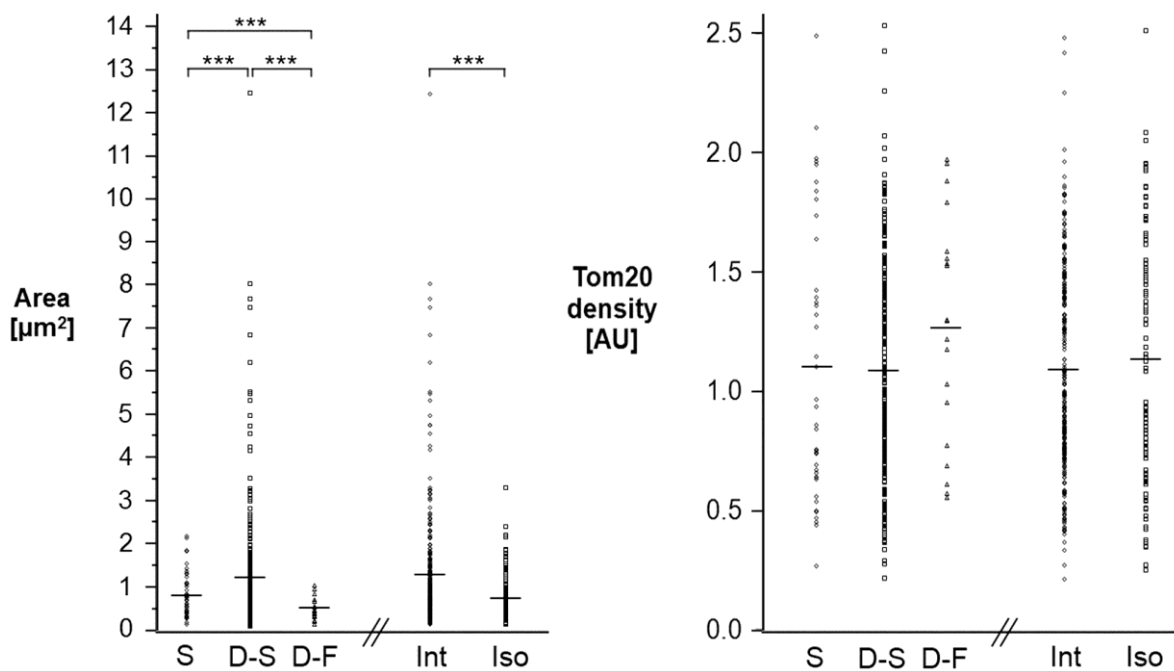

Fig 3.7 Mitochondrial dynamics in relation to size and protein distribution (S, Stationary, D-S, Dynamic-Slow, D-F, Dynamic Fast, Int, Interacting, Iso, Isolated). The average is indicated by a horizontal line. Tom20 density is given as the number of Tom20 localizations per unit area normalized to the overall median density. All dynamic categories were significantly different from each other in area (***, $p < 0.001$), but were not significantly different in Tom20 density.

3.3 Correlative multi-color STORM imaging

3.3.1 Sequential imaging using a virtual grid to repeatedly locate a given region of interest

Sequential or correlative imaging requires that the same region of interest be located on multiple imaging sessions or microscopes. Moreover, carrying out the immunostaining in situ on the microscope stage in between imaging sessions will lead to long periods of "down time" during which the microscope is not acquiring data. As the number of colors to be imaged increases, the time that the sample must remain on the microscope stage also increases, rendering the microscope unusable for other experiments and decreasing efficiency. To limit the microscope down time and to increase the flexibility and ease of imaging, we developed a simple and versatile approach we termed "virtual grid" to repeatedly and reliably locate the same region of interest on different imaging sessions and even on different microscopes. The use of high magnification objectives in STORM imaging implies that the field of view being imaged is relatively small (typically 40x40 μm^2 or smaller). Therefore, finding the same region can be highly challenging once the sample is removed from the microscope. In correlative microscopy, a "finder grid" is used for this purpose (Mao, Yang and Cremer, 2002). However, glass-bottom chambers that are readily

available and used by most laboratories for fluorescence microscopy applications typically do not include a finder grid. It would be beneficial to most people working with fluorescence microscopy to have a simple method for finding the same region of interest on multiple days and even multiple microscopes without the need for a physical grid. Here, we demonstrate a ''virtual grid'' which functions like a grid but without the need for a physical grid (**Fig 3.8a**). The virtual grid can be implemented using a precision motorized stage with a readout for the stage coordinates in the X and Y directions. During the first imaging session, the coordinates were recorded on the region that was imaged, C, along with the coordinates of two reference points, which were defined as the two corner points of the sample chamber, P1 and P2 (**Fig 3.8a** and **Fig 3.8b**). At the start of the next imaging session, the two reference points were relocated and the coordinates of these two points were recorded as P1' and P2'. These reference points were used to locate the cell. The rotation angle between day 1 and day 2 was calculated as:

$$\Delta\theta = \cos^{-1}\left(\frac{\overrightarrow{P_1 P_2} \cdot \overrightarrow{P_1 P_2'}}{\|P_1 P_2\| \, \|P_1 P_2'\|} \right).$$

With careful mounting of the sample, we could maintain $\Delta\theta$ below 0.05 degrees. The new location of the region, C', relative to the corner point P1' was calculated as:

$$C' = \left\| \overrightarrow{P_1 C} \right\| \angle (\theta + \Delta\theta), \text{ where } \theta = \tan^{-1}\left(\frac{\overrightarrow{P_1 C}|_y}{\overrightarrow{P_1 C}|_x} \right).$$

This procedure allowed us to locate the same region of interest within 5 μm (one field of view is approximately 40x40 μm in our microscope, and the precision of our motorized stage is around 2 μm). To locate the region more precisely, images of fiduciary markers (fluorescent beads) were acquired and compared to images of these same markers from the first imaging session. This enabled us to fine-tune the position of the stage (**Fig 3.7c**).
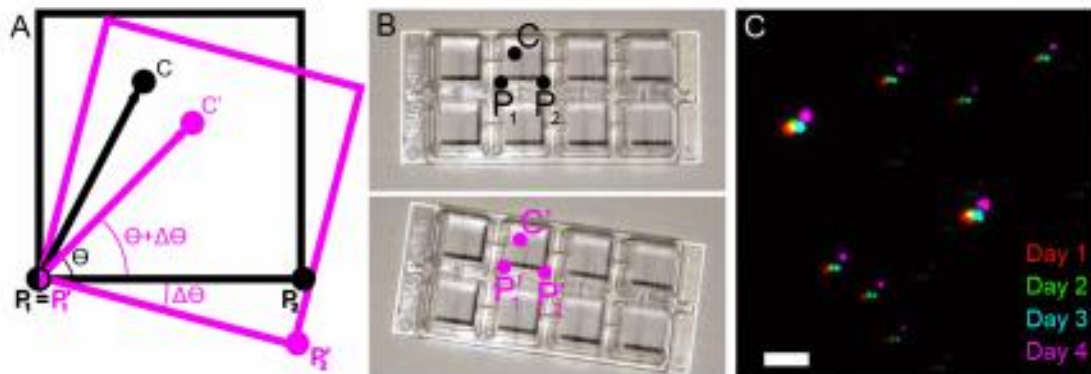
Figure 3.8 Virtual grid to relocate the same region of interest (A-B) During the first imaging session, the coordinates of two references points and recorded (P$_1$ and P$_2$, typically the corner coordinates of the sample chamber as shown in B) as well as the coordinates of the region of interest, C. During the subsequent imaging sessions, the new coordinates of the reference points are recorded (P$_1$' and P$_2$') and these coordinates along with the previously recorded coordinates of the reference points and region of interest are used to calculate the new coordinates of the region of interest (C'). (C) Fiduciary markers (fluorescent beads) imaged on four subsequent days using the « virtual grid » approach to locate them. Scale bar 5μm.

3.3.2 A new multicolor approach

Here, we show that some of the caveats such as cross talk, imaging buffer optimization (see chapter 2) can be overcome with a multi-color STORM imaging approach that uses the same fluorophore for all the colors. This approach is based on sequential labeling and STORM imaging and utilizes a simple and versatile strategy that enables the same region to be located for different imaging sessions and even for different microscopes. Sequential labeling has previously been shown to be useful at the conventional fluorescence level for imaging several different protein species (Weibel and Whitesides, 2006). At the STORM level, this approach enables us to always use the best imaging buffer conditions and the best performing fluorophore for STORM, without any cross-talk or need to consider chromatic aberrations

3.3.3.Multi-color using the same fluorophore

To demonstrate multi-color STORM imaging using the same fluorophore, we labelled the first target structures of interest (microtubules in **Fig 3.9a**, green, and mitochondrial inner membrane in **Fig 3.9b**, green) with appropriate primary antibodies (anti-α-tubulin for microtubules and anti-ATP-synthase for mitochondrial inner membrane) followed by secondary antibody conjugated with a STORM compatible fluorophore pair (AlexaFluor405-AlexaFluor647). After recording a STORM image, the coordinates of two reference points (usually two corners of the 8 well chambers) were recorded and the sample was removed from the microscope stage. The remaining (unbleached) fluorophores were quenched by adding a reducing agent (sodium borohydride, see **Appendix**) and a second target structure (mitochondria outer membrane in both **Fig 3.9a** and **Fig 3.9b**, magenta) was labelled with an appropriate primary antibody (anti-Tom20) derived from a species different from the previously used primary antibody. The secondary antibody, once again, was conjugated with the same fluorophore pair. The two references points were found back, and their coordinates were recorded. The same region of interest was then located using the virtual grid approach described above and a new STORM image was recorded. During the first imaging session, we set the focal plane such that both the sample and the fiduciary markers (fluorescent beads) were in focus at the same time. During subsequent imaging sessions, we manually adjusted the focus such that the fiduciary markers were at the same focus. Finally, after image acquisition, the images of fiduciary markers were used to precisely align the

images (**Appendix**). This sequential labeling and imaging scheme could be repeated as many times as desired to increase the number of colors (see **Fig 3.9c** for a 3-color combination).
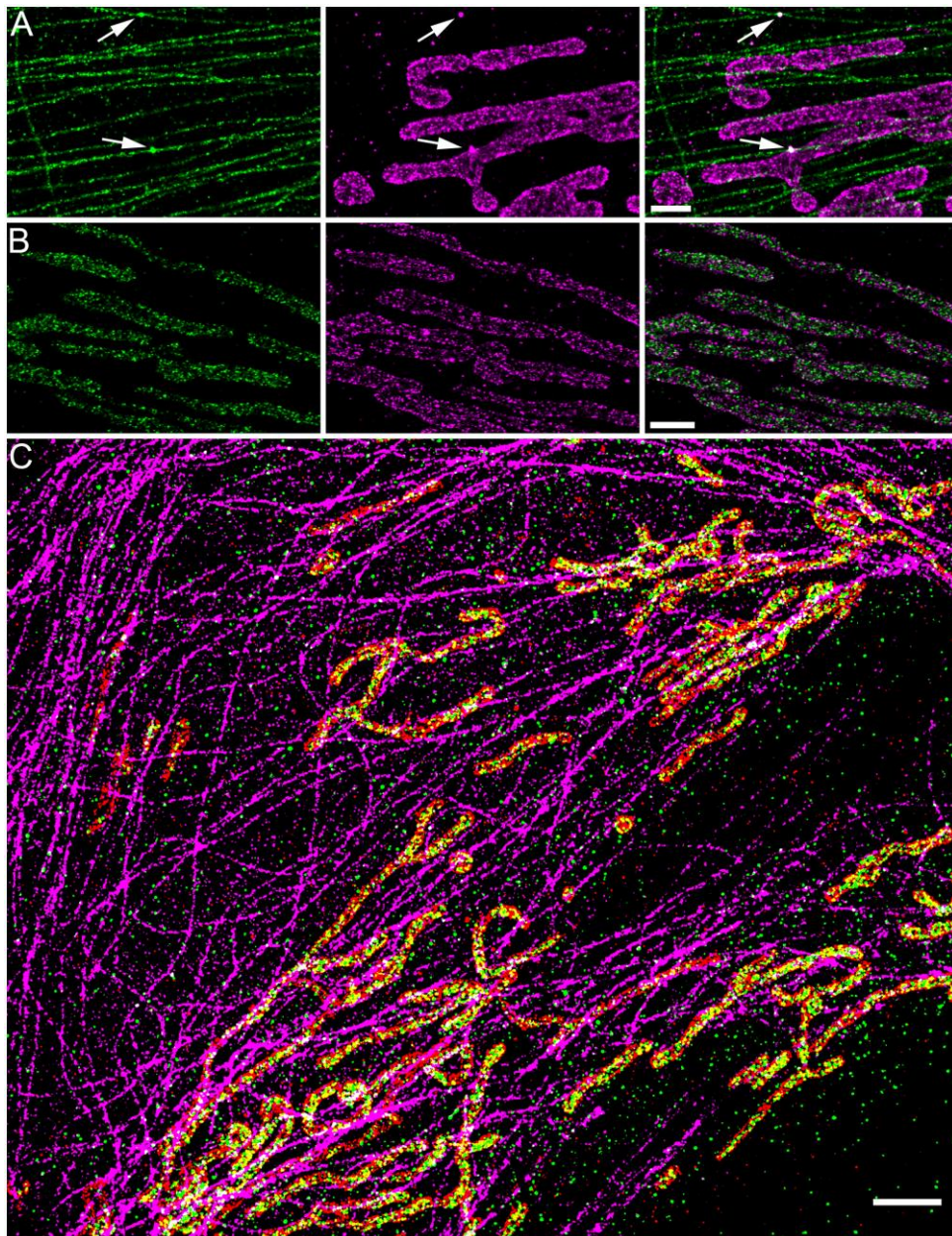
Figure 3.10 Multi-color STORM imaging using a single fluorophore. (A) Microtubules (green) and mitochondrial outer membrane protein Tom20 (Magenta) imaged sequentially using the same fluorophore activator-reporter pair (AlexaFluor405-AlexaFluor647). Arrows show the localized positions of fiduciary markers (fluorescent beads) that were used for image alignment. (B) Mitochondrial outer membrane protein Tom20 (magenta) and inner membrane protein ATP Synthase (green). (C) Three-color image of microtubules (green), mitochondrial outer membrane outer protein Tom20 (magenta) and mitochondrial inner membrane (ATP-synthase, orange) imaged sequentially using the same fluorophore activator-reporter pair (AlexaFluor405-AlexaFluor647).The discontinuous appearance of microtubules is due to the fact that we used anti-GFP antibody to label the GFP-α-tubulin and the endogenous α-tubulin.

 is unlabeled in this scheme. The anti-GFP antibody was used since it offers a different antibody species to those used for ATP-synthase and Tom20. Scale bars, 1 μm (A-B), and 2 μm (C)

The image registration precision was quantified by determining the average distance between the transformed centroid positions of fiduciary markers in one image with the centroid positions of these in the other image (**Appendix**, Equation 1). While we normally use the positions of all the fiduciary markers to calculate the transformation function, optimal registration could be achieved with a minimum of three fiduciary markers for a first order polynomial affine transformation and six fiduciary markers for a second order polynomial local weighted mean transformation, as long as the fiduciary markers chosen for the registration were located on opposite corners of the field of view (**Appendix**). We therefore computed the registration error using this minimum number of fiduciary markers. The average registration error was 12.2±3.0 and 10.5±2.5 nm (mean ± standard deviation, n = 9) (**Fig 3.10**) for the affine and local weighted mean transformations, respectively.
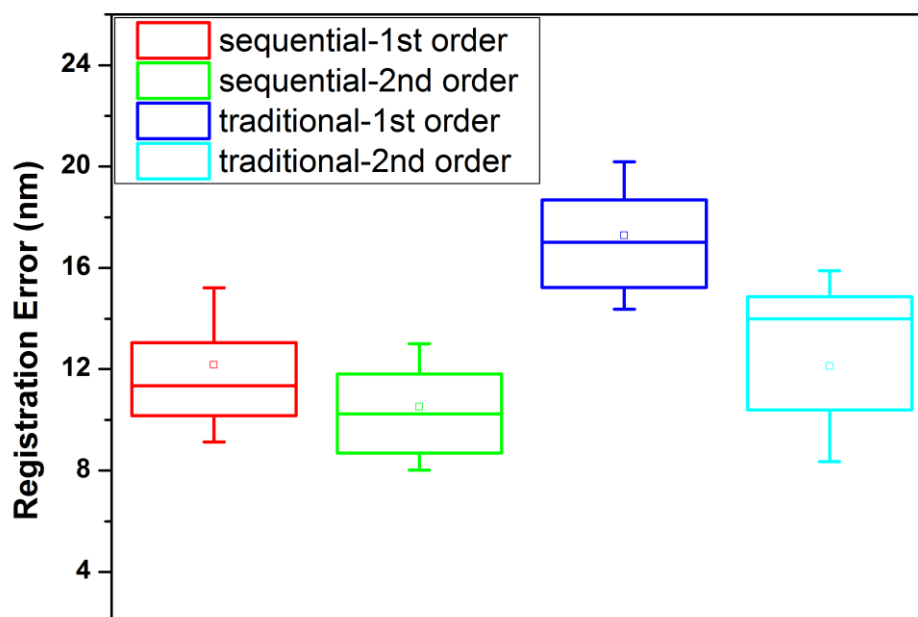
Fig 3.10 Determination of registration error. Registration error, calculated as the average distance between the transformed centroid positions of fiduciary markers from one image with the centroid positions from the other image. Two registration algorithms (first order polynomial affine and second order polynomial local weighted mean) were compared between sequential labeling (sequential) and traditional multi-color imaging using spectrally separated color channels (traditional). The boxes represent the 25th and 75th percentiles, the squares represent the mean, the lines represent the median and the whiskers represent the standard deviation.

The registration error between different combinations of multiple sequential images did not change when the same sample was repositioned many times (**Table 4**).

	Image 2	Image 3	Image 4
Image 1 (reference)	10.0 nm	10.9 nm	9.5 nm
Image 2		10.7 nm	9.8 nm
Image 3			5.6 nm

Table 4 Registration error for multiple sequential imaging of the same field of view. The sample was repositioned and the same field of view was imaged multiple times. The first image (Image 1) was used as a reference image and all subsequent images (Image 2- Image 4) were registered to this reference by using a first order polynomial affine transformation. Registration error was computed as the average distance between the centroid positions of fiduciary markers in different combinations of two sets of images (Image 1-Image 2, Image 1-Image3, Image 1-Image 4, Image 2-Image 3, Image 2-Image 4 and Image 3-Image 4). The registration error was not affected by the multiple repositioning of the same sample

In the case of images acquired in two separate channels (therefore containing chromatic aberrations), the registration error was 17.3±2.9 and 12.1±3.8 nm (n = 9) for affine and local weighted mean transformations, respectively. Therefore, while the chromatic aberrations can be accounted for with fiduciary markers, the registration error is more dependent on the complexity of the registration algorithm in the case when chromatic aberrations are present. The efficiency by which the fluorophores were quenched after the first imaging round was quantified by drawing regions of interest around the structure imaged in the first round and determining the number of localizations per unit area within these regions of interest in the first as well as the sequential image. For a microtubule sample that was labeled at high density (1:70 dilution of primary antibody, typically used in STORM imaging) and imaged in the first round, followed by labeling and imaging of mitochondria in the second round, the microtubule localization density was 20177±8200 μm^{-2} (mean ± standard deviation, n = 4 cells) in the first image. This density dropped to 590±286 μm^{-2} when considering the same regions in the subsequent image, which was comparable to the background localization density (490±234 μm^{-2}) of regions that excluded both microtubule and mitochondria structures. As a comparison, for a two-color image of microtubules and mitochondria recorded using activator-reporter pairs undergoing the same labeling and sample preparation conditions, the localization density of the microtubules was 3777±2394 μm^{-2} (n = 2 cells) in the microtubule channel. This density was lower than the density measured for sequential imaging because only the frames immediately after the activation frame were included in the analysis to minimize color cross-talk. This restriction resulted in a reduction in the number of frames analyzed. In this case, the localization density of these same regions in the mitochondria channel was 2191±2027 μm^{-2}, which was higher than the background density of regions excluding both microtubules and mitochondria (287±337 μm^{-2}), indicating a large degree of crosstalk. Therefore, our method not only eliminates cross-talk, but it also improves the efficiency of accumulating localizations in each channel by not

having to discard frames to minimize crosstalk. Finally, to verify that the additional immunostaining steps performed between imaging sessions did not affect the integrity of the sample, we investigated the effect of repeated sample preparation steps on the structure of microtubules. Sequential images of the same microtubule network imaged before and after five rounds of immunostaining steps aligned within the previously calculated registration error and no structural defects or changes to the microtubule architecture were visible. The beads that were used for the registration also aligned within the previously determined registration error, indicating that the beads did not shift their position during the sample preparation. This result shows that both the sample and the fiduciary markers used for precise alignment were not affected by additional rounds of immunostaining when compared to our calculated registration error.

3.3.4 Multi-color STORM imaging using overlapping antibody species

Using our approach, multi-color STORM imaging should only be limited by the availability of well-performing primary antibodies derived from different species. However, sometimes the best-performing and most specific antibodies are monoclonal antibodies derived from the same species (e.g. mouse) and it may become difficult to avoid using two antibodies derived from the same species. In this case, one approach for multi-color imaging would be to directly label the primary antibody with STORM compatible fluorophores followed by the sequential imaging approach as described above. However, fluorophore labeling of primary antibodies leads to a decrease in antibody concentration, and a decreased labeling density due to a lack of amplification from secondary antibodies. Optimization of primary antibody labeling can be very costly. Moreover, the common presence of other proteins inside the primary antibody buffer solution (such as BSA or ascites), which would also get labeled alongside the antibody, hinders the determination of the labeling efficiency and can lead to non-specific background in the images. To alleviate these problems and to potentially increase the number of colors that can be imaged in one sample, we borrowed an approach used in Electron Microscopy (EM) in which the images are grayscale but can be segmented into different colors due to the high spatial resolution offered by EM (Shroff *et al.*, 2008). We demonstrate that multiple targets can be imaged using the same antibody species and that colors can be segmented based on the spatial separation of the different targets in the high resolution image in combination with the molecular specificity afforded by fluorescence microscopy. To demonstrate this point, as an example, we first recorded an image of ATP-synthase (localized to mitochondria) and LAMP2 (localized to lysosomes), both labelled using a mouse monoclonal primary and anti-mouse secondary antibody and imaged at the same time (**Fig 3.11a**). The high resolution of the final image led to spatial separation between mitochondria-like and lysosome-like structures. However, in some cases, the identity of a structure can be unclear simply from visual inspection. To guide the segmentation, a second target known to localize to one of the structures can be imaged in a sequential session, contributing to an additional color. Here we imaged Tom20, a mitochondrial outer membrane protein (**Fig 3.11b**). Since Tom20 and ATP-synthase partially

colocalize on mitochondria, (**Fig 3.11a** and b arrows) the colocalization could be used to separate the initial image into separate colors. ATP-synthase was identified as those molecules which partially colocalize with Tom20 in a semi-automated way using a custom written colocalization analysis software (see **Appendix**) for the initial segmentation followed by visual inspection for confirmation and manual correction. Similarly, lysosomes were identified as those molecules which did not colocalize with Tom20. Therefore, all three structures could be segmented into three different colors (**Fig 3.11c**). We similarly extended this approach to five-color imaging using three mouse antibodies and two additional antibodies from different species (**Fig 3.11d**).
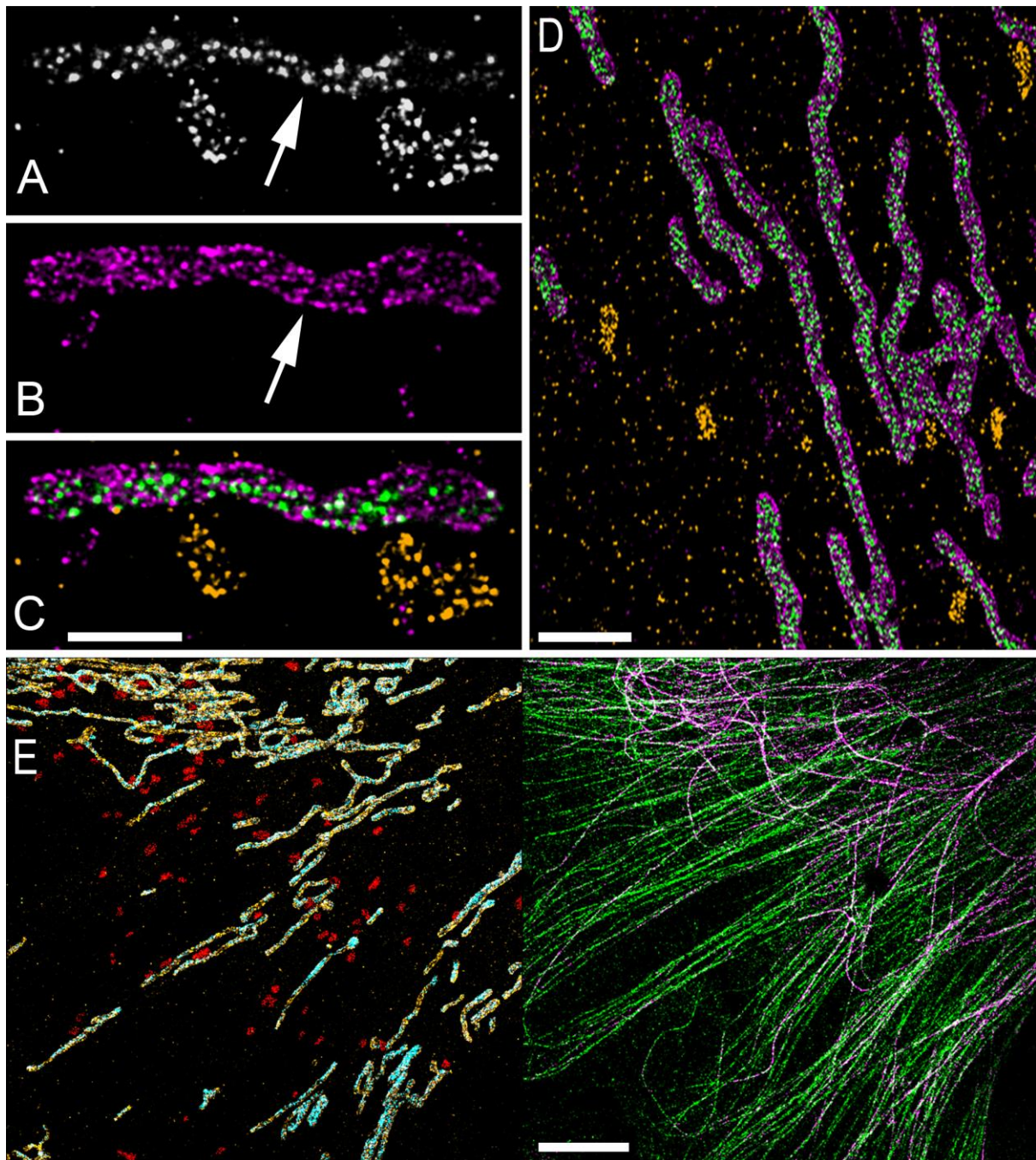
Figure 3.11 Multi-color STORM imaging using overlapping antibody species. (A) An image of ATP-synthase (localized to mitochondria) and LAMP2 (localized to lysosomes) both labeled using a mouse monoclonal primary and anti-mouse secondary antibody and imaged at the same time. (B) An image of Tom20, a mitochondrial outer membrane protein. Since Tom20 and ATP-synthase co-localize on mitochondria (arrows), the colocalization can be used to separate the initial image into separate colors. (C) ATP-synthase is identified as those molecules which colocalize with Tom20. Lysosomes are identified as those molecules which do not colocalize with tom20. (D) A zoom-pit of the three color Tom20 (magenta), ATP-synthase (green), lysosome (orange) STORM image. (E) A five-color STORM image of mitochondrial outer membrane protein Tom20 (orange), mitochondrial inner membrane ATP-synthase (cyan), lysosomal protein LAMP2 (red), total tubulin (green) and acetylated tubulin (magenta). The five-color image is split between the two panels to more clearly display the different structures. The acetylated tubulin, ATP-synthase, and LAMP2 are all imaged using mouse primary antibodies. The acetylated tubulin colocalizes with total tubulin and ATP-synthase colocalizes with Tom20 ; LAMP2 does not colocalize with either total tubulin nor Tom20. Scale bars, 500 nm (C), 2 μm (D) and 5 μm (E).

Summary

We demonstrate multi-color STORM imaging using a single fluorophore pair. Our simple strategy eliminates a large number of technical problems and enables cross-talk free, multi-color STORM with the best performing fluorophore pair. We also demonstrate how the same region of interest can be repeatedly and robustly located on different days or microscopes using a very simple approach of imaging reference points on the sample chamber (such as the corners). This capability is very important since it means that the sample can be removed from the microscope to carry out the sequential labelling steps off-stage. Off-stage labelling means that each target can be immunostained with its own optimal set of conditions (e.g. incubation times and temperatures). More importantly, the microscope is not tied up during the multiple immunostaining steps. This simple method for locating a given region of interest without the need for any special grid can be broadly applied to any situation where sequential imaging is needed, including correlative microscopy where different microscopy modalities are combined.

Chapter 4

Super-resolution imaging reveals differential clustering of microtubule motors on vesicle membranes

Motor proteins play an essential role in cellular organization by carrying organelles along microtubules and delivering them at the right place. Recently, the clustering of dynein motors has emerged as a novel mechanism of regulating retrograde trafficking of large vesicles. We aimed to determine whether similar clustering mechanisms of retrograde and anterograde motor proteins play a role in the trafficking of small vesicles in intact cells. Using multicolor, 3D super-resolution microscopy and quantitative analysis, we revealed the organization of dynein, KIF5 and KIF3 on the membrane of lysosomes at the nanoscale level. Our results show that motor proteins are organized at two different levels on the vesicle membrane. First, motors organize in small clusters consisting of 1-4 motor proteins. Second, in the case of certain motors like dynein and KIF3, these small clusters of motors further organize onto a small patch of the vesicle membrane. In addition, the total number of motor teams on the membrane is differentially regulated for the three motors and scales differentially with the size of the lysosome among the different motors. Overall, our results reveal for the first time how various motor proteins are organized on the membrane of small vesicles in intact cells, giving new insights into mechanisms of transport regulation by motor protein clustering[4].

Introduction

Dynein and kinesin are the two main microtubule-based motor proteins, which are essential for cell homeostasis. They are responsible for a huge number of tasks, ranging from cargoes transport to centrosome repositioning. A functional failure could lead cell apoptosis, which can then be related to neurological disorders. Discovered in the 60's and 80's respectively, dynein and kinesin have then been broadly studied *in vitro*. Previous works have shown that dynein is a weaker force generator as compared to kinesin and it is more prone detachment. Therefore, it has been proposed that multiple dyneins are required to effectively balance a few kinesins, and in-vitro experiments have indeed demonstrated this (A. Yildiz *et al.*, 2004; Carter and Cross, 2005; Hendricks, Holzbaur and Goldman, 2012). Indeed, kinesins have a higher rate of attachment, detachment and reattachment to the microtubule filament than dyneins. These differences also reflect the underlying biophysical properties of these motors: multiple kinesins do not work especially well together, while the clustering of dyneins into teams greatly enhances force generation and motility (Hendricks *et al.*, 2012; Arpan K Rai *et al.*, 2013). It has been roughly estimated to be 1 to 4 kinesins and 1 to 9 dyneins, using purified vesicles of ~90 nm in diameter (Hendricks *et al.*, 2010) and various methods like single step photobleaching of labeled motors or optical force measurements

In addition to the total number of motors present on the vesicle, their arrangement and location on the vesicle membrane are also highly important in determining whether they can cooperate (Arpan K Rai *et al.*, 2013). In order for multiple motors to engage with a given microtubule, they need to be positioned in close proximity, covering limited area of the vesicle membrane. Coordination by motors in close proximity is important for several reasons: the cargoes can bind faster to microtubules in the case of very large cargoes at high viscosities, clustering also increases the run length before detachment of the cargo from the microtubule (Erickson *et al.*, 2011). The probability that multiple motors randomly locate in a limited area of the vesicle is 50% for a 100nm diameter sphere, but only 4% for a 380 nm sphere (Rai *et al.*, 2016). Hence, for cellular cargoes ranging in size between 100-500 nm, additional mechanisms may regulate motor organization on the cargo membrane.

Immuno-electron microscopy studies have reported a clustered distribution of certain motors typically ranging in number between one and seven (Marples *et al.*, 1998; Habermann *et al.*, 2001; Gross *et al.*, 2007). Optical trapping experiments on beads confirm this range by measuring forces of 7 pN, corresponding to 7 budding yeast dyneins (Rai *et al.*, 2016). Furthermore, the organization is likely a dynamic process. It has been shown that during autophagosome maturation dynein distribution changes from uniform to clustered (Rai *et al.*, 2016). This clustering is mediated by the changes in lipid composition and an increase in cholesterol content. However, due to limitations of previous methods (low throughput and efficiency of immuno-EM, low spatial resolution of light microscopy), whether multiple different motors indeed cluster on the membrane of physiological cargoes

like lysosomes is an open question. In this chapter, we developed new multi-color super-resolution imaging methods and use them to address this important question.

4.1 Experimental workflow

Our first approach to study how KIF5, KIF3 and dynein are organized on the vesicle membrane was to perform conventional fluorescence microscopy. Conventional microscopy methods such as confocal do not have sufficient spatial resolution to reveal the distribution of motors on the lysosome membrane since both lysosomes and motors are below the diffraction limit. Indeed, in confocal images, the motor proteins seemed to completely cover the lysosome membrane (**Fig 4.1**).To overcome this problem we decided to use 3D, cross-talk free multi-color STORM imaging (**Fig 4.1**) developed previously in our laboratory (see Chapter 3 and the article (Tam *et al.*, 2014)). We took advantage of a stable cell line expressing lysosomal protein LAMP2 fused to mCherry. To visualize lysosomes with high resolution, we labeled the mCherry using and a chicken anti-mCherry antibody and A405-A647 labeled secondary antibody against chicken. After STORM imaging, the remaining fluorescence was quenched chemically as described in Chapter 3 on the microscope stage. Next, one of the three motor proteins (KIF5, KIF3 or dynein) was labeled using a mouse primary antibody followed by incubation of A405-A647 labeled secondary antibodies against mouse and finally imaged with STORM. STORM image of fiducial markers consisting of fluorescent beads were used to precisely align the two STORM images based on a 2D local weighted mean algorithm (see **Chapter 3**). On the final STORM image we could start to identify small clusters of motors overlapping with the images of lysosomes. More specifically, we could appreciate motor puncta on different places on the lysosome membrane (**Fig 4.1 C-E**)
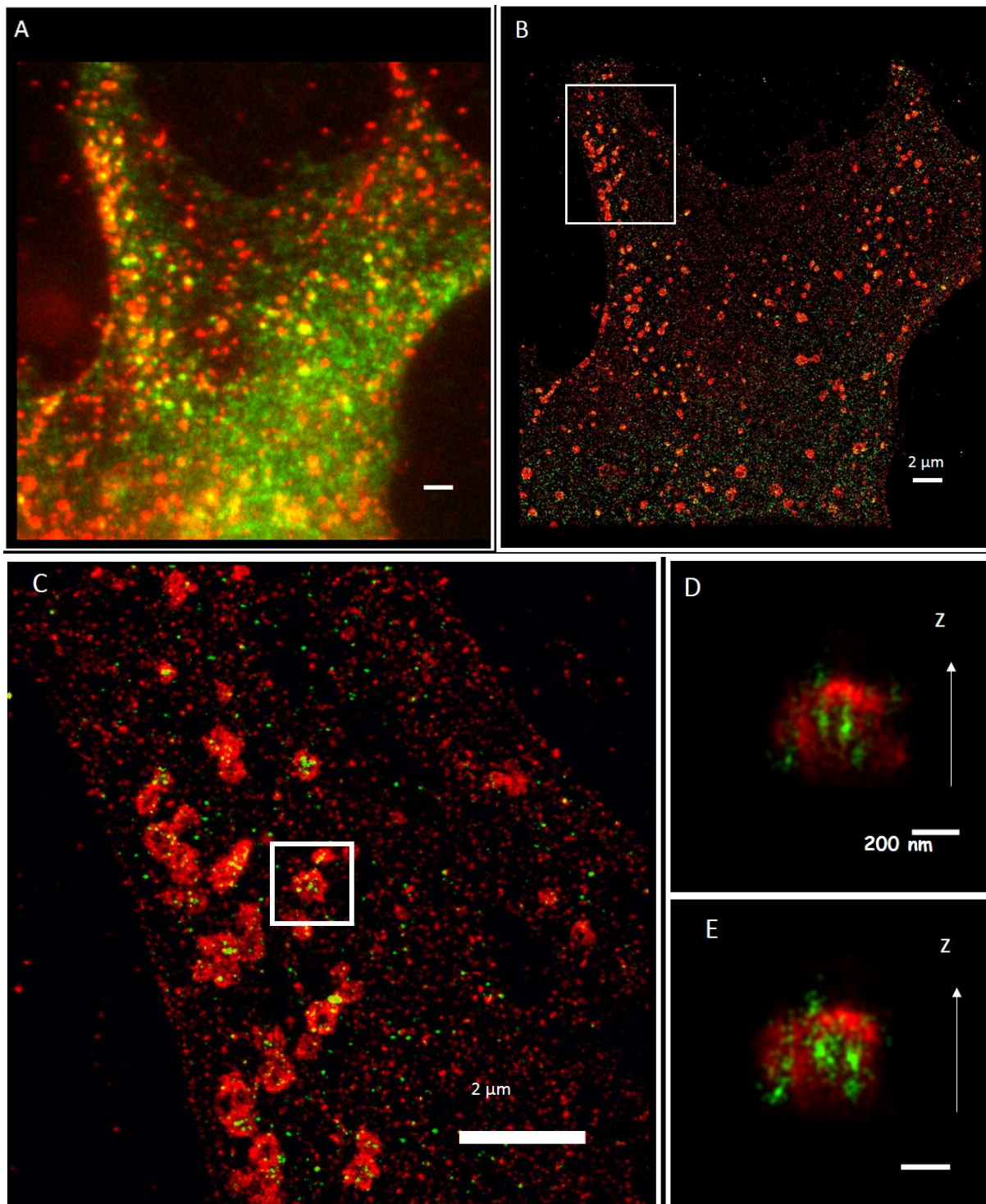
Fig 4.1. The power of 3D sequential STORM. (A) the conventional diffraction limited image does not have enough resolution power to discern the KIF3 motor (green) and precise position on the lysosome (red). (B) The same region of the sample was recorded with STORM using the grid technique developed previously in our laboratory (see chapter 3). (C) Zoom shows the puncta of KIF3 overlap with lysosomes. (D-E) Different 3D views of the same lysosome selected in the white frame in C, with the motor protein.

4.2 Analysis Workflow

Previous to any analysis, we precisely overlapped both STORM images relying on a 2D local weighted mean transformation that aligns fiducial markers (beads) spread in the sample . For each image, we used at least 5 beads for the transformation, reaching a residual registration error below 10 nm. For details of the transformation please refer to **Chapter 3,** section 3.2 and A**ppendix**. Finally, the two images are aligned along the z-axis by a simple rigid z-shift. On average, the z-shift applied was below 50 nm since we selected experiments in which the two images maintained their relative z-position roughly constant.

After the alignment of the two STORM images, regions of interest corresponding to lysosome images were manually selected using ImageJ and retained for further analysis (**Fig 4.2-A**). We particularly selected lysosomes that were roughly spherical in shape and contained a minimum localization density of 6000 localizations.μm^{-3} (23 000 localizations .μm^{-3} on average), such that its image could be reliably reconstructed at high resolution. The corresponding region in the STORM image of motors was similarly retained for further analysis.

Once the lysosomes were selected, we fit the 3D localization distribution arising from each lysosome to a sphere in order to model the edges of the lysosomal membrane (**Fig 4.2-B**). This was important, as the cloud of localizations in the STORM image can be discontinuous with gaps for several reasons such as incomplete labeling or breakage due to fixation. For each lysosome, we calculated a residual error of the fit by computing the distance from each localization to the membrane position obtained from the fit. The average residual error was 37 nm (n=180 lysosomes) and equivalent to our 3D localization precision (36 nm), suggesting that the sphere was a good fit. Since the shape of lysosomes in some cases deviated from a perfect sphere, we also compared the spherical fit to a more complex model of the lysosome shape composed of several polynomials. This polynomial fit gave a similar residual error (35nm, n=180 lysosomes), confirming that the spherical fit was a good approximation. Since the sphere fit was faster, we used this as a method of fitting.

The corresponding region of interest in the motor protein STORM image showed the presence of several clusters. These clusters were projected in 2D and segmented using a 2D cluster identification algorithm that was previously developed in the group (Ricci *et al.*, 2015) . This algorithm grouped together localizations in close proximity into clusters (**Fig 4.2-C**). To further refine the clusters in 3D, we considered the 3D positions of the localizations inside the segmented clusters. The localizations that were outliers in the z-dimension within the segmented clusters were removed. To remove outlier localization in z, we set a density threshold of 3 localizations per 15 nm. This density threshold removed isolated localizations that were far away from the core of the cluster. Finally, we fit the z-position of the localizations to multi peak Gaussian and determined whether they were indeed an individual cluster (best fit to a single Gaussian) or multiple clusters overlapping in z (best fit

to two or more Gaussians). This analysis provided the center position of each cluster, the size of each cluster and the number of localizations within each cluster (**Fig 4.2-D**).

After the cluster analysis and the spherical fit, we had information on the X,Y and Z coordinate of the membrane as well as the X,Y, Z center position of the motor clusters. Thus we could calculate the perpendicular distance of the motor protein clusters in the STORM image from the lysosome membrane. We set a threshold of 50 nm to consider the motor protein cluster as belonging to the lysosome. This threshold was based on our 3D spatial resolution (roughly 40 nm), the rough size of the antibody complex (10-15 nm) and the estimated distance between the labeled motor subunit and the membrane (an unfolded motor can span between 60 to 80 nm in size). We observe a steady and high concentration of motors up to 50 nm and then a very irregular concentration and sparse distribution. After this threshold 49% of motor clusters were removed as not belonging to the lysosome membrane. Finally, the remaining motor protein clusters were projected onto the 3D membrane obtained after the spherical fit (**Fig 4.2 E**).
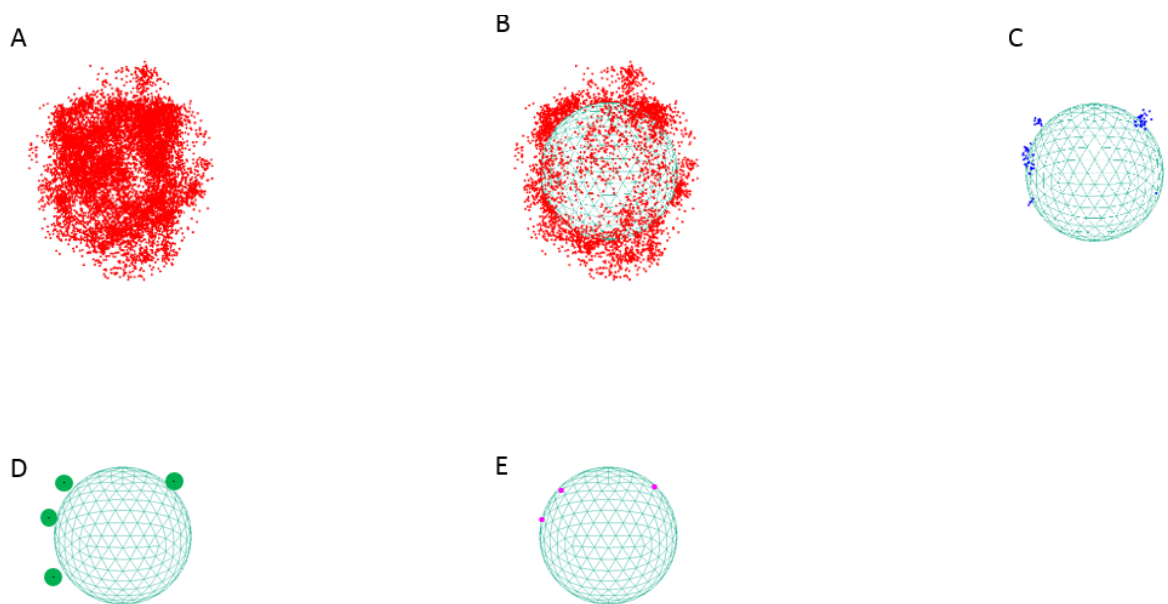
Fig 4.2. General workflow. (A) After two sequential STORM acquisitions, and precise alignment, the lysosome images were manually segmented. (B) The lysosome localizations were fit to a sphere. (C) The motor clusters were segmented using cluster identification algorithm. (D) The cluster centers were identified. (E) Clusters not associated to lysosome were filtered out and the remaining clusters were projected on the lysosome membrane.

This workflow was semi-automated, and result in a day of experiment followed by a day of analysis. In each experiment, at least 10 lysosomes were selected. The lysosomes spanned a size range of 220 to 650 nm. The selected lysosomes were mostly in the cell periphery since this was the region of the cell flat enough for proper imaging.

4.3 Results

The motility of lysosomes is regulated by several mechanisms including regulation of motors by scaffolding and adapter proteins, by the local cytoskeleton or through clustering of motors (Fu and Holzbaur, 2014). It has long been thought that the arrangement of motors in small clusters on the vesicle membrane allows them to simultaneously engage with the microtubule and to cooperate. However, determining the organization of motors on the membrane of vesicles in intact cells has been challenging for several reasons. The motors and the vesicles are typically smaller than the diffraction limit and there is a large population of cytoplasmic motors, making it difficult to discern vesicle-bound motors from unbound ones using conventional microscopy methods. Here, we used 3D multi-color super-resolution microscopy to study and visualize the organization of three motor proteins, dynein, Kif5 and Kif3 on the membrane of lysosomal vesicles.

4.3.1 Dynein and KIF5 organization

1. Dynein and KIF5 are organized into few small motor teams on lysosomes

In order to determine the organization of dynein and KIF5 on lysosome membrane, we analyzed several parameters after segmentation of the lysosomes and their associated motor clusters. First, we determined the number of clusters present per lysosome (**Figure 4.3**) and found that in both cases a small average number of clusters is present on lysosomes (Average=2 for dynein and 1.4 for KIF5).
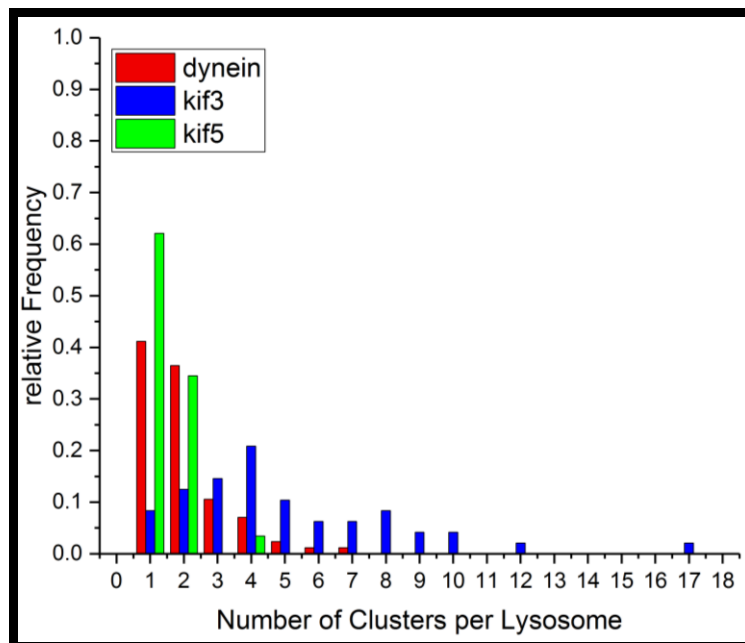
Fig 4.3. Frequency distribution of the number of three different motor proteins cluster per lysosome. The dynein motor proteins (red) are almost equally distributed, between one and two motors per lysosome, the KIF5 motor (green) is mostly found single on the lysosome membrane whereas the KIF3 is more distributed, with a mean of five clusters per lysosome. The lysosome size homogeneously ranged from 200 to 600 nm. A total of 88, 63, 29 lysosome were analyzed for dynein, KIF3 and KIF5 respectively

We further determined the number of localizations per cluster (**Fig 4.4**). This quantity is proportional to the number of motors in the clusters. We first used a log-normal model to fit the number of localization per individual primary/secondary complex (**Fig 4.4 B**) and we got the median number of localization per primary-secondary antibodies complex (13). We could estimate, as a first basic approximation, the number of motors by comparing the range for the number of localizations per motor cluster (~10-80, **Fig 4.4**) to the median number of localizations (13) in isolated primary-secondary antibody complexes. This analysis showed that the clusters were composed of small teams of motors. Depending on the motor protein around 20-40% (data shown for dynein **Fig 4.4 C**) of clusters were in fact single motors with the remaining percentage of clusters ranging between 2-6 motors (**Fig 4.4 A**).
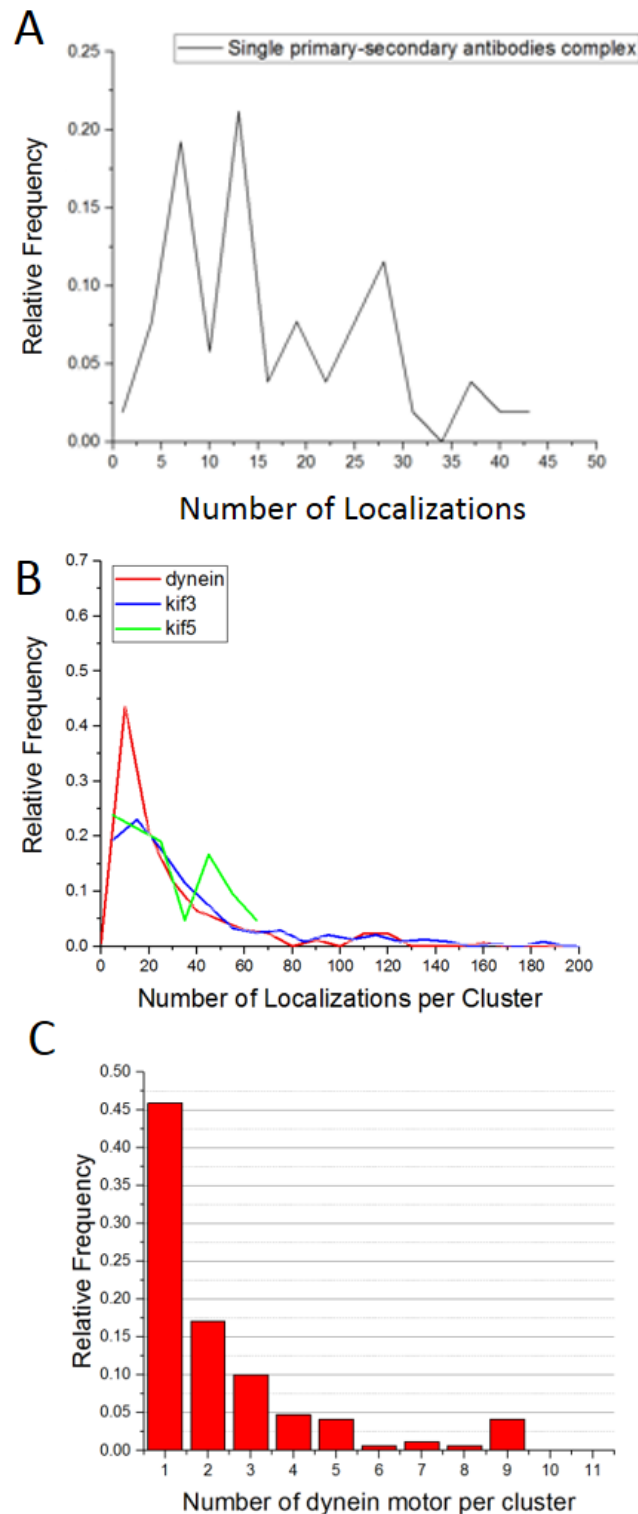
Fig 4.4 Number of motors per cluster.(A) The number of localizations per single primary-secondary-antibodies complex was correlated with (B) the number of localizations per cluster for each motor species. The number of motor per cluster was then deduced as a first approximation (C). The dye pair (A405-A647) was used in each case. The single antibody localizations are collected from the background of the experiment, i.e. under the same illumination conditions.

Finally, we summed up all the localizations in all the dynein or KIF5 clusters present on a given lysosome to determine the total number of dynein or KIF5 motors associated to lysosomes. We found that the histogram for the total number of localizations showed multiple peaks (3 peaks for dynein and 2 peaks for KIF5) (**Fig 4.5 A-C**). Once again based on the comparison to the median number of localizations in primary-secondary antibody complexes, these peaks roughly corresponded to 1, 4 and 9 motors in the case of dynein and 1 and 4 motors in the case of KIF5. These results are in agreement with single step photobleaching results carried out on purified lysosomes for dynein and dynactin (Hendricks *et al.*, 2012) as well as optical trap experiments that show only a small number of engaged Kif5 motors on lipid droplets (Shubeita *et al.*, 2008).

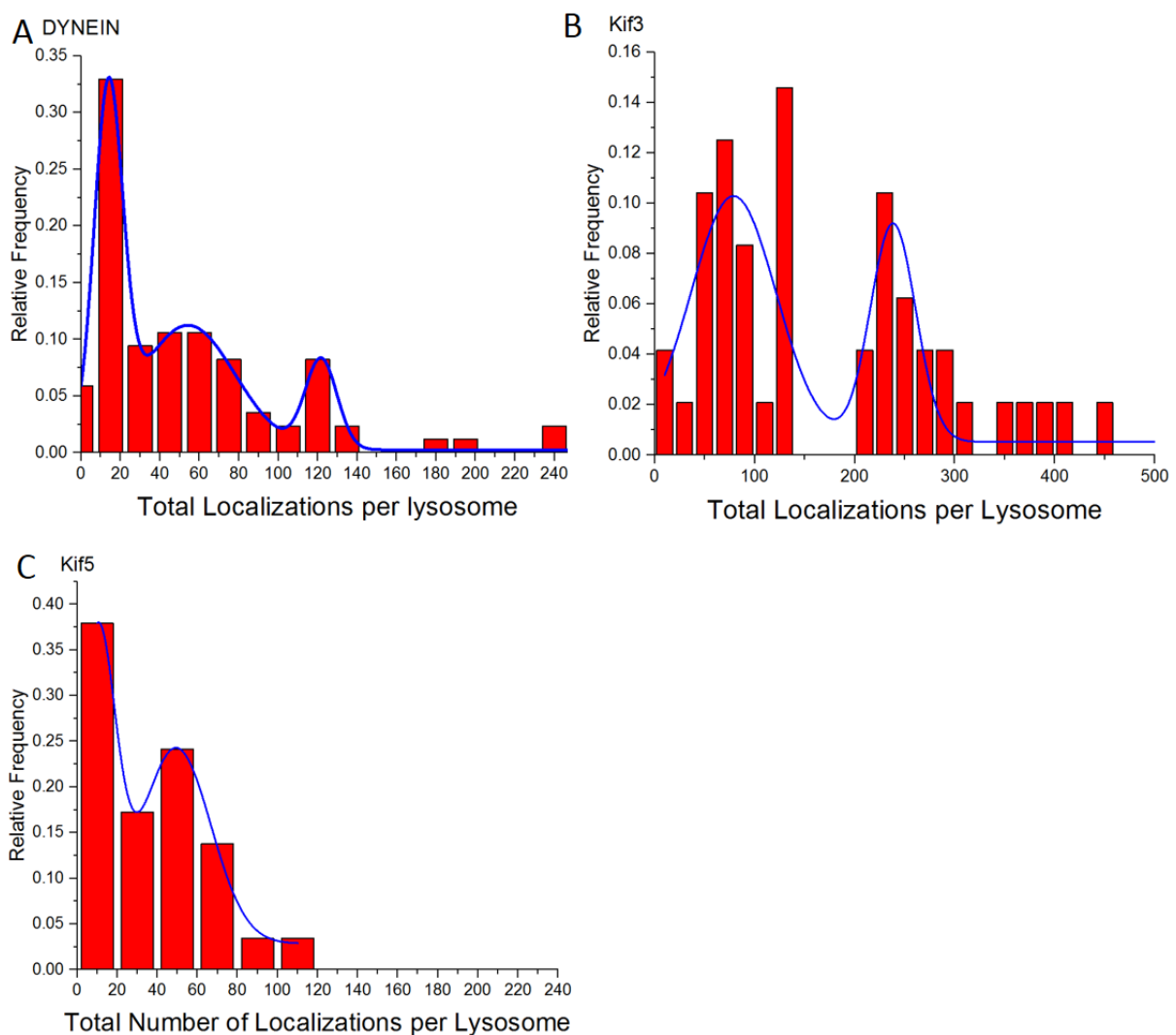**Fig 4.5 Number of motor per lysosome.**(A) Peaks at 13, 54, 122 localizations, corresponding to 1, 4 and 9 dynein motors respectively. (B) Peaks at 67, 132, 238 localizations, corresponding to 4.5, 9 and 16 KIF3A motors on the lysosome.(C) Peaks at 10, 50 localizations, corresponding to 1 and 4 KIF5B motors on lysosome. The total amount of lysosome analyzed was of 88, 63, 29 for dynein, KIF3A and KIF5B motors respectively.

In order to assess the veracity of our finding we submitted the dynein raw data to a recent analysis method based on DNA origami (Zanacchi *et al.*, 2017). Purified single yeast GFP-dyneins from HeLa cells were attached on DNA origami via handles and stained using primary/secondary approach. In order to have a calibration for the quantitative analysis. We imaged single primary-secondary complexes (each complex corresponding to a single protein) under the same condition as the ones used to obtain the STORM images used previously for the dynein data. It was determined that the number of localizations for a single protein followed a log normal distribution. The proportion of monomers, dimers, trimers and so on could therefore be obtained by fitting the number of localizations in the experimental data to a recursive convolution of log normal calibration functions. Since the original calibration experiment was done under different imaging conditions, the data from the dynein experiments carried out in his thesis could not be directly compared to the original calibration. However, we recently developed an approach that can transfer the calibration to the new imaging conditions by convolving with a transfer function (see **Appendix** for the description of the parameters of the log-normal function). Indeed the calibration was made for the DNA origami, based on antibody against GFP, and in our case, the calibration was made based on antibody against dynein. The normal-log distribution approach consist in fitting the distribution of localizations of a primary-secondary antibody complex attached to a single copy of dynein with a log-normal distribution. From a general distribution of number of localizations (coming from an unknown number of dyneins), the number of dynein was estimated by fitting the distribution to a linear combination of the calibration distributions previously obtained from the calibration experiments (**Fig 4.6 B**). The optimal number of log normal function that should be linearly convoluted (i.e, what is the maximum number of dynein), was determined by minimizing the fit objective function (**Fig 4.6 A** and see **Appendix** to know what is an objective function)
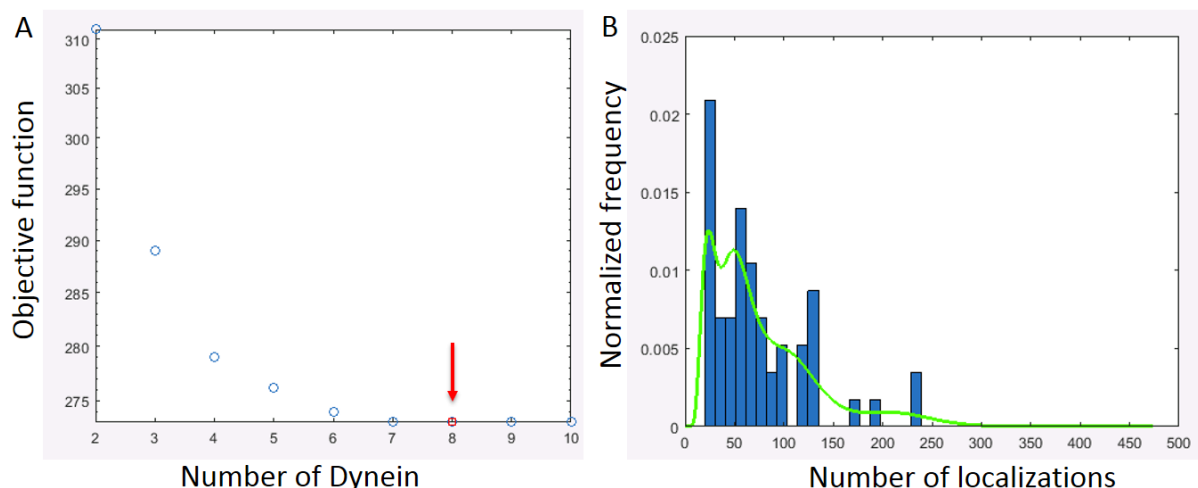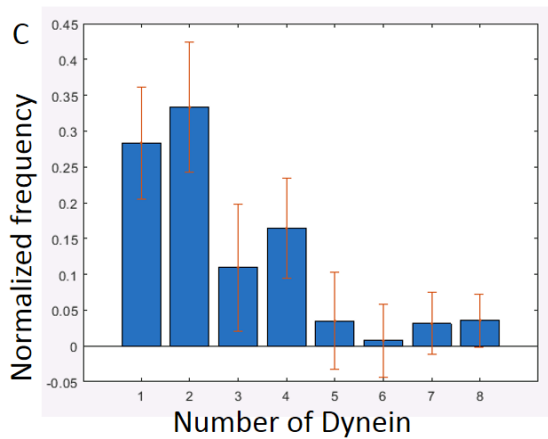
Fig 4.6 Quantification of dynein complexes around the lysosome. (A) The objective function for different stoichiometry with a minimum corresponding to 8 motors (red arrow). (B) Fit to a linear combination of log-normal distribution (green) up to 8 copies of dynein. (C) Percentage of 1, 2 , 3 , 4 , 5 , 6 ,7 and 8 motors obtained from the fit. Error bars refer to the lower bound to the standard errors based on the Fisher Information Matrix.

The results of the analysis using DNA origami as a calibration, for the dynein data, are in agreement with the previous estimation, which makes us more confident about the robustness of the experiments. In addition, the total number of motors on the lysosome ranged from 1-8 (**Fig 4.6 C**). The dynein motors are found to be in 1, 2 and 4 copies mostly per lysosomes.

While we do not have similar calibration data for the kinesin motors (the original DNA origami calibration was done for dynein), if we assume a similar efficiency for the antibody labeling, we can conclude that both Kif5 and Kif3 form similarly small teams as dynein, however overall much less Kif 5 (1-4) and much more Kif 3 (1-16) are present on lysosomes.

2. Dynein and Kif5 organization is largely independent of lysosome size

To determine whether the organization and the number of motors present in the case of dynein and KIF5 depended on the size of the lysosome, we determined the correlation between the previously measured parameters (total number of clusters per lysosome and the total number of motors per lysosome) and the lysosome size measured from the super-resolution experiments. We did not find any strong correlation between the size of the lysosome and the number of dynein or KIF5 clusters per lysosome (**fig 4.7 A, C**). We observed the same lack of correlation between the total number of dynein and KIF5 motors per lysosome (**fig 4.7 D, F**)
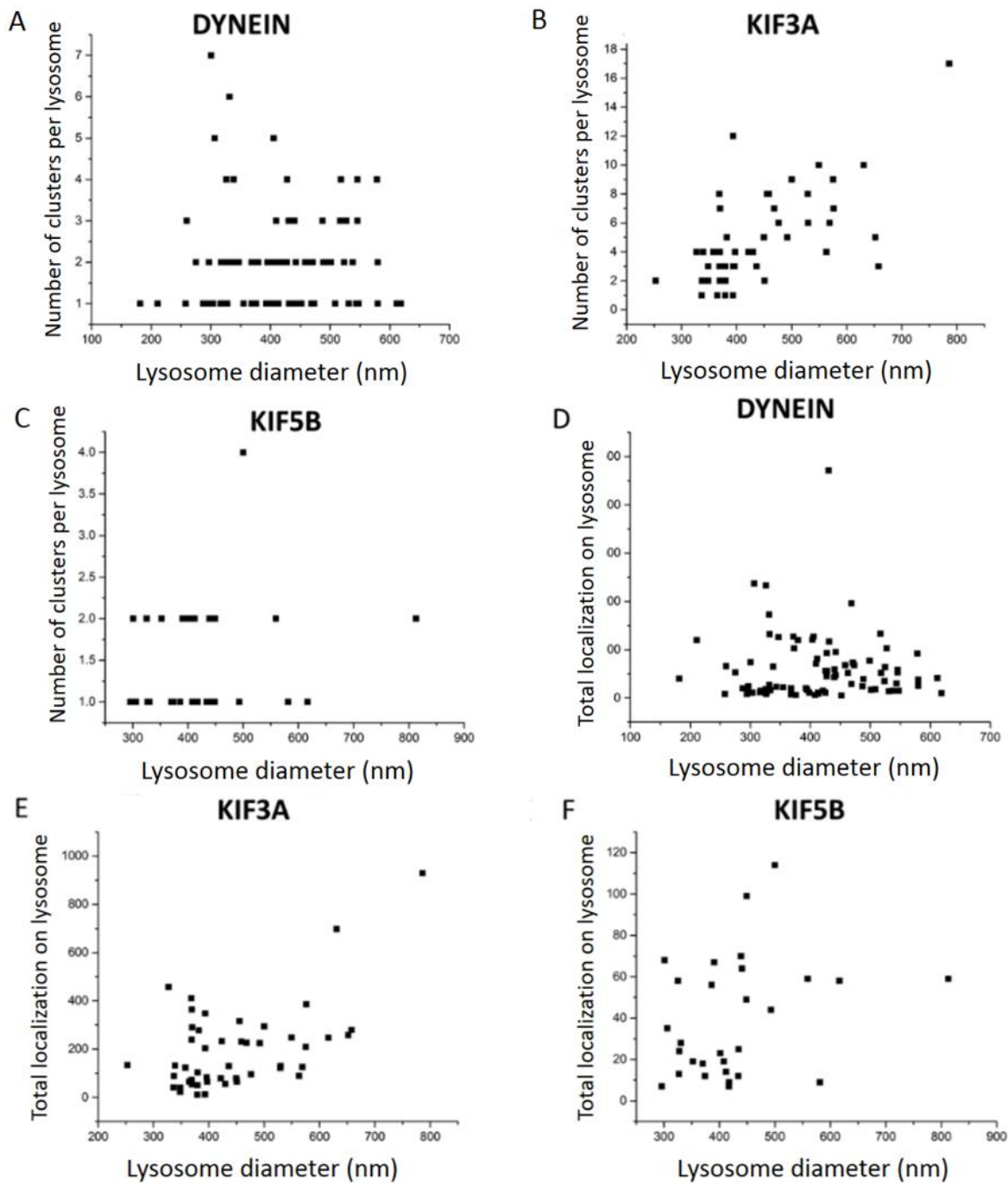
Fig 4.7. Correlation between lysosome diameter and motor protein organization. The Pearson's correlation was used to calculate correlation coefficient. No correlation was found for the number of cluster of KIF5B motors and dynein motors, (A) and (C) respectively, whereas a positive correlation (R=0.6) was found for cluster of KIF3A motors. The total amount of dynein motors is independent from lysosome diameter (D) whereas a weak positive correlation was found between the total number of KIF3A motors and the lysosome size (R=0.4)(E). KIF5B global motors number also show a weak positive correlation (R=0.3) with the lysosome diameter (F).

4.3.2 KIF3 organization

1. Many KIF3 clusters are present on lysosomes

We determined the organization of KIF3 in the same way as described above. Our results showed that in the case of KIF3, in contrast to dynein and KIF5, a much higher number of clusters is present on lysosomes (Average =5 for KIF3). The number of localizations in the clusters were similar to dynein and KIF5, suggesting that KIF3 also clustered into small teams of motors on the lysosome membrane composed of 1-4 motors. The histogram for the total number of localizations showed 2 major peaks (**Figure 4.7-B**), corresponding to roughly 5, and 15 motors. Thus many more KIF3 motors arranged in small teams are present on the lysosome membrane compared to dynein and KIF5.

2. Number of KIF3 motor clusters positively correlates with lysosome size

The total number of KIF3 motor clusters as well as the total KIF3 motors positively correlated with lysosome size (**fig 4.7 B** and **Fig 4.7 E**), although the correlation was stronger for the number of motor clusters. These results suggest that, larger lysosomes require more KIF3 motors working cooperatively for their transport. This correlation between lysosome size and the number of KIF3 motor clusters is consistent with the fact that KIF3 is a weak motor and likely more motors need to cooperate to move a larger cargo through the crowded cytoplasm.
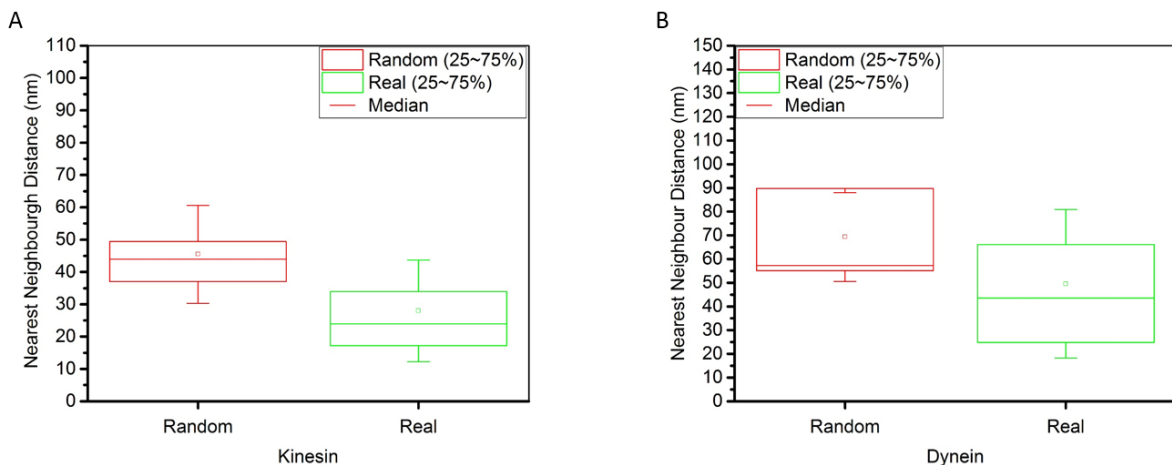
Fig 4.8 3D nearest neighbor distances between real clusters and randomly distributed clusters. We compared the real data to a random distribution. For both dynein (A) and KIF3 (B), we found that motor teams were closer together to each other than what would be expected for a random distribution.

4.3.3 The motor clusters are organized on a small patch of lysosome membrane.

Finally, we wondered whether the small teams of motors themselves were randomly distributed on the lysosome membrane. When a lysosome had 3 or more motor teams, we calculated the 3D nearest neighbor distances between the clusters. In order to calculate

nearest neighbor distance for a random distribution, we randomly generated the same number of points on a sphere of the same size as the lysosome and calculated the 3D nearest neighbor distances of between these random points. We repeated this calculation 1000 times for each lysosome (n=180), each time generating a new set of random points. We then took the average nearest neighbor distance of these 1000 iterations in each of the 180 cases. This analysis showed that for both dynein and KIF3 (motors that had 3 or more clusters present on lysosomes), the actual nearest neighbor distances between the motor clusters was smaller than that expected from the random distribution (**Fig 4.8**). Hence, the motor clusters are not randomly organized on the lysosome membrane but instead they further cluster on a small patch of the lysosome membrane. This nonrandom organization of motor proteins has been recently observed for dynein during the maturation of phagosomes (Rai *et al.*, 2016).

Conclusion

In conclusion, we used super resolution microscopy to reveal two different levels of organization of motor proteins on the lysosome membrane (**Fig 4.9**). The first level of organization was the arrangement of motors into small teams and this organization was independent of the type of motor protein. Many more kinesin 2 teams were present on lysosomes than dynein or kinesin1. This result is consistent with previous work showing that kinesin 2 is a less processive and weaker motor, which likely needs to work in larger teams. The second level of organization was the clustering of the motor teams in small patches of lysosome membrane as their nearest neighbor distances were closer than expected from random distribution. Further, we found that kinesin 2 organization correlated with lysosome size and larger lysosomes contained more kinesin 2 teams, also consistent with the weak nature of this motor.
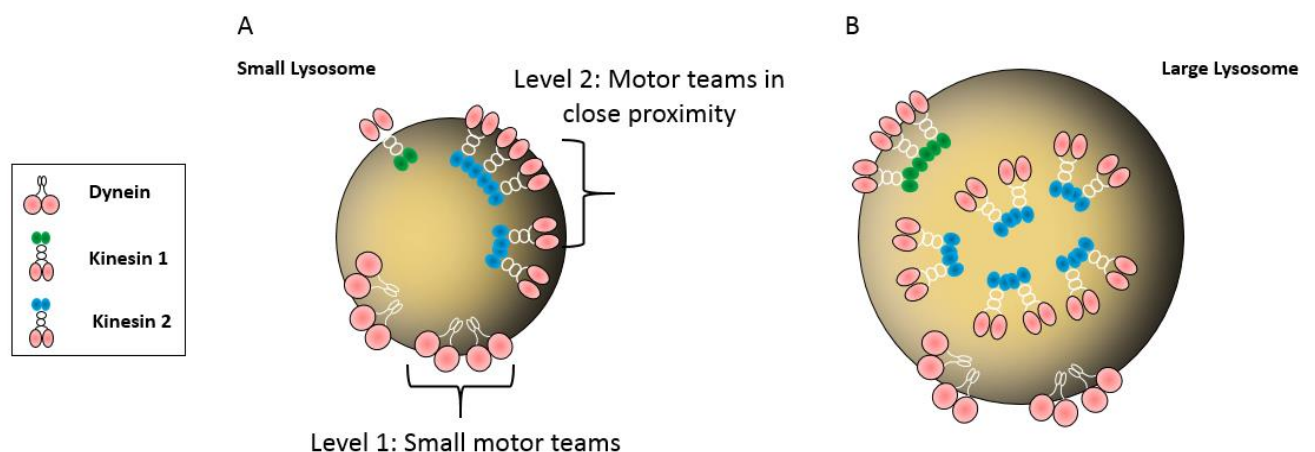
Fig 4.9. Different organization of motor proteins depending on its type and on the size of the lysosome. (A) For small lysosomes, all type of motor proteins (dynein, KIF5 (kinesin-1) and KIF3

(kinesin-2)) studied, are clustering in small teams of motors. A second level of organization is observed : the small teams tend to cluster each other. (B) For large lysosomes, a strong correlation between the number of KIF3 cluster and lysosome size was observed.

We pushed further the possibilities of the super resolution microscopy by creating tools for biologist that can be easily re-used in other biological context. The use of localizations as dots to connect, in order to model a structure, was initially thought for a simple case: the spherical lysosome shape, but its application can be extended to more complex structures such as mitochondrion membrane (using Tom20 for external membrane, or Tim44 for internal membrane). Also the projection of the center of the motor protein cluster on the membrane of lysosome, permitted to get more information on the distribution of the cluster. The geodesic distance were first calculated and compared to a random distribution. Another step could be to compare the distribution to an homogenous distribution, or to calculate the minimal area that encompasses all the cluster projections, and correlate this area with the position of the microtubule filament. Quantification is a feature that seemed inaccessible for STORM due to its stochastic nature but with the advance in the field of cluster analysis, it is now a very relevant technique that can be associated with STORM. The Bayesian approach, the Ripley's K function, the Density-based spatial clustering of applications with noise (DBSCAN), the Voronoi tessellation approach are data clustering algorithm which could be applied to STORM data (Andronov *et al.*, 2016; Griffié *et al.*, 2016) .

Chapter 5

Conclusions and future work

In this last chapter, I will review and discuss the main conclusions reported in this thesis and highlight its novel contribution to science from a technological point of view as well as from a biological perspective. I will further discuss future directions following this work and possible future applications of the 3D crosstalk free multicolor STORM.

Motor proteins such as dynein and kinesin transport vesicles and organelles through the microtubule network to the required location of function. Motor protein organization plays an essential role in achieving efficient intracellular transport. It has been shown by many research groups that several dynein and kinesin motors are present on individual vesicles and these motors may cooperate or compete when moving the vesicle. The way in which multiple motors organize on the vesicle membrane will have important implications for how they can cooperate or engage in a tug of war during transport. For example, if motors are randomly distributed on the membrane, likely just one motor can engage with the microtubule at any given time, whereas if motors cluster, multiple motors can simultaneously engage with the microtubule. The major goal of this thesis was to determine the organization of various motors on the vesicle membrane and also to understand the implications of this organization for transport. In order to do so, we first had to develop new multi-color super-resolution microscopy methods that overcome the limitations of previous methods. We developed a cross-talk free multi-color imaging approach that uses one fluorophore for the multiple colors and hence preserves maximal spatial resolution across the different colors. Applying this method to the question of motor protein organization, we have provided new insights into how different motor proteins are arranged on the lysosome membrane. We found that motors follow 2 different levels of organization. First, small team of motors assemble in clusters, and second, these teams further cluster onto a small patch of the membrane. This organization likely has important implications for transport, enabling multiple motors to engage simultaneously with the microtubule.

5.1 Cross-talk free multi-color imaging

We demonstrate multi-color STORM imaging using a single fluorophore, sequential labeling and imaging. Our first strategy was the following: a STORM image was acquire using a classic immunostaining method (primary-secondary antibodies) and the best performing fluorophore pair (A405-A647) on fixed cells. After the acquisition, the sample was bleached chemically using sodium borohydride. Another immunostaining was made using a different species for the primary antibody, but the same fluorophore pair on the secondary antibody (the best performing one, A405/A647). Another STORM image was done, and both images were precisely aligned. The positions of the same fiducials marker, homogeneously spread over the region of interest, in both STORM image are then used to calculate the 2D transformation using a local weighted mean algorithm. The ability to use the same fluorophore for multiple-colors also means that the extension of STORM to additional colors should only be restricted by the availability and performance of antibodies derived from distinct species. We also demonstrated that multiple targets can be imaged using the same antibody species and separated into multiple colors based on image segmentation. This approach provides additional flexibility for selecting antibodies for multicolor STORM, and is particularly important for STORM, since many of the antibodies for immunofluorescence which would have been acceptable for conventional microscopy methods do not produce a sufficiently high labeling density together with a sufficiently low background labeling for STORM. One example of a biologically-relevant scenario in which this approach would be

useful is depicted in the conceptual drawing in **Figure 5.1**. One can imagine a scenario in which it would be interesting to know whether ''nanoclusters'' of a given protein (Protein C) simultaneously colocalize with ''nanoclusters'' of two other proteins (Protein A and Protein B) that localize to different structures (e.g. pre- and post-synaptic membranes or mitochondrial outer and inner membranes). If only one well-performing antibody species exists that can properly label Protein A and Protein B (e.g. mouse), then these two proteins can be labelled and imaged together using this one antibody species. If needed, a second antibody species can be used (e.g. chicken, rat, donkey etc…) to label one of the structures (e.g. the post synaptic structure or the outer membrane) and carry out guided segmentation of Protein A and B into separate colors. Finally Protein C can be labelled with yet a third antibody species and its simultaneous colocalization with both Proteins A and B can be determined. Labeling only Protein A and C or only Protein B and C, in two separate experiments would not allow discrimination between the scenario in which Protein C colocalizes with Protein A and B separately but not both of them simultaneously. Our approach builds upon a recently developed multiplexed version of point accumulation for imaging in nanoscale topography (PAINT) which uses a single fluorophore to achieve multicolor super-resolution imaging with labelled oligonucleotides (Jungmann *et al.*, 2014). The approach we present here is a simpler and cost-effective alternative as it relies on simple immunofluorescence labeling without the need for oligonucleotides and without the need for lengthy imaging sessions or long periods of microscope down-time. In combination, these approaches enable cross-talk free imaging of b-cellular structures. The one major disadvantage of our method is that it requires a substantial time investment. Automation of this method for example using microfluidic devices (see below) can help streamline it.
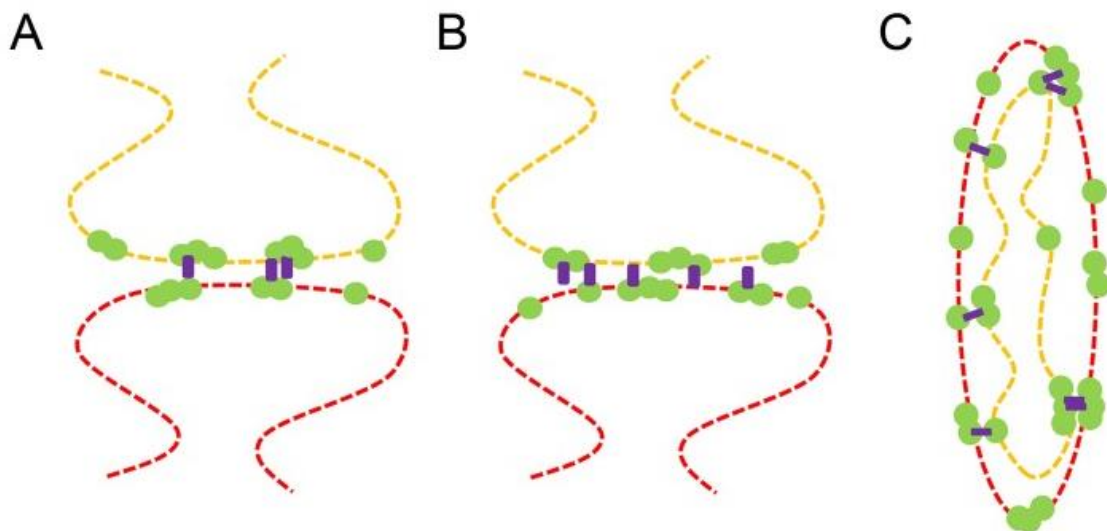
Fig 5.1 Conceptual application of multi-color STORM imaging using the same antibody species and same fluorophore. (A) Protein A (green) on the pre-synaptic structure (orange) and Protein B (green) on the post-synaptic structure (red) simultaneously colocalize with a third protein, Protein C (purple). (B) Protein C (purple) separately colocalizes with both Protein A (green) on the pre-synaptic structure (orange) and Protein B (green) on the post-synaptic structure (red) but rarely colocalizes

with both proteins simultaneously. Sequential imaging using the same antibody species to label Protein A and B can be used to distinguish between these two scenarios (C) A second example following the same scenario as (A) and (B) but with mitochondrial inner and outer membrane proteins.

5.2 Microfluidic platform for correlative live-cell and STORM imaging

We have combined correlative super-resolution and live-cell imaging with PDMS based microfluidic devices, automated and streamlined the sample preparation, and demonstrated an application to investigate mitochondrial dynamics in the context of their high-resolution morphology and their nanoscale membrane protein distribution. To the best of our knowledge, this is the first time that STORM has been successfully demonstrated using mammalian cells in microfluidic devices. Moreover, we show for the first time that correlative live cell and STORM can be performed using microfluidics. From a practical perspective, the design we used is simple and low-cost, making it accessible to laboratories without previous expertise in microfluidics. The use of external valves allows the microfluidic chip to be easily transported on and off the microscope stage, an important advantage over microfluidic chips that utilize on chip valves (Cheong, Paliwal and Levchenko, 2010). As a result of the external valves, the cell culture can be maintained off the microscope stage, and if needed the chip can be removed from the microscope stage when no imaging is being carried out and brought back at a later time for further imaging using a virtual grid approach to relocate the same region of interest (Tam *et al.*, 2014). This capability frees up the microscope during times where no data is collected, and allows for multiple batches to be prepared in parallel. Most designs that use on-chip valves do not allow this flexibility since the microfluidic device must typically be connected to a pressure source to keep the valves in their closed position. Selecting the simplest possible design minimizes operation cost and increases the reliability of the overall system. In particular, unlike previous systems, our imaging chamber is relatively large (2 cm x 1 mm). The use of a large imaging chamber enables cells to grow in larger populations, as a nearly-confluent monolayer providing healthy growth conditions and giving the researcher the freedom to select an appropriate cell for imaging. This is an important consideration when working with transfection of cells, which typically results in nonuniform expression levels due to the random insertion of DNA – in this case it is important to be able to select a cell that has an appropriate expression level. Finally, the modular design makes the microfluidic device flexible and provides a platform on which many future designs and experiments can be built. Although we have elected to use a very simple microfluidic chip, more advanced microfluidic techniques can be introduced by swapping out our current chip and by replacing it with a new design. With our current design, we have the ability to rapidly change the cellular microenvironment with fast fluid exchange. However, by replacing the chip with a new design, it would also be possible to generate and apply microgradients in concentration or in temperature (Jeon *et al.*, 2000; Mao, Yang and Cremer, 2002; Weibel

and Whitesides, 2006). Precise control over the cellular microenvironment could give important insights into how cells modify protein distributions in response to different perturbations. We have addressed a number of challenges that are associated with implementing microfluidics with other technologies, such as the additional optimization experiments that are needed to carry out immunostaining and STORM imaging. Sample preparation is especially important for high-resolution imaging methods such as STORM, since the improved resolution requires an even more stringent criterion for the preservation and labeling of sample features after fixation. In particular, high labeling densities must be achieved using higher-thantypical antibody concentrations. The labeling density is directly linked to the spatial resolution through the Nyquist criterion (the labeling density must be such that the distance between individual localizations in the resulting image is at least half of the desired resolution) (Lakadamyali et al.; Shroff et al.; Dempsey et al., see chapter 2). In addition, the imaging buffer conditions are crucial for inducing the desired photoswitching properties in the small organic fluorophores. Our results establish that with properly optimized sample preparation protocols, microfluidics and STORM can be combined. As a general guideline for future implementations of PDMS-based microfluidic chambers for STORM, based on our optimization tests, the antibody concentrations should be increased by about five-fold. The buffer conditions determined here should in principle work for all photoswitchable fluorophores that have similar photoswitching properties in thiol-based buffers. Together, these important optimization steps form the basis for integrating microfluidics with STORM microscopy.

We have developed a tool that can assay mitochondrial dynamics at a high temporal resolution (up to 50 ms temporal resolution) in relation to their morphology and protein distribution (up to 23.8 nm spatial resolution). Our data suggests that there may be different functional categories of mitochondria within a cell and that the morphology and dynamic behavior of a mitochondrion may be linked. One potential limitation of this approach is that the imaging of mitochondrial dynamics is performed at a higher temporal resolution but lower spatial resolution, which may lead to two mitochondria appearing to "interact" while in fact remaining "isolated" when examining only the live-cell imaging data. This miscategorization will lead to an overestimation of the interacting category. While there are currently other techniques available for live-cell imaging at higher spatial resolutions, the advantage of our approach is that we can achieve high temporal resolution (50 ms) at a very low laser power density (0.2 W.cm^{-2} at 561-nm) which minimizes and potential disturbances to the cell due to possible phototoxic effects.

In summary, we have demonstrated a versatile platform based on microfluidics for automated correlative microscopy that has the capability to image with both high temporal resolution (live-cell) and high spatial resolution (STORM). This platform adds to a growing list of recent ''systems microscopy'' approaches (Conrad and Gerlich, 2010; Lock and Strömblad, 2010; Neumann *et al.*, 2010; Conrad *et al.*, 2011) that address the need for automation in advanced microscopy and can be applied to investigate biological

phenomena at very high spatial and temporal scales with a wide range of potential applications which include cargo transport (Bálint *et al.*, 2013; Verdeny-Vilanova *et al.*, 2017b) and mitochondrial motility. The microfluidic automation can in principle be applied to other microscopy modalities such as the sequential multi-color imaging described above in order to streamline their operation.

5.3 Motor protein organization on the membrane of lysosomes

We took advantage of the previous cross talk free multicolor STORM method developed in our group (Tam *et al.*, 2014) to image at a high resolution lysosomes and motor proteins (whose size is below the diffraction of light limit). Our approach, which is done in the context of the cellular milieu contrasts with the *in vitro* experiments that were done until last decade to study and characterize motor protein behavior. Capturing the complex cellular environment can be challenging using bottom up in vitro approaches. So in complement to the bottom up approach (reconstruct cell conditions *in vitro*), the top down approach consisting of observing motor proteins and transport in the 3D context of a living cell can give new insights into this important biological question.

In this PhD thesis, we visualized only one motor type at a time. In the future, it would be interesting to carry out imaging of more than one motor on the lysosome membrane to determine whether the motor teams are composed only of one type of motor or if motors can form mixed teams. Further, it would be important to determine the molecular players that help organize motors into teams. Some potential players may be the lipid composition of the membrane or the adaptor proteins that may form platforms on the lysosome membrane for the assembly of motors. The clustering of motor teams on small patches of the membrane may be driven by the microtubule cytoskeleton. It would thus be interesting to depolymerize microtubules, modify the lipid content by pharmacological means or knock down adaptor proteins to determine the contribution of these different players on the 2-level organization we observed. Finally, it would be important to understand the implications of this organization for transport. Once the molecular mechanisms of motor organization are known, it would be possible to perturb the organization of motors by modifying the molecular players and use single particle tracking of lysosomes to study the impact on transport. In addition, correlative super-resolution and live cell imaging can be used to determine how the presence of different motor clusters impact the trafficking of individual lysosomes.

Summary and future directions

In summary, we developed novel methods that allowed us to visualize the organization of motor proteins on the membrane of vesicles with unprecedented spatial resolution and in the cellular context. These experiments helped us gain new insights into intracellular trafficking. In the future, it would be interesting to understand how the organization of

motors we describe here may be disrupted in diseases that affect intracellular trafficking. Further, the new methods we developed should be applicable to study other biological processes where multi-color imaging is important.

Appendix: Materials and Methods details

1. Sample preparation

Cell culture

Experiments described in **Chapters 3 and 4** were performed with genetically modified variants of the immortalized cell line: African green monkey (*Cercopithecus aethiops*) kidney epithelial cells (BS-C-1, American Type Culture Collection, ATCC, CCL-26). These cells are quite large (~50-100µm) and flat, thus, an appropriate imaging system for STORM. Most of the experiments were performed with the BS-C-1 cell line except for experiments in **(chapter 4)** where the BS-C-1 GFP-Tubulin and LAMP2-mCherry double stable cell line was used. Both stable cell lines were developed in our lab by Dr. Ángel Sandoval Álvarez. BS-C-1 cells were maintained in culture using a complete growth medium (Minimum Essential Medium Eagle with Earle's salts and nonessential amino acids plus 10% (v/v) FBS, 2 mM L-glutamine, and 1 mM sodium pyruvate; 500 µg/mL of Geneticin® (G418 Sulphate) to ensure continuity of the plasmid expression; penicillin-streptomycin to prevent bacterial contaminations) at 37°C and 5% carbon dioxide. The GFP-Tubulin and LAMP2-mCherry cell line stably expresses GFP together with ⍺-tubulin on microtubules and LAMP2 (Lysosomal Associated Membrane Protein – 2), one of the most abundant transmembrane proteins in lysosomes, together with the fluorescent protein mCherry attached to the C-terminal of LAMP2 and pointing towards the cytosolic side of lysosomes. This double stable cell line for GFP-Tubulin and LAMP2-mCherry (Lgp120NL-mCherry) was obtained by transfecting the plasmid pHyg-Lgp120NL-mCherry on top of the stably transfected cell line BS-C-1 GFPTubulin. This plasmid was constructed using the hygromycin resistance pcDNA5/FRT/TO vector as backbone. The cassette LAMP2-mCherry (Lgp120NLmCherry) was generated from plasmid Lgp120NL-PA-GFP, modified by replacing the PA-GFP with mCherry cloned in frame using *Bam*HI/*Xba*I restriction sites. This cassette was then amplified by PCR and cloned into the pcDNA5/FRT/TO vector using *Nhe*I/*Eco*RV restriction sites. The integrity of all these constructs was assessed by direct sequencing. BS-C-1 GFP-Tubulin stably transfected cell line was transfected with plasmid pHyg-LgpNL-mCherry and single clones were selected by adding Hygromycin B (Invitrogen 10687010) (100 µg/mL final concentration) to the cell culture medium. This double stably transfected cell line was maintained in culture using a complete growth medium (Minimum Essential Medium Eagle with Earle´s salts with nonessential amino acids supplemented with 10% (v/v) FBS, 2 mM Lglutamine, 1 mM sodium pyruvate and penicillin-streptomycin to prevent bacterial contaminations). Cell cultures were incubated at 37°C with 5% carbon dioxide. In order to ensure the stability of both plasmids 500 µg/mL of Geneticin® (G418 Sulfate) and 100 µg/mL Hygromycin B were added to the culture medium. For the imaging experiments, cells were plated on fibronectin (20 µg/mL) coated 8-well Lab-Tek 1 coverglass chamber (Nunc) containing fiduciary markers (Carboxyl Fluorescent Yellow microspheres 260 nm or Carboxyl Fluorescent Nile Red microspheres 240 nm, Spherotech) at a seeding density of 20000–50000 cells per well. Cell culture media and additives were purchased from GIBCO (Life Technologies).

Immunostaining

Cells in chapter 3 were fixed with 37°C warmed fixation buffer [3% (v/v) paraformaldehyde and 0.1% glutaraldehyde in PBS] for 10 min, then washed two times with 400 µL per well of PBS. Cells in chapter 4 were fixed with a -20°C mixture of methanol and ethanol (50%/50%) for 3 min at -20ºC, then washed two times with 400 µL per well of PBS. For cells in chapter 3 the background fluorescence of glutaraldehyde was quenched by incubating the cells with 200 µL per well of 0.1% NaBH4 solution in PBS for 7 min at room temperature. Finally, the cells were washed three times with PBS. After fixation, the cells were incubated for 60 min at room temperature with blocking buffer [3% (w/v) BSA, 0.2% TritonX-100 (Fisher Scientific) (v/v) in PBS] **(without Triton for cells in experiments in chapt4**). The blocking buffer was removed after one hour and the cells were incubated for 45 min with the appropriate dilution of primary antibody in blocking buffer. The primary antibodies were then removed and the cells rinsed with washing buffer [0.2% BSA, 0.05% TritonX-100 (Fisher Scientific)] three times (5 min each) **(without Triton for cells in experiments in chapt4**) Afterwards, the cells were incubated for 40 min, protected from light, with the appropriate dilutions of dye-labeled secondary antibodies. Finally, secondary antibodies were removed and the cells washed three times (5 min each) with PBS. In the sequential experiments, cells were incubated 10 min at room temperature with 0.1% NaBH4 solution in PBS, and then washed 2 times with PBS. For sequential experiments, subsequent immunostainings were similar to the procedure described above, except the initial incubation with blocking buffer was reduced to 5 minutes. The primary antibodies used in these experiments were against: Tom20 (Santa Cruz Biotechnology, sc-11415), alpha tubulin (Abcam, ab6160), and LAMP2 (DSHB, H4B4). The primary antibody used for dynein immunostaining was Mouse Monoclonal to DIC74.1 (Abcam, ab23905), at a dilution of 1:50. The primary antibody used for KIF3A immunostaining was Mouse Monoclonal to KIF3A [K2.4] (Abcam, ab24626), at a dilution of 1:50. The primary antibody used for KIF5B immunostaining was Mouse Monoclonal to KIF5B [SUK-4] (Abcam, ab 28060), at a dilution of 1:50. The secondary antibody used was AffiniPure Donkey anti Mouse IgG (H+L) (Jackson ImmunoResearch, 715-005-150) at a dilution of 1:100. The primary antibody used for endolysosome immunostaining was Chicken Polyclonal [YL1/2] to mCherry (Novus Biologicals, NBP2-25158. Lot# 6695), at a dilution of 1:500. The secondary antibody used was AffiniPure Donkey anti-Chicken IgY (IgG) (H+L) (Jackson ImmunoResearch, 703- 005-155) at a dilution of 1:100. For STORM imaging, the secondary antibodies were labeled in-house with Alexa Fluor® 405 – Alexa Fluor® A647 activator/reporter dye pair combination, at typical concentrations of 0.15 mg/ml, as previously described (Bates *et al.*, 2007). Briefly, the dyes were purchased as NHS-ester derivatives: Alexa Fluor® 405 Carboxylic Acid Succinimidyl Ester (Invitrogen), and Alexa Fluor® 647 Carboxylic Acid Succinimidyl Ester (Invitrogen). The antibody labeling reaction was performed by incubating a mixture containing the secondary antibody, NaHCO3, and the appropriate pair of activator/reporter dyes diluted in DMSO for 40 min at room temperature. Finally, purification of labeled antibodies was performed using NAP5 Columns (GE HealthCare).
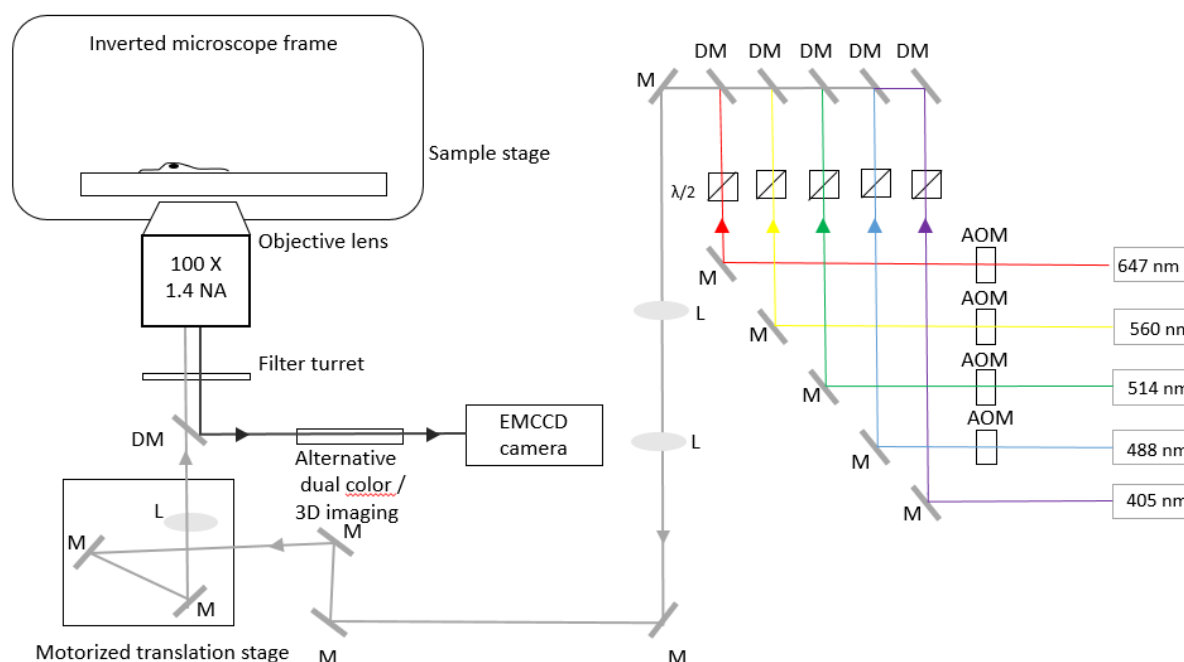
2 Experimental setup and imaging protocols

Fig A Schematic representation of the STORM experimental setup that I builded in 2015 together with Joseph Borberly.

Experimental setup

The experimental setup (schematic representation in **Fig. A**) used to perform the experiments described in chapter 3 is a home-built system with the capabilities for wide-field fluorescence TIRF microscopy and single-molecule localization based super-resolution fluorescence microscopy. The setup is divided in two separate optical tables equipped with a compressed air system that isolates the components on the table from environmental vibrations. One of the tables contains all the laser sources which are coupled to an optical fiber and directed to a second table where the microscope frame and the camera detector, among other optical components, are located. The purpose of this division is also to better isolate the microscope imaging system from additional vibrations coming from the laser sources. The laser sources consist of a multichannel argon-krypton laser (Spectrum IC70, Coherent) covering a range of wavelengths from 450-750nm approximately, a 405-nm solid-state laser (Cube, Coherent), and a 560-nm fiber laser (MPB Communications). The multichannel argon-krypton laser is split in multiple wavelengths (457, 488, 514, 647nm) by means of a prism and each laser line, as well as the 405nm and 560nm laser lines, are then directed to parallel paths containing the following combination of optical components: mirror - half-wave plate - polarizing beam splitter. The polarizing beam splitter allows us to homogenize the polarization among all laser lines such that all lines have the same linear polarization. In addition, the combination of half-wave plate and polarizing beam splitter enables individual control of the laser power for each laser line. All laser lines are combined into the same imaging path using dichroic mirrors and a telescope arrangement of two lenses adjusts the beam size before entering an acousto-optic tunable filter (AOTF; AOTFnC-400.650-TN, AA Opto-Electronic). The AOTF is a solid-state, electronically tunable bandpass filter, which uses the acoustooptic interaction inside an anisotropic medium to enable the

selection and transmission of a single wavelength (filtered in 1st order) from the incoming light by controlling the RF frequency applied on the AOTF. These devices allow for performing rapid switching between different illumination wavelengths for the required pulsed activation/excitation configuration of single-molecule localization based techniques, although pulsed laser excitation could be achieved using other configurations such as fast mechanical shutters or laser-software-controlled switching. In addition, the AOTF also allows for tuning of the laser power throughout the experiment, which is of particular importance since the activation laser power must be increased over time. The 1st-order laser light from the AOTF is directed to a half-wave plate for adjustment of the laser polarization and optimal coupling into a polarization dependent optical fiber (QPMJ-A3AC, 3C-405/650-3/125-3AS-7-1, OZ Optics Ltd.), and redirected to the second optical table where the microscope (IX71, Olympus) is located. The fiber-coupled laser light exits the fiber in the second optical table and, before entering into the microscope, the laser light is expanded and collimated with a telescope arrangement of two lenses. The collimated light is then directed into the microscope with a number of mirrors, such that the light is centered at the back aperture of the microscope. The microscope is a custom-built wide-field fluorescence microscope system based on an inverted Olympus IX71 microscope frame. The inverted configuration provides flexibility in terms of mounting and visualizing the sample as well as in terms of mounting multiple objectives, filter sets, and other components. A lens placed at the microscope back aperture focuses the laser light onto the objective back focal plane so that the light ultimately exits the objective as collimated. By placing the lens on a motorized translation stage, the light can be moved across the back aperture of the objective to change the angle of the incoming illumination from epi-fluorescence to TIRF. Sample excitation in single-molecule based super-resolution microscopy is typically performed in a close to TIRF or inclined illumination configuration to reduce the background coming from out-of focus planes, thus, a TIRF system is also a technical requirement. An active, home-built autofocusing system is used to keep the sample in focus and prevent z stage drift throughout the data collection process. This is especially important in imaging techniques such as STORM where the image acquisition is significantly long (from 30min to 2h approximately depending on the sample and imaging conditions). The autofocusing system consists of a commercialised focus lock system: Nikon Perfect Focus Sytem, correcting axial focus fluctuations in real time during long-STORM imaging. To maximize the light collection efficiency and to minimize aberrations and background fluorescence, we use a high quality TIRF oil-immersion objective with high magnification (100X), high numerical aperture (1.4 NA) and with the appropriate corrections for chromatic and other aberrations. Emitted light from the sample is then directed through an emission filter (a filter turret allows us to use the required emission filter based on the fluorescent label) and ultimately directed to the side port of the microscope and imaged onto an EMCCD (iXon DU-897, Andor Technology) camera. Single-molecule detection and localization requires very sensitive detectors along with an optical path that is optimized to maximize light collection efficiency. Thermoelectrically-cooled cameras incorporating electron multiplying charge coupled device (EMCCD) technology are the most commonly used devices. The image magnification is chosen such that the full width at half maximum of the PSF is equal in size to approximately 2.4 camera pixels. This leads to an effective pixel size of 160nm. Depending on the imaging requirements, dual-color imaging or 3D imaging capabilities are easily implemented between the EMCCD camera and the microscope side

port. For 3D imaging, a 1-m focal length cylindrical lens is inserted in front of the camera, as previously described in (Huang *et al.*, 2008)

Correlative experiments: experimental protocols

Confocal imaging

Confocal imaging was performed in the SLN microscope facilities from ICFO on a Leica TCS SP8 STED nanoscope. Confocal z-stacks were acquired after fixation. An 800-nm z range was scanned in 130 nm steps and the duration of a full z-stack acquisition was ~5 min. We used confocal set up to perform control experiment to characterize antibody specificity.

STORM imaging

For STORM imaging of the motor proteins (dynein and kinesin),motors were stained with antibodies conjugated with photoswitchable fluorophores (see immunostaining section in the ***Appendix*** for further details) and the activator-reporter dye pair formed by Alexa Fluor® 405 and Alexa Fluor® 647 (A405-A647) was the typically used label. The STORM imaging scheme for samples labeled with A405-A647 dye pairs consisted of A647 excitation and subsequent switching to the dark state with laser light at 647 nm from solid state laser(Coherent©), and reactivation of A647 fluorescence with the 405-nm solid-state laser via an activator dye (A405)–facilitated manner. A 488 nm pulse was also shinning the sample in order to excite carboxyl fluorescent nile red 240 nm (Spherotech) microspheres and help drift correction.). The emitted light from A647 was collected by the 100X objective, filtered by an emission filter (ET705/72m, Chroma) and imaged onto the EMCCD camera at a frame rate of 16 ms per frame. During image acquisition, a focus lock system was used to keep the sample in focus throughout the imaging process . The typical imaging sequence consisted of cycles of one frame of 405-nm and 488 nm laser activation followed by three frames of 647-nm excitation (405(x1)488(x1)-647(x3)). Super-resolution imaging with single-molecule localization based techniques such as STORM require relatively high power lasers in order to achieve the photoswitching of fluorophores. For A647 excitation, an output power of at least 200 mW (~1 kW.cm^{-2}) was used to enable fast switching times and rapid data collection. Reactivation of A647 fluorescence with the 405-nm laser required a gradual increase of the laser power (from 0 to 1.5 mW laser power before the objective, 20W.cm^{-2} on the sample) in order to control the density of single fluorescent molecules and avoid spatial overlapping. For 3D STORM imaging, a 1-m focal length cylindrical lens positioned in front of the camera (Huang *et al.*, 2008) was used. The imaging depth in 3D single particle tracking experiments was within ~200-300 nm of the glass surface where spherical aberrations did not significantly impact the imaging. The imaging buffer used for STORM experiments follows the recipe from original STORM literature (Bates, Jones and Zhuang, 2013). We particularly use MEA as the reducing agent because it allows for longer imaging. The imaging buffer consists of PBS 80x (v/v), MEA 10x (v/v), 50% glucose 10x (v/v), and GLOX (oxygen scavenger system based on glucose oxidase and catalase enzymes) 1x (v/v).

Microfluidic Chip Design and Fabrication

Microfluidic chips with miniaturized imaging chambers were designed using AutoCAD (Autodesk, Inc., Sausalito, CA) and fabricated by the Stanford Microfluidics Foundry in PDMS (RTV615, General Electric) using soft lithography. A single layer of PDMS was plasma bonded to a glass coverslip (Gold Seal Cover Slips, Thomas Scientific, Swedesboro, NJ). Each chip contains eight independent channels with a uniform flow height of 100 mm, a key difference

with previously used on-chip designs for immunostaining of mammalian cells (Cheong, Paliwal and Levchenko, 2010). A height of 100 mm allows for approximately four hours of culture time without fluid exchange (Young and Beebe, 2010) (important to allow for cell attachment, **Fig. B**). Since sterile conditions are critical for mammalian cell culture, but since the maintenance of sterility throughout an experiment can add unnecessary complexity and cost, we defined two working zones (**Fig. B and fig 3.2**). In the first zone, adherent mammalian cells are introduced and grown in a microfluidic chip under sterile conditions, using a conventional incubator. In the second zone, for the data collection portion of correlative imaging, since sterility was not necessary, the microfluidic device was transferred to the microscope for imaging once cells have adhered and reached the proper level of confluency.
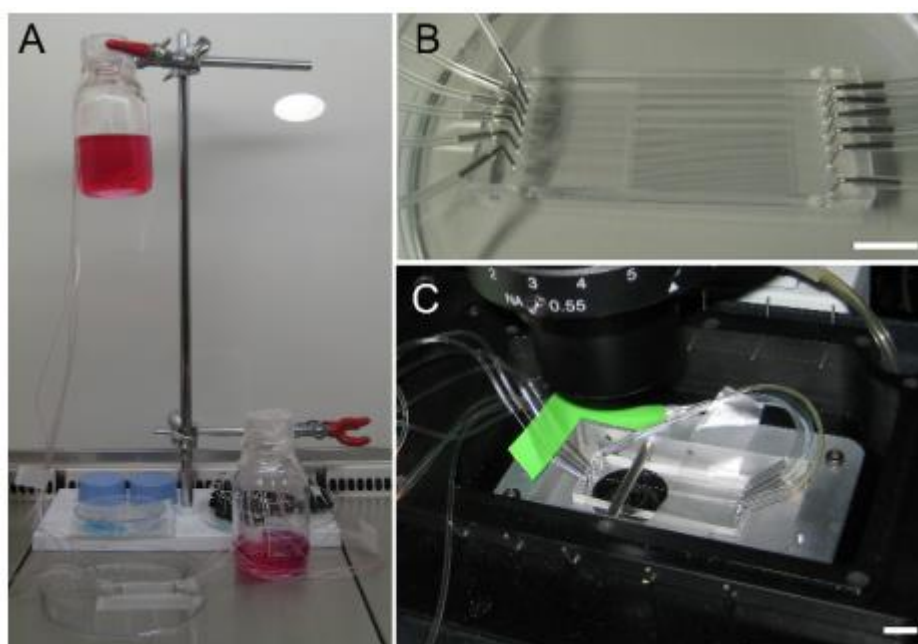
Fig B Overview of workflow. (A) Day 1. The microfluidic chip and cell culture materials are sterilized for thirty minutes and left overnight to equilibrate with complete growth medium under gravity flow, in a sterile hood. (B) Day 2. Mammalian cells are loaded into the microfluidic chip, left to attach for 2.5 to 4.5 hours (with no gravity flow), and then switched to perfusion culture overnight (with gravity flow). Scale bar, 1 cm. (C) Day 3. Livecell imaging, on-stage fixation, immunostaining, and STORM imaging are performed in a sequential manner. Scale bar, 1 cm

Automated Fluid Delivery System

The number of reagents and the timed sequence in which they are delivered varied depending on the immunostaining protocol and on the experimental conditions. We therefore developed a multiplexed design that could be easily modified to give flexibility to experimental strategy (**Fig. 3.2**). Instead of assigning each imaging channel to its own dedicated set of reagents, all imaging channels have access to a common set of fluid reservoirs. This allowed the numbers of reagents or imaging channels to be increased or decreased independently of upstream or downstream components, an important advantage over more complex and less flexible former designs that use on-chip valves (Cheong, Paliwal and Levchenko, 2010). Reagents were loaded into either 15 mL centrifuge tubes or Tygon microbore tubing (0.020060.0600 inner and outer diameter, Cole Parmer, Vernon Hills, IL),

connected to a Luer manifold, and pressurized with filtered Nitrogen gas. Fluid delivery was regulated using external solenoid pinch valves (2-way normally closed pinch valves and 3-way pinch valves outfitted for 0.023"x 0.093" inner and outer diameter C-Flex tubing, Bio-Chem Fluidics, Boonton, NJ). A data acquisition card (DAQ) (USB 6501, National Instruments) in combination with custom-written software (LabVIEW, National Instruments) and a custom-built electronics box was used to drive the solenoid valves. The DAQ configuration allowed for up to 24 digital outputs, organized into three ports of eight outputs. Instead of using each output to control one valve (resulting in a maximum of 24 valves), the first two ports were multiplexed to allow for more than 2,000 valves to be addressed by the DAQ (utilizing the first port to select which set of eight valves to control, and the second port to actuate up to eight valves). DAQ signals were read by a custom-built electronics box and used to switch individual power circuits on/off to provide the appropriate power needed for controlling the solenoid valves (24VDC at 150 mA per valve). The custom-built electronics box consisted of a rack-mount design with individual modules, each of which controlled up to eight valves. Together, the DAQ multiplexing and the rack-mount design provided a simple way to scale up or down the total number of solenoid valves. To minimize heating of solenoid valves, after 100 ms the input voltage was reduced to 8VDC, which still enabled the valves to remain on (Coolcube, Biochem Fluidics, Boonton, NJ). The LabView software to run the microfluidic device, along with the documentation on how to install and run the software can be found at https://github.com/LakadamyaliLab/microfluidic-control/blob/master/Automated_Valve_Control.zip

Optimization of Fluid Delivery in the Automated Immunostaining System

During microscopy, the pressure could be increased to generate rapid fluid exchange (**Fig. 3.2**). Using pressure-driven flow enabled precise control over fluid flow. We performed calibration experiments to establish the appropriate flow rates needed for on-stage fluid delivery (**Fig C**). Two-way and threeway solenoid pinch valves (075P2NC24-23B and 075P3MP24-23B, Biochem Fluidics, Boonton, NJ) with zero dead volume in combination with microbore tubing (Tygon microbore tubing, 0.02"x0.06" inner and outer diameter, Cole Parmer, Vernon Hills, IL, and C-Flex tubing, 0.023"x0.093" inner and outer diameter, Biochem Fluidics, Boonton, NJ) were used to minimize reagent consumption. Although the pinch valves were placed as close to the stage as possible to minimize the travel distance between the reagent reservoirs and the microfluidic chip, there was still a residual distance of 7' of Tygon microbore tubing between the imaging chamber in the microfluidic chip and the solenoid pinch valves, corresponding to a fluid overhead of approximately 35.5 mL. In addition, the binary multiplexer tree (for routing fluids between the different channels) required an additional 33.4 mL, which would have resulted in a combined fluid overhead of 68.9 mL per channel. We were able to decrease this overhead down to 20 mL per channel by using an alternate fluid delivery strategy based on moving a smaller bolus of fluid (e.g. having a bolus of antibody solution sandwiched by different fluids upstream and downstream). To ensure that the bolus was delivered to the chip, we tuned the fluid delivery such that the bolus was present both upstream and downstream of the chip. This corresponded to an overall reagent usage of 75 mL per channel (which includes a fluid overhead of 20 mL), or 300 mL per experiment (with four channels).
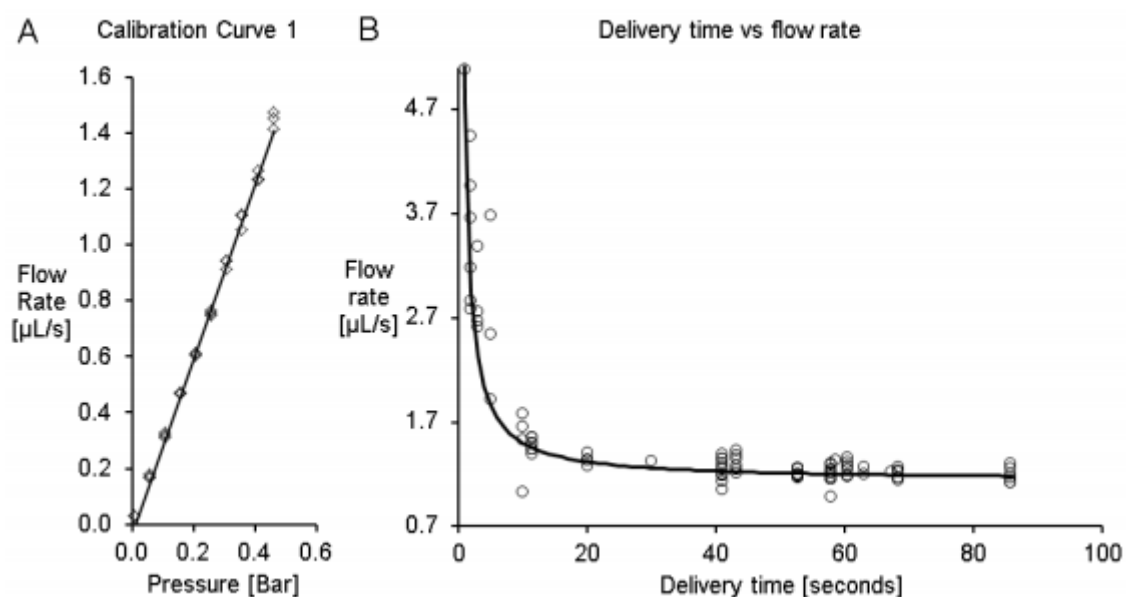
Fig C Calibration of the fluid delivery system. (A) The flow rate varies linearly with pressure for a fixed delivery time (least squares fit, y=3.12x-0.03, R^2 =0.99). (B) The flow rate has a non-linear dependence on the delivery time, due to the elasticity of the C-Flex tubing. For an input pressure of 0.5 bar, the average flow rate is approximately (3.61 + 1.14t)/t, where t refers to the delivery time, and flow rate is given in $\mu L.s^{-1}$. These calibration curves enable precise delivery of fluid volumes to the microscope stage.

Mammalian Cell Culture in the microfluidic chips

Prior to cell seeding, microfluidic chips and components were sterilized. Components were either purchased sterile, autoclaved, or sterilized using a combination of ethanol and ultraviolet light, as described below. For the sterilization step, the complete cell culture system was assembled in a sterile hood and a gravity-driven flow of pure ethanol was established. Care was taken during the initial priming steps (that is, during the initial filling of the tubing upstream of the microfluidic chip) to eliminate any bubbles. After priming, introduction of ethanol into the dry microfluidic chip by means of gravity flow resulted in complete filling of the microfluidic chip without bubbles. Once the gravity flow was established, the system was exposed to ultraviolet light for at least thirty minutes. Next, the ethanol was carefully replaced with complete growth medium, and gravity flow was re-established. Care was taken to not introduce any bubbles into the system. The complete growth medium was allowed to flow through the system overnight to equilibrate the PDMS with the complete growth medium. BS-C-1 Cells were seeded into microfluidic chambers at a seeding density of 4 to 6 million cells per mL and placed into an incubator and maintained at 37˚C and 5% CO2 for 2.5 to 4.5 hours to allow cells to attach to the bottom of the chamber. After attachment, slow but steady perfusion of complete growth medium (CGM) was established (Minimum Essential Medium, with Earle's salts and nonessential amino acids plus 10% (v/v) FBS, 2 mM L-glutamine, 1 mM sodium pyruvate, and a mixture of penicillin streptomycin; complete growth medium components purchased from GIBCO, Life Technologies). We performed calibration experiments to establish the appropriate flow rates needed for cell culture. This slow, steady flow rate was established using gravity-driven flow controlled by changing the difference in height between the media and waste reservoirs, without the need for any electrical or mechanical pumps or parts. For two-color imaging, immediately prior to cell seeding, microfluidic chips were incubated with fiduciary

beads (Nile Red, Spherotech), which were used to precisely align the sequentially-acquired STORM images of mitochondria and microtubules.

Live-cell Imaging

Live-cell imaging was performed using a previously-described custom-built microscope (Bálint *et al.*, 2013). Briefly, cells were imaged in epifluorescence wide-field microscopy using a 10061.4 NA oil-immersion objective. Cells were maintained on-stage at 37˚C using a temperature-controlled objective and stage heater (Live Cell Instrument). For one-color mitochondrial imaging, cells were incubated with MitoTracker orange (Invitrogen) at a concentration of 1 mM in CGM for 10 minutes at 37˚C, followed by a washing step of CGM. Cells were maintained in CGM during the live-cell imaging. A 560-nm fiber laser (MPB Communication) was used to excite the MitoTracker at a power between 0.2 and 0.5 W/cm2 . The emitted fluorescence passed through an emission filter (ET605/52, Chroma) and was collected with an electron-multiplying charge-coupled device (EM-CCD, Andor Technology) at a frame rate of either 10 or 20 frames per second. For two color imaging, the same procedures were performed with the following additional steps. During cell seeding, a well-established stably-transfected cell line for GFPtubulin was used, which were generated by transfecting BS-C-1 cells with a plasmid encoding GFP-tubulin and selectively screened through multiple passages (plasmid kind gift of Lynne Cassimeris, Lehigh University, Bethlehem, PA). A 488-nm line from an argon-krypton laser (Spectrum IC70, Coherent) was used to excite GFP at 1.0 W/cm2 and emitted fluorescence was collected after passing through an emission filter (ET525/50, Chroma).

3   Data analysis

To precisely align the different colors, fiduciary markers were used, which were recorded alongside the raw STORM data and localized alongside the other molecules to generate high-resolution images of each fiduciary marker. These marker positions were used to generate a transformation matrix that aligns one image onto the other one (see Evaluation of Registration Error). The first imaging session was used as a reference and the subsequent imaging sessions were aligned to the first image. For some images, multiple primary antibodies from the same species were used. The resulting images were segmented based on colocalization which was detected using both a custom-written software as well as manually. The custom written software determines colocalization as follows. The localizations of a particular channel are rendered at a resolution in which each pixel is 10x10 nm^2 (i.e., the precision of our image alignment). A binary image is generated from this rendered image such that every pixel in the binary image that contains a localization gets a value of 1 and every pixel that does not contain a localization gets a value of 0. A similar binary image is also generated for an additional channel of interest. A pixel-wise logical AND operation is performed between these two binary images to generate a colocalized binary mask. Additional image morphology techniques (such as opening, closing and hole-filling) can also be applied to this binary mask. The pixels in this binary mask that have a value of 1 represent pixels where colocalization occurs and the localizations for each channel that are within these pixels are extracted to render a high-resolution colocalized image. The colocalized images were further examined and any false assignments were corrected manually.High-resolution images were rendered and displayed in ImageJ. Areas of colocalization were delineated manually and then another custom-written software was

used to sort the localizations inside each molecule list based on whether or not they were inside the areas of colocalization. After molecule lists were split using this guided segmentation approach, all molecule lists were recombined and used to render a high-resolution STORM image with each list displayed as a separate color in Insight3. For traditional multicolor imaging, each peak was color coded based on whether the emission was recorded immediately after 405 nm or 532 nm activation cycle. The peaks coming from frames which did not immediately follow an activation frame were discarded from the analysis. STORM images were analyzed and rendered as previously described in ref. (Huang *et al.*, 2008) (see also ***Chapter 2***), using a custom-written software Insight3 (**Fig. D**), kindly provided by Dr. Bo Huang. Briefly, peaks in single-molecule images were identified based on a threshold and fit to a simple 2D Gaussian function for 2D STORM data or an elliptical Gaussian function for 3D STORM data. For the case of 3D STORM, the elliptical Gaussian fit allowed us to determine the x and y positions and the z positions were determined by comparing the widths of the point spread function in the x and y dimension to a predetermined calibration curve obtained using the particular STORM filter set (see ***Chapter 2*** for details). The calibration curve was determined by imaging 260 nm carboxyl fluorescent yellow microspheres (Spherotech) on glass at different focal planes using a piezoelectric z stage. Sample drift during acquisition was calculated and subtracted by reconstructing STORM images from subsets of frames (typically 500– 2000 frames, for which drift was assumed to be small) and correlating these images to a reference frame (typically one that is reconstructed at the initial time segment) (Bates *et al.*, 2007). The final images were visualized by using a Gaussian rendering with a width corresponding to the determined localization precision.
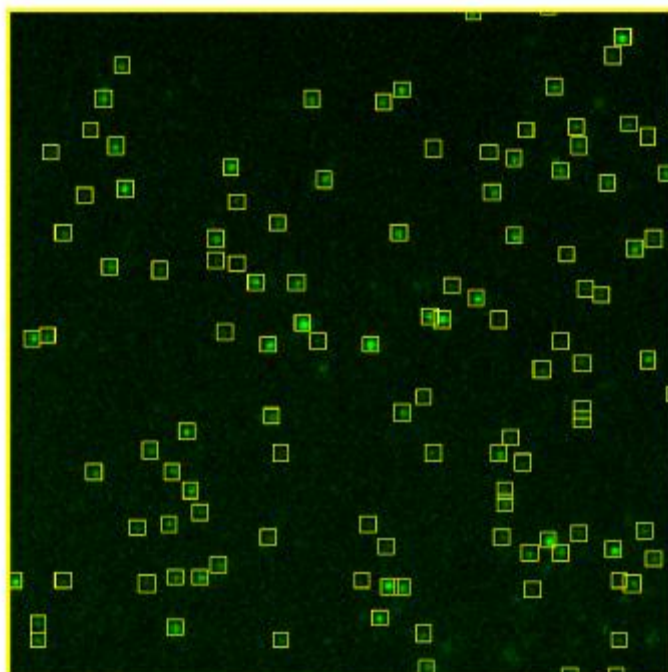

Figure D. STORM data analysis software: Insight3. Interface of Insight3 showing an example frame from a STORM acquisition where the yellow squares correspond to the single molecules that have been identified. The software allows for 2D and 3D data analysis and it includes drift correction, cross talk correction and spherical aberration correction capabilities among others.

The super-resolution raw localizations were first filtered to remove outlier localizations that were more than one standard deviation away from the mean z-position of all the localizations. Next, the remaining localizations were smoothed by averaging over N localizations, in which N was given by one-tenth of the total number of localizations in that particular super-resolution image of the microtubule. Finally, a three-dimensional linear fit was performed on the smoothed localizations to extract the microtubule position.

Classification of mitochondrial dynamics

Mitochondria were systematically identified and classified according to their dynamic category using custom-written software in addition to ImageJ. Only those mitochondria which were clearly identifiable in both the high-resolution STORM image and its corresponding live video were included in the analysis. Specifically, those mitochondria which were partially out of focus, residing in dense regions with overlapping mitochondria, or exhibiting multiple dynamic behaviors were excluded from analysis. Based on examination of the live videos, mitochondria were manually classified as isolated, interacting, dynamic-slow, dynamic-fast, and stationary. All classifications were performed by one trained operator who was blind to quantitative data generated from the STORM images. In addition, a particle and filament tracking program (FIESTA) (Ruhnow, Zwicker and Diez, 2011) was used to confirm the classification based on the maximum displacement of mitochondria from their starting position as well as the average speed.

Quantification of Tom20 labeling density and image resolution

For each of the mitochondrion selected for analysis, an outline of the mitochondrion in the STORM image was manually generated using ImageJ. This outline was used to quantify the area in pixels^2 , which was then converted to μm^2 based on the pixel size of the camera in the sample plane (0.157 μm.pixel^{-1} in each direction). Next, using custom-written software, all the molecules which were localized inside the outline were selected and counted. The Tom20 labeling density was calculated by dividing the number of localizations within each mitochondria by the area of the mitochondria. Finally, the Tom20 density was normalized by dividing by the median density of the dataset. This approach in principle overestimates the Tom20 density since each fluorophore can give rise to more than one localization and each Tom20 may be labeled by more than one antibody. However, we assume that the density will be similarly overestimated across all dynamic categories, therefore not influencing the comparative analysis. The resolution (R) of the image was calculated by adding in quadrature a labeling density-based estimate of image resolution (R1) and the localization precision of the microscope system (R2) (Lakadamyali *et al.*, 2012), where

$$R = \sqrt{(R_1)^2 + (R_2)^2}$$

$$R_1 = \frac{2}{\sqrt{number\ of\ localizations\ per\ nm^2}}$$

$$R_2 = 9\ nm$$

This calculation was performed for each mitochondria and then averaged to determine the average image resolution.

Statistical Analysis

Groups were compared using two-tailed, unpooled t-tests with a significance value of 0.001.

Evaluation of the registration error

A thousand-frame movie of fiduciary markers (fluorescent beads) was recorded. Next, the sample was taken off the stage, the same region of interest was relocated and a second thousand frames movie of the beads was recorded. In addition, the same fiduciary markers were imaged using two different filter sets (set 1: ZT660 dichroic and ET705/72 emission filter; set 2: ZT488/561/ 642RPC dichroic and ET525/50 emission filter). The position of the beads was identified in each frame, leading to a small cluster of bead positions. The centroid cluster positions of the corresponding bead localizations in the two images were used for computing a transformation function. For choosing optimal beads for the registration the total perimeter of the polygon (a triangle in the case of three beads) enclosed by different bead combinations was computed and the beads that gave the largest perimeter were chosen. This approach enabled one to choose beads that were evenly distributed and covered a large range across the field of view. Two registration algorithms were tested by using a varying number of beads to carry out the registration (n = 3 to n = 10 beads). The first algorithm used a first-order polynomial affine transformation while the second algorithm used a second order polynomial local weighted mean transformation (the 'cp2tform' function of Matlab was used for each algorithm). The registration error was defined as the average distance between the transformed centroid positions from one movie with the centroid positions from the other movie (Equation 1):

$$Registration\ Error = \frac{1}{N}\sum_{i=1}^{N}\sqrt{\Delta x_i^2 + \Delta y_i^2} \quad (Equation\ 1)$$

where Δx_i is the shift between the x-centroid positions of the ith bead in the two images and Δy_i is the shift between the y-centroid positions of the ith bead in the two images.

DNA origami analysis

The DNA origami work has been done in our laboratory, on the same set up, excluding any artefacts due to a different system. The methods here explained can be found in (Zanacchi *et al.*, 2017). The distribution of the number of localizations for a structure composed by n dynein can be recursively obtained as

$$f_n = f_{n-1} \times f_1$$

where x represent the convolution and f_1 is a log-normal distribution:

$$f_1(x) = \frac{1}{x\sigma\sqrt{2\pi}} e^{-\frac{(\ln x - \mu)^2}{2\sigma^2}}$$

The distributions of localizations obtained for 1,2,3,4,5,6,7,8 dyneins were simultaneously fitted to the functions f_2, f_3, f_4 etc. obtaining the parameters $\mu = 3.35$ and $\sigma = 0.85$. To quantify

dynein labeled by means of different antibodies we have to consider that the different labeling condition will produce a different calibration function. For this reason we found the optimal parameters for the lognormal distribution through the comparison of measurements the distributions obtained labeling dynein intermediate chain in HeLa IC74 cells using anti GFP antibodies and in HeLa cells wild type using anti dynein antibodies, Mouse Monoclonal to DIC74.1 (Abcam, ab23905). The analysis provided a new lognormal calibration function with parameters µ =2.6 and σ =0.545. The log-normal distribution was chosen because, among several tested distributions, it provided the best data model.

For a general distribution of number of localizations, the copy number of a given protein can thus be estimated by fitting the distributions to a linear combination of the "calibration" distribution of f_n

$$g(x) = \sum_{n=1}^{N_{max}} \alpha_n f_n(x)$$

Where α_n represents the weight of the distribution of n-mers and

$$\sum_{n=1}^{N_{max}} \alpha_n = 1$$

Fitting are performed by a two-step numerical minimization of the objective function:

$$F = -\omega_L \sum_x p(x) lng(g) + \omega_E \sum_n \alpha_n ln\alpha_n$$

Which represents the sum of the negative log-likelyhood and the entropy. In the first term, p(x) corresponds to the number of occurences for number of localization x. In the first optimization step, ω_L was set to $\omega_L=1$ and $\omega_E = \dfrac{max(x) - min(x)}{<x>}$, with <x> representing the average value of the data, and let the optimization run at varying N_{max} until the minimum of the objective function F_{min} is found. By means of this procedure, the maximum number of loglikelihood is set ti the inverse of its target value $w_L=1/F_{min}$. Calculation of the errors on the estimated weights α_n was based on the reciprocal of the diagonal elements of the Fisher information matrix and thus represents a lower bound to the standard error of the estimators. The code can be found at https://github.com/cmanzo/DECO

References

Andreasson, J. O. L. *et al.* (2015) 'The Mechanochemical Cycle of Mammalian Kinesin-2 KIF3A/B under Load', *Current Biology*, 25, pp. 1166–1175. doi: 10.1016/j.cub.2015.03.013.

Andronov, L. *et al.* (2016) 'ClusterViSu, a method for clustering of protein complexes by Voronoi tessellation in super-resolution microscopy', *Scientific Reports*. Nature Publishing Group, 6(1), p. 24084. doi: 10.1038/srep24084.

Anishkin, A. and et al (2013) 'Stiffened lipid platforms at molecular force foci.', *Proceedings of the National Academy of Sciences of the United States of America*. National Academy of Sciences, 110(13), pp. 4886–92. doi: 10.1073/pnas.1302018110.

Babcock, H., Sigal, Y. M. and Zhuang, X. (2012) 'A high-density 3D localization algorithm for stochastic optical reconstruction microscopy.', *Optical nanoscopy*. NIH Public Access, 1(6). doi: 10.1186/2192-2853-1-6.

Bálint, Š. *et al.* (2013) 'Correlative live-cell and superresolution microscopy reveals cargo transport dynamics at microtubule intersections.', *Proceedings of the National Academy of Sciences of the United States of America*. National Academy of Sciences, 110(9), pp. 3375–80. doi: 10.1073/pnas.1219206110.

Bananis, E. *et al.* (2004) 'Microtubule-dependent movement of late endocytic vesicles in vitro: requirements for Dynein and Kinesin.', *Molecular biology of the cell*. American Society for Cell Biology, 15(8), pp. 3688–97. doi: 10.1091/mbc.E04-04-0278.

Bates, M. *et al.* (2005) 'Short-Range Spectroscopic Ruler Based on a Single-Molecule Optical Switch', *Physical Review Letters*, 94(10), p. 108101. doi: 10.1103/PhysRevLett.94.108101.

Bates, M. *et al.* (2007) 'Multicolor super-resolution imaging with photo-switchable fluorescent probes.', *Science (New York, N.Y.)*, 317(5845), pp. 1749–53. doi: 10.1126/science.1146598.

Bates, M. *et al.* (2012) 'Multicolor Super-Resolution Fluorescence Imaging via Multi-Parameter Fluorophore Detection', *ChemPhysChem*, 13(1), pp. 99–107. doi: 10.1002/cphc.201100735.

Bates, M., Jones, S. A. and Zhuang, X. (2013) 'Stochastic Optical Reconstruction Microscopy (STORM): A Method for Superresolution Fluorescence Imaging', *Cold Spring Harbor Protocols*, 2013(6), p. pdb.top075143. doi: 10.1101/pdb.top075143.

Baudhuin, P. *et al.* (1965) 'Combined biochemical and morphological study of particulate fractions from rat liver. Analysis of preparations enriched in lysosomes or in particles containing urate oxidase, D-amino acid oxidase, and catalase.', *The Journal of cell biology*. The Rockefeller University Press, 26(1), pp. 219–43. Available at: http://www.ncbi.nlm.nih.gov/pubmed/4379260 (Accessed: 15 June 2017).

References

Benke, A. and Manley, S. (2012) 'Live-Cell dSTORM of Cellular DNA Based on Direct DNA Labeling', *ChemBioChem*, 13(2), pp. 298–301. doi: 10.1002/cbic.201100679.

Berezuk, M. A. and Schroer, T. A. (2007) 'Dynactin Enhances the Processivity of Kinesin-2', *Traffic*, 8(2), pp. 124–129. doi: 10.1111/j.1600-0854.2006.00517.x.

Berthier, E. *et al.* (2012) 'Engineers are from PDMS-land, Biologists are from Polystyrenia', *Lab on a Chip*. The Royal Society of Chemistry, 12(7), p. 1224. doi: 10.1039/c2lc20982a.

Betzig, E. *et al.* (2006) 'Imaging Intracellular Fluorescent Proteins at Nanometer Resolution', *Science*. Available at: http://science.sciencemag.org/content/early/2006/08/10/science.1127344 (Accessed: 7 August 2017).

Bhabha, G. *et al.* (2014) 'Allosteric Communication in the Dynein Motor Domain', *Cell*, 159(4), pp. 857–868. doi: 10.1016/j.cell.2014.10.018.

Bielli, A. *et al.* (2001) 'The Small GTPase Rab4A Interacts with the Central Region of Cytoplasmic Dynein Light Intermediate Chain-1', *Biochemical and Biophysical Research Communications*, 281(5), pp. 1141–1153. doi: 10.1006/bbrc.2001.4468.

Biteen, J. S. *et al.* (2008) 'Super-resolution imaging in live Caulobacter crescentus cells using photoswitchable EYFP', *Nature Methods*, 5(11), pp. 947–949. doi: 10.1038/nmeth.1258.

Block, S. M., Goldstein, L. S. B. and Schnapp, B. J. (1990) 'Bead movement by single kinesin molecules studied with optical tweezers', *Nature*. Nature Publishing Group, 348(6299), pp. 348–352. doi: 10.1038/348348a0.

Brakemann, T. *et al.* (2011) 'A reversibly photoswitchable GFP-like protein with fluorescence excitation decoupled from switching', *Nature Biotechnology*, 29(10), pp. 942–947. doi: 10.1038/nbt.1952.

Brede, N. and Lakadamyali, M. (2012) 'GraspJ: an open source, real-time analysis package for super-resolution imaging', *Optical Nanoscopy*, 1(1), p. 11. doi: 10.1186/2192-2853-1-11.

Brown, C. L. *et al.* (2005) 'Kinesin-2 is a Motor for Late Endosomes and Lysosomes', *Traffic*, 6(12), pp. 1114–1124. doi: 10.1111/j.1600-0854.2005.00347.x.

Burgess, S. A. *et al.* (2003) 'Dynein structure and power stroke.', *Nature*, 421(6924), pp. 715–8. doi: 10.1038/nature01377.

Cai, Q. *et al.* (2010) 'Snapin-Regulated Late Endosomal Transport Is Critical for Efficient Autophagy-Lysosomal Function in Neurons', *Neuron*, 68, pp. 73–86. doi: 10.1016/j.neuron.2010.09.022.

Cai, Q., Gerwin, C. and Sheng, Z.-H. (2005) 'Syntabulin-mediated anterograde transport of mitochondria along neuronal processes', *The Journal of Cell Biology*, 170(6), pp. 959–969. doi: 10.1083/jcb.200506042.

Can, S. *et al.* (2014) 'Bidirectional helical motility of cytoplasmic dynein around

microtubules', *eLife*, 3. doi: 10.7554/eLife.03205.

Carter, A. P. *et al.* (2011) 'Crystal structure of the dynein motor domain.', *Science (New York, N.Y.)*, 331(6021), pp. 1159–65. doi: 10.1126/science.1202393.

Carter, A. P. (2013) 'Crystal clear insights into how the dynein motor moves', *Journal of Cell Science*, 126(3), pp. 705–713. doi: 10.1242/jcs.120725.

Carter, A. P., Diamant, A. G. and Urnavicius, L. (2016) 'How dynein and dynactin transport cargos: a structural perspective', *Current Opinion in Structural Biology*, 37, pp. 62–70. doi: 10.1016/j.sbi.2015.12.003.

Carter, N. J. and Cross, R. A. (2005) 'Mechanics of the kinesin step.', *Nature*, 435(7040), pp. 308–12. doi: 10.1038/nature03528.

Cattoni, D. I. *et al.* (2013) 'Super-Resolution Imaging of Bacteria in a Microfluidics Device', *PLoS ONE*. Edited by D.-J. Scheffers. Public Library of Science, 8(10), p. e76268. doi: 10.1371/journal.pone.0076268.

Chan, D. C. (2006) 'Mitochondria: Dynamic Organelles in Disease, Aging, and Development', *Cell*, 125(7), pp. 1241–1252. doi: 10.1016/j.cell.2006.06.010.

Chen, H. *et al.* (2008) 'Cholesterol Level Regulates Endosome Motility via Rab Proteins', *Biophysical Journal*, 94(4), pp. 1508–1520. doi: 10.1529/biophysj.106.099366.

Chen, H. and Chan, D. C. (2009) 'Mitochondrial dynamics--fusion, fission, movement, and mitophagy--in neurodegenerative diseases.', *Human molecular genetics*, 18(R2), pp. R169-76. doi: 10.1093/hmg/ddp326.

Cheong, R., Paliwal, S. and Levchenko, A. (2010) 'High-content screening in microfluidic devices', *Expert Opinion on Drug Discovery*, 5(8), pp. 715–720. doi: 10.1517/17460441.2010.495116.

Collins, T. J. *et al.* (2002) 'Mitochondria are morphologically and functionally heterogeneous within cells.', *The EMBO journal*. European Molecular Biology Organization, 21(7), pp. 1616–27. doi: 10.1093/emboj/21.7.1616.

Conrad, C. *et al.* (2011) 'Micropilot: automation of fluorescence microscopy–based imaging for systems biology', *Nature Methods*, 8(3), pp. 246–249. doi: 10.1038/nmeth.1558.

Conrad, C. and Gerlich, D. W. (2010) 'Automated microscopy for high-content RNAi screening', *The Journal of Cell Biology*, 188(4). Available at: http://jcb.rupress.org/content/188/4/453 (Accessed: 7 September 2017).

Culver–Hanlon, T. L. *et al.* (2006) 'A microtubule-binding domain in dynactin increases dynein processivity by skating along microtubules', *Nature Cell Biology*, 8(3), pp. 264–270. doi: 10.1038/ncb1370.

Dempsey, G. T. *et al.* (2009) 'Photoswitching Mechanism of Cyanine Dyes', *Journal of the American Chemical Society*, 131(51), pp. 18192–18193. doi: 10.1021/ja904588g.

References

Dempsey, G. T. *et al.* (2009) 'Photoswitching mechanism of cyanine dyes.', *Journal of the American Chemical Society*. American Chemical Society, 131(51), pp. 18192–3. doi: 10.1021/ja904588g.

Dempsey, G. T. *et al.* (2011) 'Evaluation of fluorophores for optimal performance in localization-based super-resolution imaging', *Nature Methods*, 8(12), pp. 1027–1036. doi: 10.1038/nmeth.1768.

Derr, N. D. *et al.* (2012) 'Tug-of-War in Motor Protein Ensembles Revealed with a Programmable DNA Origami Scaffold', *Science*, 338(6107), pp. 662–665. doi: 10.1126/science.1226734.

Detmer, S. A. and Chan, D. C. (2007) 'Functions and dysfunctions of mitochondrial dynamics', *Nature Reviews Molecular Cell Biology*, 8(11), pp. 870–879. doi: 10.1038/nrm2275.

DeWitt, M. A. *et al.* (2012) 'Cytoplasmic dynein moves through uncoordinated stepping of the AAA+ ring domains.', *Science (New York, N.Y.)*, 335(6065), pp. 221–5. doi: 10.1126/science.1215804.

Dixit, R. *et al.* (2008) 'Differential Regulation of Dynein and Kinesin Motor Proteins by Tau', *Science*, 319(5866), pp. 1086–1089. doi: 10.1126/science.1152993.

De Duve, C. *et al.* (1955) 'Tissue fractionation studies. 6. Intracellular distribution patterns of enzymes in rat-liver tissue.', *The Biochemical journal*. Portland Press Ltd, 60(4), pp. 604–17. Available at: http://www.ncbi.nlm.nih.gov/pubmed/13249955 (Accessed: 15 June 2017).

Efimov, V. P. and Morris, N. R. (2000) 'The LIS1-related NUDF protein of Aspergillus nidulans interacts with the coiled-coil domain of the NUDE/RO11 protein.', *The Journal of cell biology*, 150(3), pp. 681–8. Available at: http://www.ncbi.nlm.nih.gov/pubmed/10931877 (Accessed: 20 September 2017).

Erickson, R. P. *et al.* (2011) 'How Molecular Motors Are Arranged on a Cargo Is Important for Vesicular Transport', *PLoS Computational Biology*. Edited by A. R. Bausch. Public Library of Science, 7(5), p. e1002032. doi: 10.1371/journal.pcbi.1002032.

Eskelinen, E.-L. *et al.* (2004) 'Disturbed Cholesterol Traffic but Normal Proteolytic Function in LAMP-1/LAMP-2 Double-deficient Fibroblasts', *Molecular Biology of the Cell*, 15(7), pp. 3132–3145. doi: 10.1091/mbc.E04-02-0103.

Fåhræus, R. and Lindqvist, T. (1931) 'THE VISCOSITY OF THE BLOOD IN NARROW CAPILLARY TUBES', *American Journal of Physiology-Legacy Content*, 96(3), pp. 562–568. doi: 10.1152/ajplegacy.1931.96.3.562.

Feng, Y. *et al.* (2000) 'LIS1 regulates CNS lamination by interacting with mNudE, a central component of the centrosome.', *Neuron*, 28(3), pp. 665–79. Available at: http://www.ncbi.nlm.nih.gov/pubmed/11163258 (Accessed: 20 September 2017).

Fu, M.-M., Nirschl, J. J. and Holzbaur, E. L. F. (2014) 'LC3 binding to the scaffolding protein

JIP1 regulates processive dynein-driven transport of autophagosomes.', *Developmental cell*. NIH Public Access, 29(5), pp. 577–590. doi: 10.1016/j.devcel.2014.04.015.

Fu, M. and Holzbaur, E. L. F. (2013) 'JIP1 regulates the directionality of APP axonal transport by coordinating kinesin and dynein motors', *The Journal of Cell Biology*, 202(3). Available at: http://jcb.rupress.org/content/202/3/495 (Accessed: 15 June 2017).

Fu, M. and Holzbaur, E. L. F. (2014) 'Integrated regulation of motor-driven organelle transport by scaffolding proteins.', *Trends in cell biology*, 24(10), pp. 564–74. doi: 10.1016/j.tcb.2014.05.002.

Fürstenberg, A. and Heilemann, M. (2013) 'Single-molecule localization microscopy – near-molecular spatial resolution in light microscopy with photoswitchable fluorophores', *Physical Chemistry Chemical Physics*, 15(36), p. 14919. doi: 10.1039/c3cp52289j.

Gennerich, A. *et al.* (2007) 'Force-induced bidirectional stepping of cytoplasmic dynein.', *Cell*, 131(5), pp. 952–65. doi: 10.1016/j.cell.2007.10.016.

Gibbons, I. R. and Rowe, A. J. (1965) 'Dynein: A Protein with Adenosine Triphosphatase Activity from Cilia', *Science*, 149(3682), pp. 424–426. doi: 10.1126/science.149.3682.424.

Glater, E. E. *et al.* (2006) 'Axonal transport of mitochondria requires milton to recruit kinesin heavy chain and is light chain independent', *The Journal of Cell Biology*, 173(4), pp. 545–557. doi: 10.1083/jcb.200601067.

Granger, E. (2014) 'The role of the cytoskeleton and molecular motors in endosomal dynamics', *Seminars in Cell & Developmental Biology*. Academic Press, 31, pp. 20–29. doi: 10.1016/J.SEMCDB.2014.04.011.

Griffié, J. *et al.* (2016) 'A Bayesian cluster analysis method for single-molecule localization microscopy data', *Nature Protocols*, 11(12), pp. 2499–2514. doi: 10.1038/nprot.2016.149.

Grigoriev, I. *et al.* (2007) 'Rab6 Regulates Transport and Targeting of Exocytotic Carriers', *Developmental Cell*, 13(2), pp. 305–314. doi: 10.1016/j.devcel.2007.06.010.

Gross, S. P. *et al.* (2000) 'Dynein-Mediated Cargo Transport in Vivo: A Switch Controls Travel Distance', *The Journal of Cell Biology*. The Rockefeller University Press, 148(5), p. 945. Available at: https://www.ncbi.nlm.nih.gov/pmc/articles/PMC2174539/ (Accessed: 15 June 2017).

Gross, S. P. *et al.* (2002) 'Coordination of opposite-polarity microtubule motors', *The Journal of Cell Biology*, 156(4), pp. 715–724. doi: 10.1083/jcb.200109047.

Gross, S. P. *et al.* (2002) 'Coordination of opposite-polarity microtubule motors.', *The Journal of cell biology*. The Rockefeller University Press, 156(4), pp. 715–24. doi: 10.1083/jcb.200109047.

Gross, S. P. *et al.* (2007) 'Cargo Transport: Two Motors Are Sometimes Better Than One', *Current Biology*, 17(12), pp. R478–R486. doi: 10.1016/j.cub.2007.04.025.

Gurskaya, N. G. *et al.* (2006) 'Engineering of a monomeric green-to-red photoactivatable fluorescent protein induced by blue light', *Nature Biotechnology*, 24(4), pp. 461–465. doi: 10.1038/nbt1191.

Gustafsson, M. G. L. (2005) 'Nonlinear structured-illumination microscopy: wide-field fluorescence imaging with theoretically unlimited resolution.', *Proceedings of the National Academy of Sciences of the United States of America*. National Academy of Sciences, 102(37), pp. 13081–6. doi: 10.1073/pnas.0406877102.

Ha, T. and Tinnefeld, P. (2012) 'Photophysics of Fluorescent Probes for Single-Molecule Biophysics and Super-Resolution Imaging', *Annual Review of Physical Chemistry*, 63(1), pp. 595–617. doi: 10.1146/annurev-physchem-032210-103340.

Habermann, A. *et al.* (2001) 'Immunolocalization of cytoplasmic dynein and dynactin subunits in cultured macrophages: enrichment on early endocytic organelles.', *Journal of cell science*, 114(Pt 1), pp. 229–240. Available at: http://www.ncbi.nlm.nih.gov/pubmed/11112706 (Accessed: 13 July 2017).

Habuchi, S. *et al.* (2005) 'Reversible single-molecule photoswitching in the GFP-like fluorescent protein Dronpa.', *Proceedings of the National Academy of Sciences of the United States of America*, 102(27), pp. 9511–6. doi: 10.1073/pnas.0500489102.

Habuchi, S. *et al.* (2008) 'mKikGR, a Monomeric Photoswitchable Fluorescent Protein', *PLoS ONE*. Edited by S. Zhang, 3(12), p. e3944. doi: 10.1371/journal.pone.0003944.

Heilemann, M. *et al.* (2005) 'Carbocyanine dyes as efficient reversible single-molecule optical switch.', *Journal of the American Chemical Society*, 127(11), pp. 3801–6. doi: 10.1021/ja044686x.

Hell, S. W. and Wichmann, J. (1994) 'Breaking the diffraction resolution limit by stimulated emission: stimulated-emission-depletion fluorescence microscopy', *Optics Letters*. Optical Society of America, 19(11), p. 780. doi: 10.1364/OL.19.000780.

Hendricks, A. G. *et al.* (2010) 'Motor Coordination Via Tug-Of-War Mechanism Drives Bidirectional Vesicle Transport', *Current biology : CB*. NIH Public Access, 20(8), p. 697. doi: 10.1016/j.cub.2010.02.058.

Hendricks, A. G. *et al.* (2012) 'Force measurements on cargoes in living cells reveal collective dynamics of microtubule motors', *Proceedings of the National Academy of Sciences*. National Academy of Sciences, 109(45), pp. 18447–18452. doi: 10.1073/PNAS.1215462109.

Hendricks, A. G., Holzbaur, E. L. F. and Goldman, Y. E. (2012) 'Force measurements on cargoes in living cells reveal collective dynamics of microtubule motors.', *Proceedings of the National Academy of Sciences of the United States of America*. National Academy of Sciences, 109(45), pp. 18447–52. doi: 10.1073/pnas.1215462109.

Hess, S. T. *et al.* (2006) 'Ultra-High Resolution Imaging by Fluorescence Photoactivation Localization Microscopy', *Biophysical Journal*, 91(11), pp. 4258–4272. doi: 10.1529/biophysj.106.091116.

Hirokawa, N. *et al.* (2009) 'Kinesin superfamily motor proteins and intracellular transport', *Nature Reviews Molecular Cell Biology*, 10(10), pp. 682–696. doi: 10.1038/nrm2774.

Hirokawa, N., Noda, Y. and Okada, Y. (1998) 'Kinesin and dynein superfamily proteins in organelle transport and cell division.', *Current opinion in cell biology*, 10(1), pp. 60–73. Available at: http://www.ncbi.nlm.nih.gov/pubmed/9484596 (Accessed: 14 June 2017).

Hoerndli, F. J. *et al.* (2013) 'Kinesin-1 Regulates Synaptic Strength by Mediating the Delivery, Removal, and Redistribution of AMPA Receptors', *Neuron*, 80(6), pp. 1421–1437. doi: 10.1016/j.neuron.2013.10.050.

Hoffman, B. D. *et al.* (2006) 'The consensus mechanics of cultured mammalian cells', *Proceedings of the National Academy of Sciences*, 103(27), pp. 10259–10264. doi: 10.1073/pnas.0510348103.

Huang, B. *et al.* (2008) 'Three-Dimensional Super-Resolution Imaging by Stochastic Optical Reconstruction Microscopy', *Science*, 319(5864). Available at: http://science.sciencemag.org/content/319/5864/810 (Accessed: 8 August 2017).

Huang, F. *et al.* (2011) 'Simultaneous multiple-emitter fitting for single molecule super-resolution imaging.', *Biomedical optics express*. Optical Society of America, 2(5), pp. 1377–93. doi: 10.1364/BOE.2.001377.

Huynh, K. K. *et al.* (2007) 'LAMP proteins are required for fusion of lysosomes with phagosomes', *The EMBO Journal*, 26(2), pp. 313–324. doi: 10.1038/sj.emboj.7601511.

Imamura, T. *et al.* (2003) 'Insulin-induced GLUT4 translocation involves protein kinase C-lambda-mediated functional coupling between Rab4 and the motor protein kinesin.', *Molecular and cellular biology*, 23(14), pp. 4892–900. Available at: http://www.ncbi.nlm.nih.gov/pubmed/12832475 (Accessed: 8 September 2017).

Jahn, K. A. *et al.* (2012) 'Correlative microscopy: Providing new understanding in the biomedical and plant sciences', *Micron*, 43(5), pp. 565–582. doi: 10.1016/j.micron.2011.12.004.

Janel, S. *et al.* (2017) 'CLAFEM', in *Methods in cell biology*, pp. 165–185. doi: 10.1016/bs.mcb.2017.03.010.

Jans, D. C. *et al.* (2013) 'STED super-resolution microscopy reveals an array of MINOS clusters along human mitochondria', *Proceedings of the National Academy of Sciences*, 110(22), pp. 8936–8941. doi: 10.1073/pnas.1301820110.

Jeon, N. L. *et al.* (2000) 'Generation of Solution and Surface Gradients Using Microfluidic Systems', *Langmuir*, 16(22), pp. 8311–8316. doi: 10.1021/la000600b.

Jha, R. and Surrey, T. (2015) 'Regulation of processive motion and microtubule localization of cytoplasmic dynein', *Biochemical Society Transactions*, 43(1), pp. 48–57. doi: 10.1042/BST20140252.

Johansson, M. *et al.* (2007) 'Activation of endosomal dynein motors by stepwise assembly of Rab7?RILP?p150 ^Glued , ORP1L, and the receptor ?lll spectrin', *The Journal of Cell Biology*, 176(4), pp. 459–471. doi: 10.1083/jcb.200606077.

Jonas, M. *et al.* (2008) 'Fast Fluorescence Laser Tracking Microrheometry, II: Quantitative Studies of Cytoskeletal Mechanotransduction', *Biophysical Journal*, 95(2), pp. 895–909. doi: 10.1529/biophysj.107.120303.

Jones, S. A. *et al.* (2011) 'Fast, three-dimensional super-resolution imaging of live cells', *Nature Methods*, 8(6), pp. 499–505. doi: 10.1038/nmeth.1605.

Jungmann, R. *et al.* (2014) 'Multiplexed 3D cellular super-resolution imaging with DNA-PAINT and Exchange-PAINT', *Nature Methods*, 11(3), pp. 313–318. doi: 10.1038/nmeth.2835.

Kanai, Y., Dohmae, N. and Hirokawa, N. (2004) 'Kinesin Transports RNA', *Neuron*, 43(4), pp. 513–525. doi: 10.1016/j.neuron.2004.07.022.

King, S. J. and Schroer, T. A. (2000) 'Dynactin increases the processivity of the cytoplasmic dynein motor.', *Nature cell biology*, 2(1), pp. 20–4. doi: 10.1038/71338.

Klar, T. A. and Hell, S. W. (1999) 'Subdiffraction resolution in far-field fluorescence microscopy', *Optics Letters*. Optical Society of America, 24(14), p. 954. doi: 10.1364/OL.24.000954.

Kollmannsperger, A. *et al.* (2016) 'Live-cell protein labelling with nanometre precision by cell squeezing', *Nature Communications*, 7, p. 10372. doi: 10.1038/ncomms10372.

Kon, T., Sutoh, K. and Kurisu, G. (2011) 'X-ray structure of a functional full-length dynein motor domain', *Nature Structural & Molecular Biology*, 18(6), pp. 638–642. doi: 10.1038/nsmb.2074.

Kural, C. (2005) 'Kinesin and Dynein Move a Peroxisome in Vivo: A Tug-of-War or Coordinated Movement?', *Science*, 308(5727), pp. 1469–1472. doi: 10.1126/science.1108408.

Lakadamyali, M. *et al.* (2012) '3D Multicolor Super-Resolution Imaging Offers Improved Accuracy in Neuron Tracing', *PLoS ONE*. Edited by Y. He, 7(1), p. e30826. doi: 10.1371/journal.pone.0030826.

Lakadamyali, M. (2014) 'Super-Resolution Microscopy: Going Live and Going Fast', *ChemPhysChem*, 15(4), pp. 630–636. doi: 10.1002/cphc.201300720.

Lawrence, C. J. *et al.* (2004) 'A standardized kinesin nomenclature: Table I.', *The Journal of Cell Biology*, 167(1), pp. 19–22. doi: 10.1083/jcb.200408113.

Leidel, C. *et al.* (2012) 'Measuring Molecular Motor Forces In Vivo: Implications for Tug-of-War Models of Bidirectional Transport', *Biophysical Journal*. The Biophysical Society, 103(3), p. 492. doi: 10.1016/j.bpj.2012.06.038.

Leterrier, C. *et al.* (2017) 'The nano-architecture of the axonal cytoskeleton', *Nature Reviews Neuroscience*, 18(12), pp. 713–726. doi: 10.1038/nrn.2017.129.

Levi, V. *et al.* (2006) 'Organelle Transport along Microtubules in Xenopus Melanophores: Evidence for Cooperation between Multiple Motors', *Biophysical Journal*, 90(1), pp. 318–327. doi: 10.1529/biophysj.105.067843.

van de Linde, S., Heilemann, M. and Sauer, M. (2012) 'Live-Cell Super-Resolution Imaging with Synthetic Fluorophores', *Annual Review of Physical Chemistry*, 63(1), pp. 519–540. doi: 10.1146/annurev-physchem-032811-112012.

Lingwood, D., Simons, K. and et al (2009) 'Lipid Rafts As a Membrane-Organizing Principle', *Science*, 327(5961). Available at: http://science.sciencemag.org/content/327/5961/46.full (Accessed: 6 September 2017).

Lippincott-Schwartz, J. *et al.* (1995) 'Kinesin is the motor for microtubule-mediated Golgi-to-ER membrane traffic.', *The Journal of cell biology*, 128(3), pp. 293–306. Available at: http://www.ncbi.nlm.nih.gov/pubmed/7844144 (Accessed: 10 July 2017).

Lock, J. G. and Strömblad, S. (2010) 'Systems microscopy: An emerging strategy for the life sciences', *Experimental Cell Research*, 316(8), pp. 1438–1444. doi: 10.1016/j.yexcr.2010.04.001.

Lovas, J. R. and Wang, X. (2013) 'The meaning of mitochondrial movement to a neuron's life', *Biochimica et Biophysica Acta (BBA) - Molecular Cell Research*, 1833(1), pp. 184–194. doi: 10.1016/j.bbamcr.2012.04.007.

Lovestone, S. *et al.* (1994) 'Alzheimer's disease-like phosphorylation of the microtubule-associated protein tau by glycogen synthase kinase-3 in transfected mammalian cells.', *Current biology : CB*, 4(12), pp. 1077–86. Available at: http://www.ncbi.nlm.nih.gov/pubmed/7704571 (Accessed: 22 September 2017).

Mallik, R. *et al.* (2004) 'Cytoplasmic dynein functions as a gear in response to load', *Nature*, 427(6975), pp. 649–652. doi: 10.1038/nature02293.

Mallik, R. *et al.* (2005) 'Building complexity: an in vitro study of cytoplasmic dynein with in vivo implications.', *Current biology : CB*, 15(23), pp. 2075–85. doi: 10.1016/j.cub.2005.10.039.

Mao, H., Yang, T. and Cremer, P. S. (2002) 'A microfluidic device with a linear temperature gradient for parallel and combinatorial measurements.', *Journal of the American Chemical Society*, 124(16), pp. 4432–5. Available at: http://www.ncbi.nlm.nih.gov/pubmed/11960472 (Accessed: 7 September 2017).

Marples, D. *et al.* (1998) 'Dynein and dynactin colocalize with AQP2 water channels in intracellular vesicles from kidney collecting duct.', *The American journal of physiology*, 274(2 Pt 2), pp. F384-94. Available at: http://www.ncbi.nlm.nih.gov/pubmed/9486234 (Accessed: 13 July 2017).

McKenney, R. J. *et al.* (2010) 'LIS1 and NudE induce a persistent dynein force-producing state.', *Cell*, 141(2), pp. 304–14. doi: 10.1016/j.cell.2010.02.035.

McKenney, R. J. *et al.* (2014) 'Activation of cytoplasmic dynein motility by dynactin-cargo adapter complexes.', *Science (New York, N.Y.)*, 345(6194), pp. 337–41. doi: 10.1126/science.1254198.

McKenney, R. J. *et al.* (2016) 'Tyrosination of α-tubulin controls the initiation of processive dynein-dynactin motility.', *The EMBO journal*, 35(11), pp. 1175–85. doi: 10.15252/embj.201593071.

McKinney, S. A. *et al.* (2009) 'A bright and photostable photoconvertible fluorescent protein', *Nature Methods*, 6(2), pp. 131–133. doi: 10.1038/nmeth.1296.

Miki, H. *et al.* (2001) 'All kinesin superfamily protein, KIF, genes in mouse and human', *Proceedings of the National Academy of Sciences*, 98(13), pp. 7004–7011. doi: 10.1073/pnas.111145398.

Min, J. *et al.* (2014) '3D high-density localization microscopy using hybrid astigmatic/ biplane imaging and sparse image reconstruction.', *Biomedical optics express*. Optical Society of America, 5(11), pp. 3935–48. doi: 10.1364/BOE.5.003935.

Mitra, K. and Lippincott-Schwartz, J. (2010) 'Analysis of Mitochondrial Dynamics and Functions Using Imaging Approaches', in *Current Protocols in Cell Biology*. Hoboken, NJ, USA: John Wiley & Sons, Inc., p. Unit 4.25.1-21. doi: 10.1002/0471143030.cb0425s46.

Moerner, W. E. *et al.* (1997) 'On/off blinking and switching behaviour of single molecules of green fluorescent protein.', *Nature*, 388(6640), pp. 355–358. doi: 10.1038/41048.

Morfini, G. *et al.* (2002) 'Glycogen synthase kinase 3 phosphorylates kinesin light chains and negatively regulates kinesin-based motility', *The EMBO Journal*, 21(3), pp. 281–293. doi: 10.1093/emboj/21.3.281.

Morfini, G. *et al.* (2004) 'A novel CDK5-dependent pathway for regulating GSK3 activity and kinesin-driven motility in neurons', *The EMBO Journal*, 23(11), pp. 2235–2245. doi: 10.1038/sj.emboj.7600237.

Morfini, G. A. *et al.* (2009) 'Pathogenic huntingtin inhibits fast axonal transport by activating JNK3 and phosphorylating kinesin', *Nature Neuroscience*, 12(7), pp. 864–871. doi: 10.1038/nn.2346.

Moughamian, A. J. *et al.* (2013) 'Ordered recruitment of dynactin to the microtubule plus-end is required for efficient initiation of retrograde axonal transport.', *The Journal of neuroscience : the official journal of the Society for Neuroscience*, 33(32), pp. 13190–203. doi: 10.1523/JNEUROSCI.0935-13.2013.

Muller, M. J. I., Klumpp, S. and Lipowsky, R. (2008) 'Tug-of-war as a cooperative mechanism for bidirectional cargo transport by molecular motors', *Proceedings of the National Academy of Sciences*, 105(12), pp. 4609–4614. doi: 10.1073/pnas.0706825105.

Murray, J. W., Bananis, E. and Wolkoff, A. W. (2000) 'Reconstitution of ATP-dependent movement of endocytic vesicles along microtubules in vitro: an oscillatory bidirectional process.', *Molecular biology of the cell*, 11(2), pp. 419–33. Available at: http://www.ncbi.nlm.nih.gov/pubmed/10679004 (Accessed: 17 July 2017).

Nakata, T. and Hirokawa, N. (2003) 'Microtubules provide directional cues for polarized axonal transport through interaction with kinesin motor head', *The Journal of Cell Biology*, 162(6), pp. 1045–1055. doi: 10.1083/jcb.200302175.

Nan, X. *et al.* (2005) 'Observation of Individual Microtubule Motor Steps in Living Cells with Endocytosed Quantum Dots', *The Journal of Physical Chemistry B*, 109(51), pp. 24220–24224. doi: 10.1021/jp056360w.

Nan, X., Sims, P. A. and Xie, X. S. (2008) 'Organelle Tracking in a Living Cell with Microsecond Time Resolution and Nanometer Spatial Precision', *ChemPhysChem*, 9(5), pp. 707–712. doi: 10.1002/cphc.200700839.

Neumann, B. *et al.* (2010) 'Phenotypic profiling of the human genome by time-lapse microscopy reveals cell division genes', *Nature*, 464(7289), pp. 721–727. doi: 10.1038/nature08869.

Neuwald, A. F. *et al.* (1999) 'AAA+: A class of chaperone-like ATPases associated with the assembly, operation, and disassembly of protein complexes.', *Genome research*, 9(1), pp. 27–43. Available at: http://www.ncbi.nlm.nih.gov/pubmed/9927482 (Accessed: 12 July 2017).

Nicholas, M. P. *et al.* (2015) 'Cytoplasmic dynein regulates its attachment to microtubules via nucleotide state-switched mechanosensing at multiple AAA domains', *Proceedings of the National Academy of Sciences*, 112(20). doi: 10.1073/pnas.1417422112.

Nikić, I. *et al.* (2011) 'A reversible form of axon damage in experimental autoimmune encephalomyelitis and multiple sclerosis', *Nature Medicine*, 17(4), pp. 495–499. doi: 10.1038/nm.2324.

Nirschl, J. J. *et al.* (2016) 'α-Tubulin Tyrosination and CLIP-170 Phosphorylation Regulate the Initiation of Dynein-Driven Transport in Neurons.', *Cell reports*, 14(11), pp. 2637–52. doi: 10.1016/j.celrep.2016.02.046.

Noda, Y. *et al.* (2001) 'KIFC3, a microtubule minus end-directed motor for the apical transport of annexin XIIIb-associated Triton-insoluble membranes.', *The Journal of cell biology*, 155(1), pp. 77–88. doi: 10.1083/jcb.200108042.

Oddone, A. *et al.* (2014) 'Super-resolution imaging with stochastic single-molecule localization: Concepts, technical developments, and biological applications', *Microscopy Research and Technique*, 77(7), pp. 502–509. doi: 10.1002/jemt.22346.

Ori-McKenney, K. M. *et al.* (2010) 'A cytoplasmic dynein tail mutation impairs motor processivity.', *Nature cell biology*, 12(12), pp. 1228–34. doi: 10.1038/ncb2127.

References

Pandey, J. P. and Smith, D. S. (2011) 'A Cdk5-Dependent Switch Regulates Lis1/Ndel1/Dynein-Driven Organelle Transport in Adult Axons', *Journal of Neuroscience*, 31(47), pp. 17207–17219. doi: 10.1523/JNEUROSCI.4108-11.2011.

Paschal, B. M. and Vallee, R. B. (1987) 'Retrograde transport by the microtubule-associated protein MAP 1C', *Nature*, 330(6144), pp. 181–183. doi: 10.1038/330181a0.

Patterson, G. H. and et al (2002) 'A Photoactivatable GFP for Selective Photolabeling of Proteins and Cells', *Science*, 297(5588), pp. 1873–1877. doi: 10.1126/science.1074952.

Pazour, G. J., Dickert, B. L. and Witman, G. B. (1999) 'The DHC1b (DHC2) isoform of cytoplasmic dynein is required for flagellar assembly.', *The Journal of cell biology*, 144(3), pp. 473–81. Available at: http://www.ncbi.nlm.nih.gov/pubmed/9971742 (Accessed: 10 July 2017).

Pike, L. J. (2006) 'Rafts defined: a report on the Keystone symposium on lipid rafts and cell function', *Journal of Lipid Research*, 47(7), pp. 1597–1598. doi: 10.1194/jlr.E600002-JLR200.

Plucińska, G. *et al.* (2012) 'In Vivo Imaging of Disease-Related Mitochondrial Dynamics in a Vertebrate Model System', *Journal of Neuroscience*, 32(46). Available at: http://www.jneurosci.org/content/32/46/16203 (Accessed: 6 September 2017).

Purohit, A. *et al.* (1999) 'Direct interaction of pericentrin with cytoplasmic dynein light intermediate chain contributes to mitotic spindle organization.', *The Journal of cell biology*, 147(3), pp. 481–92. Available at: http://www.ncbi.nlm.nih.gov/pubmed/10545494 (Accessed: 12 July 2017).

Qiu, W. *et al.* (2012) 'Dynein achieves processive motion using both stochastic and coordinated stepping.', *Nature structural & molecular biology*, 19(2), pp. 193–200. doi: 10.1038/nsmb.2205.

Rai, A. *et al.* (2016) 'Dynein Clusters into Lipid Microdomains on Phagosomes to Drive Rapid Transport toward Lysosomes', *Cell*, 164(4), pp. 722–734. doi: 10.1016/j.cell.2015.12.054.

Rai, A. K. *et al.* (2013) 'Molecular Adaptations Allow Dynein to Generate Large Collective Forces inside Cells', *Cell*, 152(1–2), pp. 172–182. doi: 10.1016/j.cell.2012.11.044.

Rai, A. K. *et al.* (2013) 'Molecular adaptations allow dynein to generate large collective forces inside cells.', *Cell*, 152(1–2), pp. 172–82. doi: 10.1016/j.cell.2012.11.044.

Reck-Peterson, S. L. *et al.* (2006) 'Single-molecule analysis of dynein processivity and stepping behavior.', *Cell*, 126(2), pp. 335–48. doi: 10.1016/j.cell.2006.05.046.

Reczek, D. *et al.* (2007) 'LIMP-2 Is a Receptor for Lysosomal Mannose-6-Phosphate-Independent Targeting of ?-Glucocerebrosidase', *Cell*, 131(4), pp. 770–783. doi: 10.1016/j.cell.2007.10.018.

Redwine, W. B. *et al.* (2012) 'Structural basis for microtubule binding and release by dynein.', *Science (New York, N.Y.)*, 337(6101), pp. 1532–6. doi: 10.1126/science.1224151.

References

Ricci, M. A. *et al.* (2015) 'Chromatin Fibers Are Formed by Heterogeneous Groups of Nucleosomes In Vivo', *Cell*, 160(6), pp. 1145–1158. doi: 10.1016/j.cell.2015.01.054.

Rice, S. *et al.* (1999) 'A structural change in the kinesin motor protein that drives motility.', *Nature*, 402(6763), pp. 778–784. doi: 10.1038/45483.

Roberts, A. J. *et al.* (2009) 'AAA+ Ring and linker swing mechanism in the dynein motor.', *Cell*. Elsevier, 136(3), pp. 485–95. doi: 10.1016/j.cell.2008.11.049.

Rocha, N. *et al.* (2009) 'Cholesterol sensor ORP1L contacts the ER protein VAP to control Rab7–RILP–p150 [Glued] and late endosome positioning', *The Journal of Cell Biology*, 185(7), pp. 1209–1225. doi: 10.1083/jcb.200811005.

Rogers, S. L. *et al.* (1997) 'Regulated bidirectional motility of melanophore pigment granules along microtubules in vitro.', *Proceedings of the National Academy of Sciences of the United States of America*, 94(8), pp. 3720–5. Available at: http://www.ncbi.nlm.nih.gov/pubmed/9108044 (Accessed: 17 July 2017).

Rojas, R. *et al.* (2008) 'Regulation of retromer recruitment to endosomes by sequential action of Rab5 and Rab7.', *The Journal of cell biology*. The Rockefeller University Press, 183(3), pp. 513–26. doi: 10.1083/jcb.200804048.

Rosa-Ferreira, C. and Munro, S. (2011) 'Arl8 and SKIP act together to link lysosomes to kinesin-1.', *Developmental cell*. Elsevier, 21(6), pp. 1171–8. doi: 10.1016/j.devcel.2011.10.007.

Ross, J. L. *et al.* (2006) 'Processive bidirectional motion of dynein-dynactin complexes in vitro.', *Nature cell biology*, 8(6), pp. 562–70. doi: 10.1038/ncb1421.

Ruhnow, F., Zwicker, D. and Diez, S. (2011) 'Tracking Single Particles and Elongated Filaments with Nanometer Precision', *Biophysical Journal*, 100(11), pp. 2820–2828. doi: 10.1016/j.bpj.2011.04.023.

Rust, M. J. *et al.* (2006) 'Sub-diffraction-limit imaging by stochastic optical reconstruction microscopy (STORM)', *Nature Methods*. Nature Publishing Group, 3(10), pp. 793–796. doi: 10.1038/nmeth929.

Schafer, J. C. *et al.* (2016) 'Rab11-FIP1A regulates early trafficking into the recycling endosomes.', *Experimental cell research*. NIH Public Access, 340(2), pp. 259–73. doi: 10.1016/j.yexcr.2016.01.003.

Schlager, M. A. *et al.* (2014) 'In vitro reconstitution of a highly processive recombinant human dynein complex.', *The EMBO journal*, 33(17), pp. 1855–68. doi: 10.15252/embj.201488792.

Schnitzer, M. J. (1999) 'Single kinesin molecules studied with a molecular force clamp', *Nature*. Nature Publishing Group, 400(6740), pp. 184–189. doi: 10.1038/22146.

Schroeder, H. W. *et al.* (2010) 'Motor number controls cargo switching at actin-microtubule

intersections in vitro.', *Current biology : CB*. NIH Public Access, 20(8), pp. 687–96. doi: 10.1016/j.cub.2010.03.024.

Schroeder, H. W. *et al.* (2012) 'Force-Dependent Detachment of Kinesin-2 Biases Track Switching at Cytoskeletal Filament Intersections', *Biophysical Journal*, 103(1), pp. 48–58. doi: 10.1016/j.bpj.2012.05.037.

Setou, M. *et al.* (2002) 'Glutamate-receptor-interacting protein GRIP1 directly steers kinesin to dendrites', *Nature*. Nature Publishing Group, 417(6884), pp. 83–87. doi: 10.1038/nature743.

Shim, S.-H. *et al.* (2012) 'Super-resolution fluorescence imaging of organelles in live cells with photoswitchable membrane probes', *Proceedings of the National Academy of Sciences*. Springer Berlin Heidelberg, 109(35), pp. 13978–13983. doi: 10.1073/pnas.1201882109.

Shroff, H. *et al.* (2008) 'Live-cell photoactivated localization microscopy of nanoscale adhesion dynamics', *Nature Methods*. Nature Publishing Group, 5(5), pp. 417–423. doi: 10.1038/nmeth.1202.

Shubeita, G. T. *et al.* (2008) 'Consequences of Motor Copy Number on the Intracellular Transport of Kinesin-1-Driven Lipid Droplets', *Cell*. Cold Spring Harbor Laboratory Press, Cold Spring Harbor, NY, 135(6), pp. 1098–1107. doi: 10.1016/j.cell.2008.10.021.

Simons, K., Ikonen, E. and et al (1997) 'Functional rafts in cell membranes.', *Nature*, 387(6633), pp. 569–572. doi: 10.1038/42408.

Sims, P. A. and Xie, X. S. (2009) 'Probing Dynein and Kinesin Stepping with Mechanical Manipulation in a Living Cell', *ChemPhysChem*, 10(9–10), pp. 1511–1516. doi: 10.1002/cphc.200900113.

Small, A. and Stahlheber, S. (2014) 'Fluorophore localization algorithms for super-resolution microscopy', *Nature Methods*. Nature Publishing Group, 11(3), pp. 267–279. doi: 10.1038/nmeth.2844.

Soppina, V. *et al.* (2009) 'Tug-of-war between dissimilar teams of microtubule motors regulates transport and fission of endosomes.', *Proceedings of the National Academy of Sciences of the United States of America*. National Academy of Sciences, 106(46), pp. 19381–6. doi: 10.1073/pnas.0906524106.

Staff, N. P., Benarroch, E. E. and Klein, C. J. (2011) 'Neuronal intracellular transport and neurodegenerative disease', *Neurology*, 76(11), pp. 1015–1020. doi: 10.1212/WNL.0b013e31821103f7.

Stagi, M. *et al.* (2006) 'Unloading kinesin transported cargoes from the tubulin track via the inflammatory c-Jun N-terminal kinase pathway', *The FASEB Journal*, 20(14), pp. 2573–2575. doi: 10.1096/fj.06-6679fje.

Starr, D. A. (2009) 'A nuclear-envelope bridge positions nuclei and moves chromosomes', *Journal of Cell Science*, 122(5), pp. 577–586. doi: 10.1242/jcs.037622.

Subach, F. V *et al.* (2009) 'Photoactivatable mCherry for high-resolution two-color fluorescence microscopy', *Nature Methods*, 6(2), pp. 153–159. doi: 10.1038/nmeth.1298.

Svoboda, K. *et al.* (1993) 'Direct observation of kinesin stepping by optical trapping interferometry', *Nature*, 365(6448), pp. 721–727. doi: 10.1038/365721a0.

Svoboda 't, K. and Block, S. M. (1994) 'Force and Velocity Measured for Single Kinesin Molecules', *Cell*, 77, pp. 773–794. Available at: http://www.andrew.cmu.edu/course/42-620/handouts/svoboda_cell_94.pdf (Accessed: 15 June 2017).

Szczurek, A. *et al.* (2016) 'Single Molecule Localization Microscopy of Mammalian Cell Nuclei on the Nanoscale.', *Frontiers in genetics*. Frontiers Media SA, 7, p. 114. doi: 10.3389/fgene.2016.00114.

Tai, A. W., Chuang, J. Z. and Sung, C. H. (2001) 'Cytoplasmic dynein regulation by subunit heterogeneity and its role in apical transport.', *The Journal of cell biology*, 153(7), pp. 1499–509. Available at: http://www.ncbi.nlm.nih.gov/pubmed/11425878 (Accessed: 12 July 2017).

Tam, J. *et al.* (2014) 'Cross-Talk-Free Multi-Color STORM Imaging Using a Single Fluorophore', *PLoS ONE*. Edited by K. Gaus, 9(7), p. e101772. doi: 10.1371/journal.pone.0101772.

Tan, S. C., Scherer, J. and Vallee, R. B. (2011) 'Recruitment of dynein to late endosomes and lysosomes through light intermediate chains.', *Molecular biology of the cell*. American Society for Cell Biology, 22(4), pp. 467–77. doi: 10.1091/mbc.E10-02-0129.

Tanaka, Y. *et al.* (1998) 'Targeted disruption of mouse conventional kinesin heavy chain, kif5B, results in abnormal perinuclear clustering of mitochondria.', *Cell*, 93(7), pp. 1147–58. Available at: http://www.ncbi.nlm.nih.gov/pubmed/9657148 (Accessed: 9 November 2017).

Thompson, R. E. *et al.* (2002) 'Precise Nanometer Localization Analysis for Individual Fluorescent Probes', *Biophysical Journal*, 82(5), pp. 2775–2783. doi: 10.1016/S0006-3495(02)75618-X.

Thompson, R. E., Larson, D. R. and Webb, W. W. (2002) 'Precise nanometer localization analysis for individual fluorescent probes.', *Biophysical journal*. The Biophysical Society, 82(5), pp. 2775–83. doi: 10.1016/S0006-3495(02)75618-X.

Toepke, M. W. and Beebe, D. J. (2006) 'PDMS absorption of small molecules and consequences in microfluidic applications.', *Lab on a chip*, 6(12), pp. 1484–6. doi: 10.1039/b612140c.

Trinczek, B. *et al.* (1999) 'Tau regulates the attachment/detachment but not the speed of motors in microtubule-dependent transport of single vesicles and organelles.', *Journal of cell science*, 112 (Pt 14), pp. 2355–67. Available at: http://www.ncbi.nlm.nih.gov/pubmed/10381391 (Accessed: 13 June 2017).

Unger, M. A. *et al.* (2000) 'Monolithic microfabricated valves and pumps by multilayer soft

lithography.', *Science (New York, N.Y.)*, 288(5463), pp. 113–6. Available at: http://www.ncbi.nlm.nih.gov/pubmed/10753110 (Accessed: 6 September 2017).

Urnavicius, L. *et al.* (2015) 'The structure of the dynactin complex and its interaction with dynein', *Science*, 347(6229), pp. 1441–1446. doi: 10.1126/science.aaa4080.

Vale, R. D. (2003) 'The molecular motor toolbox for intracellular transport.', *Cell*, 112(4), pp. 467–80. Available at: http://www.ncbi.nlm.nih.gov/pubmed/12600311 (Accessed: 14 June 2017).

Vale, R. D., Reese, T. S. and Sheetz, M. P. (1985) 'Identification of a novel force-generating protein, kinesin, involved in microtubule-based motility.', *Cell*, 42(1), pp. 39–50. Available at: http://www.ncbi.nlm.nih.gov/pubmed/3926325 (Accessed: 14 June 2017).

Vale, R. D. and Toyoshima, Y. Y. (1988) 'Rotation and translocation of microtubules in vitro induced by dyneins from Tetrahymena cilia.', *Cell*, 52(3), pp. 459–69. Available at: http://www.ncbi.nlm.nih.gov/pubmed/2964278 (Accessed: 14 June 2017).

Vallee, R. B. *et al.* (1988) 'Microtubule-associated protein 1C from brain is a two-headed cytosolic dynein', *Nature*, 332(6164), pp. 561–563. doi: 10.1038/332561a0.

Vallee, R. B. *et al.* (2000) 'A role for the lissencephaly gene LIS1 in mitosis and cytoplasmic dynein function.', *Nature Cell Biology*, 2(11), pp. 784–791. doi: 10.1038/35041020.

Vallee, R. B. *et al.* (2004) 'Dynein: An ancient motor protein involved in multiple modes of transport.', *Journal of neurobiology*, 58(2), pp. 189–200. doi: 10.1002/neu.10314.

Vaughan, J. C. *et al.* (2013) 'Phosphine quenching of cyanine dyes as a versatile tool for fluorescence microscopy.', *Journal of the American Chemical Society*. NIH Public Access, 135(4), pp. 1197–200. doi: 10.1021/ja3105279.

Vaughan, K. T. and Vallee, R. B. (1995) 'Cytoplasmic dynein binds dynactin through a direct interaction between the intermediate chains and p150Glued.', *The Journal of cell biology*, 131(6 Pt 1), pp. 1507–16. Available at: http://www.ncbi.nlm.nih.gov/pubmed/8522607 (Accessed: 12 July 2017).

Vaughan, P. S. *et al.* (2002) 'A role for regulated binding of p150 ^{Glued} to microtubule plus ends in organelle transport', *The Journal of Cell Biology*, 158(2), pp. 305–319. doi: 10.1083/jcb.200201029.

Verdeny-Vilanova, I. *et al.* (2017a) '3D motion of vesicles along microtubules helps them to circumvent obstacles in cells'. Available at: http://jcs.biologists.org/content/joces/early/2017/04/13/jcs.201178.full.pdf (Accessed: 15 June 2017).

Verdeny-Vilanova, I. *et al.* (2017b) '3D motion of vesicles along microtubules helps them to circumvent obstacles in cells.', *Journal of cell science*, 130(11), pp. 1904–1916. doi: 10.1242/jcs.201178.

Vershinin, M. *et al.* (2007) 'Multiple-motor based transport and its regulation by Tau', *Proceedings of the National Academy of Sciences*, 104(1), pp. 87–92. doi: 10.1073/pnas.0607919104.

Vershinin, M. *et al.* (2008) 'Tuning Microtubule-Based Transport Through Filamentous MAPs: The Problem of Dynein', *Traffic*. Blackwell Publishing Ltd, 9(6), pp. 882–892. doi: 10.1111/j.1600-0854.2008.00741.x.

Visscher, K., Schnitzer, M. J. and Block, S. M. (2000) 'Force production by single kinesin motors', *Nature Cell Biology*. Nature Publishing Group, 2(10), pp. 718–723. doi: 10.1038/35036345.

Wang, T. *et al.* (2011) 'Rab7: Role of its protein interaction cascades in endo-lysosomal traffic', *Cellular Signalling*, 23(3), pp. 516–521. doi: 10.1016/j.cellsig.2010.09.012.

Wang, X. and Schwarz, T. L. (2009) 'The Mechanism of Ca2+-Dependent Regulation of Kinesin-Mediated Mitochondrial Motility', *Cell*, 136(1), pp. 163–174. doi: 10.1016/j.cell.2008.11.046.

Wang, Y. *et al.* (2014) 'Localization events-based sample drift correction for localization microscopy with redundant cross-correlation algorithm.', *Optics express*, 22(13), pp. 15982–91. Available at: http://www.ncbi.nlm.nih.gov/pubmed/24977854 (Accessed: 21 February 2018).

Wedaman, K. P. *et al.* (1996) 'Sequence and submolecular localization of the 115-kD accessory subunit of the heterotrimeric kinesin-II (KRP85/95) complex.', *The Journal of cell biology*. The Rockefeller University Press, 132(3), pp. 371–80. Available at: http://www.ncbi.nlm.nih.gov/pubmed/8636215 (Accessed: 9 November 2017).

Weibel, D. and Whitesides, G. (2006) 'Applications of microfluidics in chemical biology', *Current Opinion in Chemical Biology*, 10(6), pp. 584–591. doi: 10.1016/j.cbpa.2006.10.016.

Welte, M. A. (2004) 'Bidirectional Transport along Microtubules', *Current Biology*, 14(13), pp. R525–R537. doi: 10.1016/j.cub.2004.06.045.

Whitesides, G. M. (2006) 'The origins and the future of microfluidics.', *Nature*, 442(7101), pp. 368–73. doi: 10.1038/nature05058.

Wiedenmann, J. *et al.* (2004) 'EosFP, a fluorescent marker protein with UV-inducible green-to-red fluorescence conversion', *Proceedings of the National Academy of Sciences*, 101(45), pp. 15905–15910. doi: 10.1073/pnas.0403668101.

Wordeman, L. (2010) 'How kinesin motor proteins drive mitotic spindle function: Lessons from molecular assays.', *Seminars in cell & developmental biology*. NIH Public Access, 21(3), pp. 260–8. doi: 10.1016/j.semcdb.2010.01.018.

Wurm, C. A. *et al.* (2011) 'Nanoscale distribution of mitochondrial import receptor Tom20 is adjusted to cellular conditions and exhibits an inner-cellular gradient.', *Proceedings of the National Academy of Sciences of the United States of America*. National Academy of

Sciences, 108(33), pp. 13546–51. doi: 10.1073/pnas.1107553108.

Yan, R. *et al.* (2018) 'Spectrally Resolved and Functional Super-resolution Microscopy via Ultrahigh-Throughput Single-Molecule Spectroscopy', *Accounts of Chemical Research*, p. acs.accounts.7b00545. doi: 10.1021/acs.accounts.7b00545.

Yano, H. *et al.* (2001) 'Association of Trk neurotrophin receptors with components of the cytoplasmic dynein motor.', *The Journal of neuroscience : the official journal of the Society for Neuroscience*, 21(3), p. RC125. Available at: http://www.ncbi.nlm.nih.gov/pubmed/11157096 (Accessed: 12 July 2017).

Yildiz, A. *et al.* (2004) 'Kinesin Walks Hand-Over-Hand', *Science*, 303(5658), pp. 676–678. doi: 10.1126/science.1093753.

Yildiz, A. *et al.* (2004) 'Kinesin walks hand-over-hand.', *Science (New York, N.Y.)*, 303(5658), pp. 676–8. doi: 10.1126/science.1093753.

Yildiz, A. *et al.* (2008) 'Intramolecular strain coordinates kinesin stepping behavior along microtubules.', *Cell*, 134(6), pp. 1030–41. doi: 10.1016/j.cell.2008.07.018.

Yogalingam, G. *et al.* (2008) 'Neuraminidase 1 is a negative regulator of lysosomal exocytosis.', *Developmental cell*, 15(1), pp. 74–86. doi: 10.1016/j.devcel.2008.05.005.

Young, E. W. K. and Beebe, D. J. (2010) 'Fundamentals of microfluidic cell culture in controlled microenvironments', *Chemical Society Reviews*, 39(3), p. 1036. doi: 10.1039/b909900j.

Zanacchi, F. C. *et al.* (2017) 'A DNA origami platform for quantifying protein copy number in super-resolution', *Nature Methods*. Nature Publishing Group, 14(8), pp. 789–792. doi: 10.1038/nmeth.4342.

Zessin, P. J. M., Finan, K. and Heilemann, M. (2012) 'Super-resolution fluorescence imaging of chromosomal DNA', *Journal of Structural Biology*, 177(2), pp. 344–348. doi: 10.1016/j.jsb.2011.12.015.

Zhang, M. *et al.* (2012) 'Rational design of true monomeric and bright photoactivatable fluorescent proteins', *Nature Methods*, 9(7), pp. 727–729. doi: 10.1038/nmeth.2021.

Zhang, Z. *et al.* (2015) 'Ultrahigh-throughput single-molecule spectroscopy and spectrally resolved super-resolution microscopy', *Nature Methods*. Nature Publishing Group, 12(10), pp. 935–938. doi: 10.1038/nmeth.3528.